1 2 9 0

UNIVERSIDADE D
COIMBRA

Francisca Isabel Teixeira Salgueiro

NUMERICAL AND EXPERIMENTAL ANALYSIS OF THE L-PBF ADDITIVE MANUFACTURING PROCESS OF ALUMINIUM ALLOYS

Dissertação no âmbito do Mestrado Integrado em Engenharia Mecânica, na especialidade de Produção e Projeto orientada pelo Doutor Rodolfo Lisboa Batalha e pelo Professor Doutor Diogo Mariano Simões Neto e apresentada ao Departamento de Engenharia Mecânica da Faculdade de Ciências e Tecnologia da Universidade de Coimbra

Julho de 2022

1290

FACULDADE DE
CIÊNCIAS E TECNOLOGIA
UNIVERSIDADE DE
COIMBRA

Numerical and experimental analysis of the L-PBF additive manufacturing process of aluminium alloys

Dissertation submitted in partial fulfilment of the requirements for the degree of Master in Mechanical Engineering in the speciality of Manufacturing and Design

Análise numérica e experimental do processo de fabrico aditivo L-PBF em ligas de alumínio

Autor
Francisca Isabel Teixeira Salgueiro

Advisors
Dr. Rodolfo Lisboa Batalha
Prof. Diogo Mariano Simões Neto

Committee

Chair	**Professor Doutor João Paulo da Silva Gil Nobre** **Professor Auxiliar da Universidade de Coimbra**
Member	**Professora Doutora Marta Cristina Cardoso Oliveira** **Professora Associada da Universidade de Coimbra**
Advisor	**Doutor Rodolfo Lisboa Batalha** **Investigador do Instituto da Soldadura e da Qualidade**

Institutional collaboration

Instituto da Soldadura e da Qualidade

Coimbra, July 2022

“Nobody escapes the dream of flying, of going beyond the limits of the space where he was born, of seeing new places and new people. But knowing how to see in each thing, in each person, that something that defines them as special, a singular object, a friend, is fundamental.”

Antoine de Saint-Exupéry.

Acknowledgements

The realization of this master's thesis had important support and incentives from people without whom it would not have become a reality nor would it have been possible to achieve it. I have always been taught to thank you so it is time to do.

To Professor Diogo Neto and Doctor Rodolfo Batalha for their guidance, support, and availability, for the knowledge they both conveyed to me and for each critical opinion that allowed me to evolve and solve the doubts and problems that I came across during the completion of this work. Thanks again for all the encouraging words. I feel like we were an amazing team.

Thanks to the Mechanical Engineering Department for providing all the resources necessary to carry out the simulations and some measurements included in this dissertation and to the Welding and Quality Institute, for accepting me and for providing me with a phenomenal experience that I will never forget.

To my parents, who always gave me wings to fly and gave me the opportunity to always choose whatever it was and the only mission they assigned me was: to be happy every day. Thank you for being so present in my life and supporting me in any dream. Are the best.

To my sister who is a force of nature, a giant thanks you for being light every day not only in my life, but in the lives of everyone around her, for being a second mother and supporting me every day without exception.

To my friends who have been with me since the beginning of college and who have shared the most random things with me. With them I lived incredible and transformative moments. You are part of my heart forever and you know that you have become like sisters to me. I am proof that when there is love there is no distance.

To those who were like a second home during this journey, a thank you to all of them, for their support, for the conversations, for the animation, for the help throughout this process, for becoming much more than co-workers. Not every day was good, but they were all worth it. It was wonderful.

This research work was sponsored by national funds from the Portuguese Foundation for Science and Technology (FCT) under the project with reference PTDC/EME-EME/31657/2017 and by European Regional Development Fund (ERDF) through the Portugal 2020 program (PT2020) and the Centro 2020 Regional Operational Programme (CENTRO-01-0145-FEDER-031657).

Abstract

The fast growth of the additive manufacturing processes over the past years has been motivated by their ability to produce parts directly from a computer-aided design file in a layer-by-layer fashion. The metal powder-based additive manufacturing processes have attracted the attention of aerospace, energy and automotive industries, in order to produce on-demand engineering parts with complex geometrical features. Nevertheless, the occurrence of manufacturing defects remains an important unsolved issue. The proper selection of the process parameters is vital to producing components without defects.

The main objective of the present study is the numerical and experimental analysis of the Laser-Powder Bed Fusion (L-PBF) for two different aluminium alloys for the powder material (AlSi10Mg and Al-6.3Cu). A design of experiments was carried out considering different combinations of laser power and scanning speed for three different geometries: (i) single track scanning; (ii) hollow thin-wall cube; (iii) cantilever. The effect of the multi-layer deposition was evaluated using hollow thin-wall cubes, while the cantilevers were used for evaluating the residual stresses generated both during the manufacturing process and after the heat treatment. The finite element modelling of the L-PBF manufacturing process was carried at two different scales: (i) meso-scale analysis and (ii) macro-scale analysis.

Regarding the single tracks built on the substrate, the track width increases either by increasing the laser power or decreasing the scanning speed. Despite the variability in the experimental data, the numerical predictions of the melt pool size are in agreement with the experimental measurements. The measured melt pool height is significatively larger for AlSi10Mg in comparison with the one obtained for Al-6.3Cu powder mixture. On the other and, for large values of laser power the melt pool depth is significatively larger for Al-6.3Cu powder mixture in comparison with the one obtained for AlSi10Mg. Using the same process parameters to build the hollow thin-wall cubes, the obtained wall thickness is significatively larger than the melt pool width obtained in the single track. This is a consequence of the low thermal conductivity of the powder bed surrounding the part under building. The residual stresses were indirectly measured using the cantilever deflection after the partial cutting operation. The cantilever profile after the cut is only slightly influenced by the process parameters studied (laser power, scanning speed, hatch distance, layer thickness and laser emission mode). Applying the heat treatment to the cantilever geometry, the deflection resulting from the cutting operation is very small.

Keywords: Additive manufacturing, Laser-powder bed fusion, Design of experiments, Numerical modelling, AlSi10Mg, Al-6.3Cu.

Resumo

O rápido crescimento dos processos de fabrico aditivo nos últimos anos foi motivado por sua capacidade de produzir peças diretamente de um projeto assistido por computador, camada por camada. Os processos de fabrico aditivo à base de pó metálico têm atraído a atenção das indústrias aeroespacial, energia e automotiva, com o objetivo de produzir peças de engenharia com características geométricas complexas. No entanto, a ocorrência de defeitos de fabrico continua a ser um problema não resolvido. A seleção adequada dos parâmetros do processo é vital para a produção de componentes sem defeitos.

O objetivo principal deste estudo é a análise numérica e experimental do processo de fabrico aditivo Laser-Powder Bed Fusion (L-PBF) para duas ligas de alumínio (AlSi10Mg e Al-6.3Cu). Foi realizado um desenho de experiências considerando diferentes combinações de potência do laser e velocidade de varrimento para três geometrias diferentes: (i) trilha; (ii) parede fina; (iii) cantilever. Os cantilevers foram usados para avaliar as tensões residuais geradas durante o processo de fabrico e após o tratamento térmico. A simulação de elementos finitos do processo L-PBF foi realizada em duas escalas diferentes: (i) meso-escala e (ii) macro-escala.

Em relação às trilhas construídas no substrato, a largura da trilha aumenta com o aumento da potência do laser ou com a diminuição da velocidade de varrimento. Apesar da variabilidade nos dados experimentais, as previsões numéricas do tamanho da poça de fusão estão de acordo com as medições experimentais. A altura da poça de fusão medida é significativamente maior para AlSi10Mg em comparação com a obtida para a mistura de pó Al-6.3Cu. Por outro lado, para grandes valores de potência do laser a profundidade da poça de fusão é significativamente maior para a mistura de pó Al-6.3Cu em comparação com a obtida para AlSi10Mg. Usando os mesmos parâmetros de processo para construir as paredes finas, a espessura de parede obtida é significativamente maior do que a largura da poça de fusão obtida na trilha única. Esta é uma consequência da baixa condutividade térmica do leito de pó que envolve a peça em construção. As tensões residuais foram medidas indiretamente usando a deflexão do cantilever após a operação de corte parcial. O perfil do cantilever após o corte é apenas ligeiramente influenciado pelos parâmetros de processo estudados (potência do laser, velocidade de varrimento, distância entre vetores, espessura da camada e modo de emissão do laser). Aplicando o tratamento térmico à geometria do cantilever, a deflexão resultante da operação de corte é muito pequena.

Palavras-chave: Fabrico aditivo, Fusão a laser em leito de pó, Desenho de experiências, Modelação numérica, AlSi10Mg, Al-6.3Cu.

Table of contents

LIST OF FIGURES ix

LIST OF TABLES xiii

LIST OF SIMBOLS AND ACRONYMS/ABBREVIATIONS xv
- List of Symbols xv
- Acronyms/Abbreviations xvi

1. INTRODUCTION 1
   - 1.1. Additive manufacturing 1
   - 1.2. Laser-Powder Bed Fusion (L-PBF) of Al-based Materials 2
   - 1.3. Aims of the study and dissertation outline 7

2. EXPERIMENTAL PROCEDURE 9
   - 2.1. Materials 9
   - 2.2. Sample Preparation 11
     - 2.2.1. L-PBF equipment 11
     - 2.2.2. Single track deposition 12
     - 2.2.3. Hollow thin-wall cubes 14
     - 2.2.4. Cantilevers 15
   - 2.3. Heat treatment 18

3. FINITE ELEMENT MODELLING 21
   - 3.1. Meso-scale modelling 21
     - 3.1.1. Transient thermal analysis 21
     - 3.1.2. Heat source 22
     - 3.1.3. Numerical model 23
   - 3.2. Macro-scale modelling 25
     - 3.2.1. Simufact Additive 26
     - 3.2.2. Inherent strain method 28

4. RESULTS AND DISCUSSION 31
   - 4.1. Powder granulometry 31
   - 4.2. Single track scanning 32
     - 4.2.1. Single track quality 33
     - 4.2.2. Melt pool dimensions 41
   - 4.3. Hollow thin-wall cubes 48
   - 4.4. Cantilevers 52
     - 4.4.1. Residual stresses and sample deflection 53
     - 4.4.2. Heat treatment 58

5. CONCLUSIONS 61
   - 5.1. Future work 62

REFERENCES 63

ANNEX A 71

LIST OF FIGURES

Figure 1.1. General process workflow of Additive Manufacturing from CAD model to 3D object [2]. 1

Figure 1.2. Examples of components obtained from additive manufacturing processes [7]. 2

Figure 1.3. Classification of additive manufacturing technologies into seven categories according to the ASTM International [11]. 2

Figure 1.4. Schematically representation of L-PBF technology [16]. 3

Figure 1.5. Examples of manufacturing defects arising in components obtained by L-PBF [13]. 4

Figure 1.6. Description of the part to be constructed and temperature profile (after dwell time) obtained from the thermal finite element analysis [36]. 5

Figure 1.7. Physical effects and processes taking place during AM [48]. 6

Figure 2.1. Equipment used to prepare the Al-6.3Cu alloy for use in the L-PBF process: (a) drying oven used to remove the powders humidity; (b) drum hoop mixer device used for blend metal powders. 10

Figure 2.2. Equipment used in powder granulometry analysis: (a) CISA Sieve Shaker BA200N; (b) manual grinder and polisher EcoMet30; (c) Zeiss optical microscope. 11

Figure 2.3. Renishaw system for L-PBF additive manufacturing: (a) RenAM 500S Flex; (b) substrate geometry used in the reduced build volume. 12

Figure 2.4. Configuration and process parameters used in the single-track scanning: (a) AlSi10Mg; (b) Al-6.3Cu powder mixture. 13

Figure 2.5. Experimental observation of the single-tracks deposited on the substrate: (a) AlSi10Mg; (b) Al-6.3Cu powder mixture. 14

Figure 2.6. Geometry and main dimensions of the hollow thin-wall cube produced by L-PBF. 14

Figure 2.7. Hollow thin-wall cubes of AlSi10Mg: (a) configuration of the process parameters; (b) experimental observation. 15

Figure 2.8. Geometry and main dimensions of the cantilever used to evaluate the residual stresses. 16

Figure 2.9. Printed cantilevers for AlSi10Mg using different combinations of process parameters (beam power, scanning speed, hatch distance, layer thickness and laser mode). 17

Figure 2.10. Measuring the cantilever profile with Mitutoyo surface test SJ-500: (a) experimental setup; (b) detail of the probe during the measurement. 18

Figure 2.11. Oven Nabertherm NW200 used in the heat treatment of the cantilevers. 19

Figure 3.1. Schematic diagram of laser beam irradiating on the powder bed surface [58]. 22

Figure 3.2. Modelling the laser emission modes for P=200 W: (a) CW and v=400 mm/s; (b) MW with 40 µs of exposure time and 16 µm of point distance. 23

Figure 3.3. Geometry and finite element mesh used in the numerical modelling of the single-track scanning: (a) solution domain composed by the substrate and powder layer; (b) detail of the mesh around the symmetry plane. 24

Figure 3.4. Geometry and finite element mesh used in the numerical modelling of the hollow thin-wall cube: (a) entire solution domain; (b) solution domain without powder; (c) detail of the mesh in the corner. 25

Figure 3.5. Effect of temperature on the mechanical properties of AlSi10Mg: (a) Young modulus; (b) flow stress evolution [source: Simufact material database]. 26

Figure 3.6. Finite element mesh used in the simulation of the cantilever geometry: (a) global lateral view of the coarse mesh (element size: 0.5 mm); (b) detail of the coarse mesh; (c) global lateral view of the fine mesh (element size: 0.25 mm); (d) detail of the fine mesh 27

Figure 3.7. Menu of Simufact Additive containing the starting values for the inherent strains used in the calibration procedure. 29

Figure 4.1. Characterization of the AlSi10Mg powder: (a) particle size distribution; (b) cross-section of the powder particles. 31

Figure 4.2. Characterization of pure powder: (a) particle size distribution of Al powder; (b) cross-section of Al powder particles; (c) particle size distribution of Cu powder; (d) cross-section of Cu powder particles. 32

Figure 4.3. Design of experiments for single-track scanning of AlSi10Mg for laser mode: (a) CW; (b) MW. 34

Figure 4.4. Design of experiments for single-track scanning of Al-6.3Cu for laser mode: (a) CW; (b) MW. 35

Figure 4.5. Morphology of the single tracks obtained experimentally for AlSi10Mg using the laser mode: (a) CW; (b) MW. 36

Figure 4.6. Morphology of the single tracks obtained experimentally for Al-6.3Cu using the laser mode: (a) CW; (b) MW. 36

Figure 4.7. Cross section view of each single track of AlSi10Mg for CW laser mode. 37

Figure 4.8. Cross section view of each single track of AlSi10Mg for MW laser mode. 38

Figure 4.9. Cross section view of each single track of Al-6.3Cu for CW laser mode. 39

Figure 4.10. Cross section view of each single track of Al-6.3Cu for MW laser mode. 39

Figure 4.11. Predicted material phase in single tracks for AlSi10Mg comparing CW and MW laser modes for P=200 W using: (a) v=1000 mm/s; (b) v=1500 mm/s; (c) v=2000 mm/s. 40

Figure 4.12. Predicted single tracks for AlSi10Mg using the MW laser mode: (a) top view of the interface between powder layer and substrate; (b) influence of the beam power and scanning speed on the track interface morphology. 41

Figure 4.13. Shape of the track cross-section for AlSi10Mg using the CW laser mode: (a) P=150 W and v=200 mm/s; (b) P=200 W and 100 mm/s. 42

Figure 4.14. Shape of the track cross-section for Al-6.3Cu using the CW laser mode: (a) P=200 W and v=500 mm/s; (b) P=300 W and 200 mm/s. 42

Figure 4.15. Effect of laser power and scanning speed on the measured melt pool width for AlSi10Mg using the laser mode: (a) CW; (b) MW. 43

Figure 4.16. Effect of laser power and scanning speed on the measured melt pool height for AlSi10Mg using the laser mode: (a) CW; (b) MW. 44

Figure 4.17. Effect of laser power and scanning speed on the measured melt pool depth for AlSi10Mg using the laser mode: (a) CW; (b) MW. 44

Figure 4.18. Effect of laser power and scanning speed on the predicted melt pool width for AlSi10Mg using the laser mode: (a) CW; (b) MW. 45

Figure 4.19. Effect of laser power and scanning speed on the predicted melt pool depth for AlSi10Mg using the laser mode: (a) CW; (b) MW. 45

Figure 4.20. Effect of laser power and scanning speed on the predicted melt pool length for AlSi10Mg using the laser mode: (a) CW; (b) MW. 46

Figure 4.21. Effect of laser power and scanning speed on the measured melt pool width for Al-6.3Cu using the laser mode: (a) CW; (b) MW. 46

Figure 4.22. Effect of laser power and scanning speed on the measured melt pool height for Al-6.3Cu using the laser mode: (a) CW; (b) MW. 47

Figure 4.23. Effect of laser power and scanning speed on the measured melt pool depth for Al-6.3Cu using the laser mode: (a) CW; (b) MW. 47

Figure 4.24. Design of experiments for the hollow thin-wall cube using AlSi10Mg and CW laser mode for scanning speed: (a) 100 mm/s; (b) 200 mm/s; (c) 400 mm/s; (d) 500 mm/s; (e) 1000 mm/s; (f) 1500 mm/s; (g) 2000 mm/s. 48

Figure 4.25. Design of experiments for the hollow thin-wall cube using AlSi10Mg and MW laser mode for scanning speed: (a) 100 mm/s; (b) 200 mm/s; (c) 400 mm/s; (d) 500 mm/s; (e) 1000 mm/s. 49

Figure 4.26. Effect of laser power and scanning speed on the measured wall thickness of each hollow cube for AlSi10Mg using the laser mode: (a) CW; (b) MW. 50

Figure 4.27. Predicted material phase at the end of the 40th layer deposition in the hollow thin-wall cube for P=300 W and v=200 mm/s using the CW laser mode for AlSi10Mg: (a) 0.2 mm of initial wall thickness; (b) 0.4 mm of initial wall thickness. 51

Figure 4.28. Predicted temperature field immediately after the 40th layer deposition (before cooling) in the hollow thin-wall cube for P=300 W and v=200 mm/s using the CW laser mode for AlSi10Mg: (a) 0.2 mm of initial wall thickness; (b) 0.4 mm of initial wall thickness. 51

Figure 4.29. Predicted material phase in the cross-section (middle of edge) at the 40th layer deposition in the hollow thin-wall cube for P=300 W and v=200 mm/s and using the CW laser mode for AlSi10Mg. 52

Figure 4.30. Location of the cutting plane used in the cantilevers: (a) lower face of the support structure; (b) upper face of the support structure. 53

Figure 4.31. Effect of process parameters on the measured cantilever deflection profile before and after cutting: (a) cantilevers #1 and #2; (b) cantilevers #3 and #6; (c) cantilevers #7 and #8; (d) cantilevers #4 and #5 with cutting operation performed at the upper face of the thin vertical supports. 54

Figure 4.32. Predicted σ_{xx} stress component field in the cantilever: (a) before cutting stage using the coarse mesh; (b) before cutting stage using the fine mesh; (c) after upper cut using the coarse mesh; (d) after upper cut using the fine mesh; (e) after lower cut using the fine mesh.. 55

Figure 4.33. Predicted vertical displacement field in the cantilever after cutting stage: (a) upper cut using the coarse mesh; (b) upper cut using the fine mesh; (c) lower cut using the coarse mesh; (d) lower cut using the fine mesh. 56

Figure 4.34. Effect of the cutting position on the predicted cantilever distortion: (a) numerical prediction; (b) experimental measurements. 57

Figure 4.35. Lateral view of the cantilever after the heat treatment: (a) before cut; (b) after cut. 58

Figure 4.36. Predicted σ_{xx} stress component field in the cantilever: (a) before heat treatment using the coarse mesh; (b) before heat treatment using the fine mesh; (c) after heat treatment using the coarse mesh; (d) after heat treatment using the fine mesh; (e) after cut using the fine mesh; (f) after cut using the fine mesh............. 59

Figure 4.37. Effect of the heat treatment on the cantilever distortion after lower cut: (a) numerical prediction using two different meshes; (b) experimental measurements. 60

LIST OF TABLES

Table 2.1. Chemical composition of the AlSi10Mg powder supplied by Renishaw (wt.-%). 9

Table 2.2. Definition of the process parameters used in each cantilever built with AlSi10Mg powder. VED is the volumetric energy density in J/mm³. 17

Table 3.1. Thermo-physical properties of AlSi10Mg (solid material) [source: Addimen]. 24

Table 3.2. Default values of each component of the inherent strain for AlSi10Mg........ 30

Table 4.1. Inherent strain values obtained with the isotropic calibration procedure (Simufact Additive) for cantilever built with AlSi10Mg powder. 58

LIST OF SIMBOLS AND ACRONYMS/ABBREVIATIONS

List of Symbols

β- absorptivity

c_p – specific heat

e^* – inherent strain

e^p – plastic deformation

e^t- strain due to the thermal expansion

e^e- elastic strain

e^{phase}- strain due to phase changes

e^{total}- total strain

ε- emissivity

$\{f^*\}$- nodal force vector

h – hatch distance

h_c – convective heat transfer coefficient

k- thermal conductivity coefficient

$[K]$- elastic stiffness matrix

σ- constant Stefan Boltzmann

P- power of the laser beam

ρ – mass density

$\dot{q}$- power generated per volume

q_c – heat exchange by convection

q_r – heat exchange by radiation

r_0 – laser beam radius

T_0- environment temperature

T- temperature

t- time

$\{u\}$- nodal displacement vector

v – scanning speed

Acronyms/Abbreviations

AM – Additive Manufacturing
CAD – Computer-Aided Design
CW – Continuous Wave
DED – Direct Energy Deposition
EDM – Electrical Discharge Machining
FEM – Finite Element Method
IS- Inherent Strain
ISQ – Instituto da Soldadura e da Qualidade
L-PBF – Laser Powder Bed Fusion
MW – Modulated Wave
RBV – Reduced Build Volume
VED – Volumetric energy density

1. INTRODUCTION

1.1. Additive manufacturing

Additive Manufacturing (AM), popularly called 3D printing, is the term for the layer wise manufacturing. This emerging technology allows creating parts directly from a Computer-Aided Design (CAD) file in a layer-by-layer fashion, as shown in Figure 1.1. Initially, the object geometry is created in CAD, which is them exported into a file, usually in STL format. Subsequently, this 3D geometry is imported into a slicing software, where the geometry is divided in individual slices of constant thickness. Finally, each layer slice is filled using an available tool path strategy, which is used by the 3D printing machine to generate the final object layer-by-layer [1].

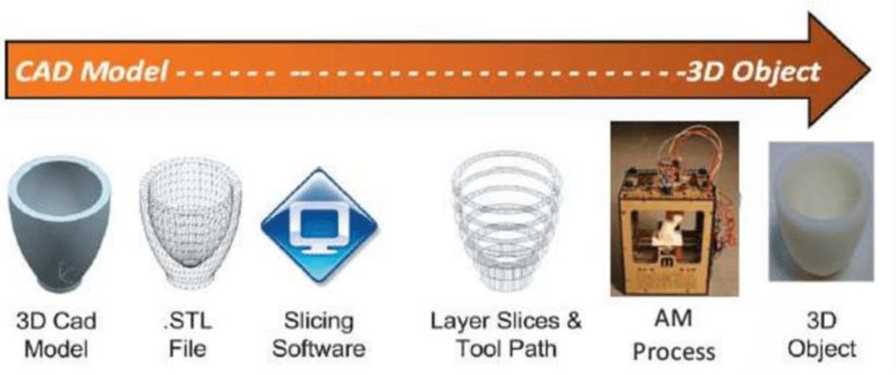

Figure 1.1. General process workflow of Additive Manufacturing from CAD model to 3D object [2].

The fast growth of the AM processes in the last years has been motivated by their ability to produce functional parts with high added value, avoiding the design constraints of traditional manufacturing processes. The unlimited design freedom of AM is ideal to produce engineering parts with complex geometrical features [3]. Besides, the short development time and the efficient use of raw materials (minimum waste), make this manufacturing process ideal for producing parts on-demand. Indeed, AM processes are now increasingly used in aerospace [4], automotive [5] and medical [6] industries because of many unique attributes. Figure 1.2 presents some examples of components with complex geometry obtained by AM processes. Since the AM can be performed using diverse materials (plastics, metals and ceramics) [7], there is an extensive variety of potential products [8]. Today, AM is already adopted in a wide application spectrum, such as jewellery, footwear, architecture, engineering, automotive and aerospace industries [9]. According to [8], the AM industry could generate an economic impact of $230 billion to $550 billion per year in 2025.

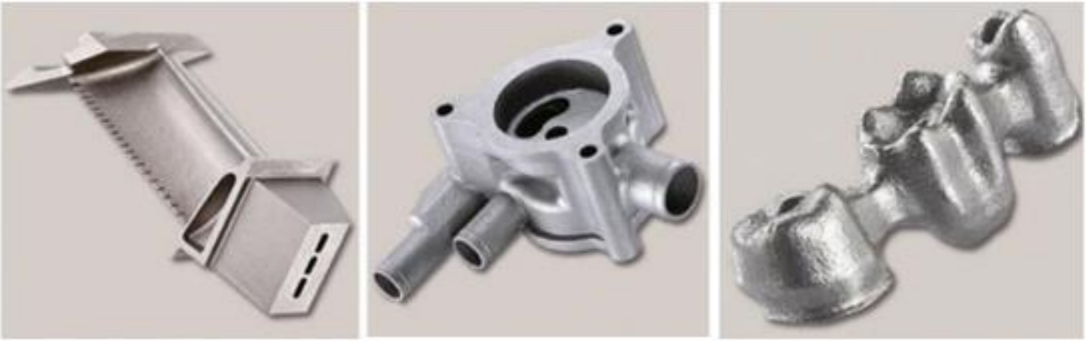

Figure 1.2. Examples of components obtained from additive manufacturing processes [7].

Recently, the AM technologies were classified into seven categories: (1) binder jetting, (2) directed energy deposition, (3) material extrusion, (4) material jetting, (5) powder bed fusion, (6) sheet lamination and (7) vat photopolymerization [10]. Figure 1.3 shows schematically each category of AM according to standard ASTM. The present work is focused on laser-powder bed fusion (L-PBF), which is based on a thermal energy selectively that melts regions of a powder bed. The L-PBF process is described in the next section.

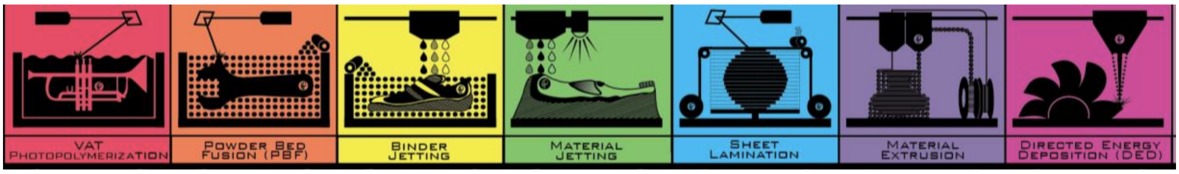

Figure 1.3. Classification of additive manufacturing technologies into seven categories according to the ASTM International [11].

1.2. Laser-Powder Bed Fusion (L-PBF) of Al-based Materials

AM has attracted much attention over the past years, particularly metal powder-based technologies [12]. Indeed, metal powder-based AM processes are now increasingly used in aerospace [4] and automotive [5] sectors. The laser-powder fed fusion (L-PBF) is one of the most popular metal powder-based technologies [13]. A laser beam is used as the heat source to melt and fuse thin layers of metallic powder, creating a melt-pool. The process is suitable to produce almost fully dense final, including the eventual pointwise control of microstructure [14] and mechanical properties [15].

Figure 1.4 presents schematically the building chamber of an L-PBF system, which is composed by a laser system, a build platform, and a powder delivery platform. The powder bed is contained in an inert atmosphere or partial vacuum to provide shielding of the molten metal. The powder layers are deposited on top of the base plate, using a recoating system to create each powder layer. The material is consolidated layer-by-layer using a laser beam. The steps required to build a part using the L-PBF technology are: (i) spread of a uniform layer of powder with the assistance of a roller or rake; (ii) melting the predefined areas of the powder layer with subsequent solidification after cooling; (iii) lowering build platform to accommodate the next powder layer; (iv) repeat steps (i) to (iii) until the build is complete; (v) removal of unnecessary powder and part extraction; (vi) post-processing when necessary.

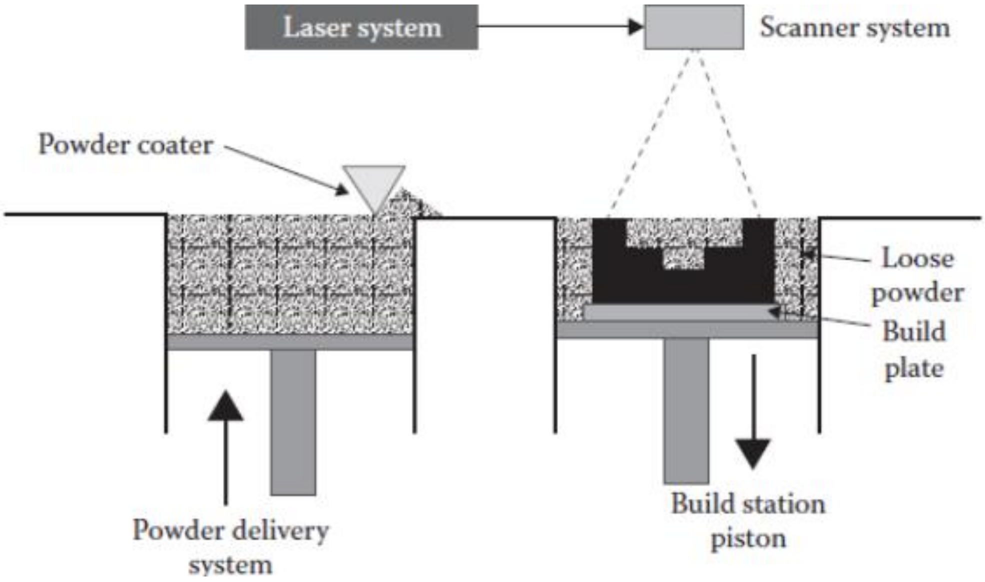

Figure 1.4. Schematically representation of L-PBF technology [16].

The raw material used in the L-PBF process is micro sized metal powder with process specific granulometry and morphology, which influence the manufacturing process result. The morphology and the powder size of the powders affects the quality of the component. For these reasons in the L-PBF process, the use of spherical powders is recommended. The powder produced via gas atomization are preferred to those that are water-atomized, which are more irregular [17].

Although the metal powder-based AM processes present some advantages over traditional manufacturing processes, several issues remain unsolved. The cyclic melting and solidification processes generate complex heat transport and physical mechanisms, which can lead to defects [18]. The most common defects include porosity, rough surfaces, warping and part distortions due to residual stresses, cracking and delamination [19]. Figure 1.5 presents some examples of manufacturing defects arising in components obtained by L-PBF. Thus, the manufacturing defects and their consequences on the quality and mechanical performance of produced parts are currently a major concern. Hence, it is essential to understand the mechanisms behind the generation of each defect, allowing to obtain defect-free parts by selecting appropriate process parameters [20].

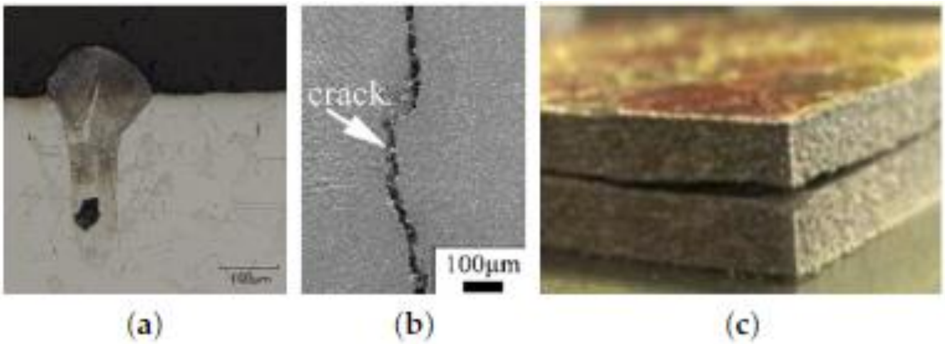

Figure 1.5. Examples of manufacturing defects arising in components obtained by L-PBF [13].

The repeated heating and cooling conditions on the workpiece generates large temperature gradients [21]. Thus, high levels of thermal residual stresses are induced in the produced part [22]. Accordingly, parts produced by L-PBF processes can comprise significant distortion, particularly in thin-walled features [23]. The tensile residual stresses have a detrimental effect on the mechanical performance of final parts, including premature failure during the building process [24] and poor fatigue performance [25]. Moreover, they affect the mechanical properties of the components [26]. Thus, the application of post-treatments to as-built parts (heat treatment and hot isostatic pressing) is a standard approach to homogenizing the microstructure, eliminate anisotropy and undesirable tensile residual stresses [27]. The stress relief heat treatment was modelled by [28] to study the effect of the post-processing parameters (temperature and dwell time) on the stress field in a simple cantilever beam produced in Ti6Al4V. The numerical results show that the plastic yielding contributes to approximately 25% of the reduction in the residual stresses.

The process parameters define the cooling rate and solidification mode, which have a strong influence on the resulting microstructure and mechanical properties. The L-PBF process comprise several parameters to be set [29], which can be divided into four groups: (i) laser beam; (ii) laser scanning; (iii) powder properties and (iv) build environment. Moreover, the interaction between process parameters is not clearly understood. Hence, a proper combination of process parameters is required to obtain a fully functional mechanical component. Currently, the process optimization is carried out by trial-and-error, relying on experimental campaigns, which are very expensive and time consuming [30]. Although the experimental approaches provide relevant physical insights into the AM processes, the in-situ measurement of some variables can be challenging, namely the residual stress field [31] and the temperature field. Thus, the adoption of virtual simulation tools is fundamental to accelerate the fine-tuning of the L-PBF process parameters [32].

Several computational methods have been recently developed for modelling L-PBF process, at different length- and time-scales [33]. The numerical models are commonly divided into three length scales: namely micro-, meso- and macro-scale models [34]. Micro-models deal with the melt pool dynamics, comprising the interaction between the laser beam and the powder particles [35]. The objective of the meso-models is the study of laser tracks, namely the interaction of the laser beam with the powder bed (usually assumed continuous). On the other hand, the macro-models address the entire geometry of the workpiece to be built, allowing the prediction of residual stress and part distortion. Figure 1.6 presents the macroscopic thermal finite element modelling of the L-PBF used in the building of an impeller with 4 spiral blades. This model allows to predict the temperature distribution and evolution in the build workpiece and non-melted powder during the L-PBF process at the macroscale.

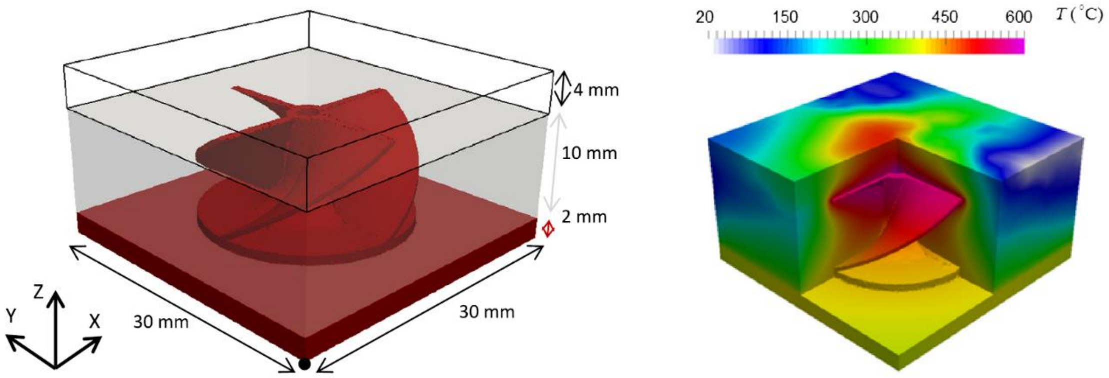

Figure 1.6. Description of the part to be constructed and temperature profile (after dwell time) obtained from the thermal finite element analysis [36].

The numerical simulation of the L-PBF process provide a proper understanding of the physics behind the manufacturing process, allowing to define the suitable process window [37], process optimization [38]. Nevertheless, the accurate and efficient numerical analysis of AM processes is very challenging, due to the multiphysics phenomena across multiple scales (see Figure 1.7). In fact, the challenges in the computational modelling are manifold: complex material behaviour, phase transitions, thermo-mechanical coupling, high temperature gradients, different length and time scales, etc. [39]. Thus, up to date, the numerical analysis is mainly focused on simple geometries [40,41]. In fact, the traditional thermo-mechanical modelling approaches require an impracticable high computational time to predict residual stresses and part distortion [42]. Consequently, multiscale modelling methods have been developed for an effective analysis of these processes [43]. The numerical simulation is crucial for understanding the complex relationship between process–structure–property–performance, in powder-based AM [44,45]. The study carried out by Mukherjee and Debroy [46] shows that a digital twin of 3D printing machine can reduce the number of trial-and-error tests, reduce defects and shorten time between the design and production.

Applying both 3D thermal simulation and experimental data, it was found that the scanning strategy affects the resulting thermal field and, consequently, the intensity of the developed thermal stresses and deformations [47]. Using different scanning strategies, the results shown that the proper selection of the scanning strategy is particularly important for parts with a surface of uniform dimensions in both directions than for parts featuring long and narrow plane surfaces.

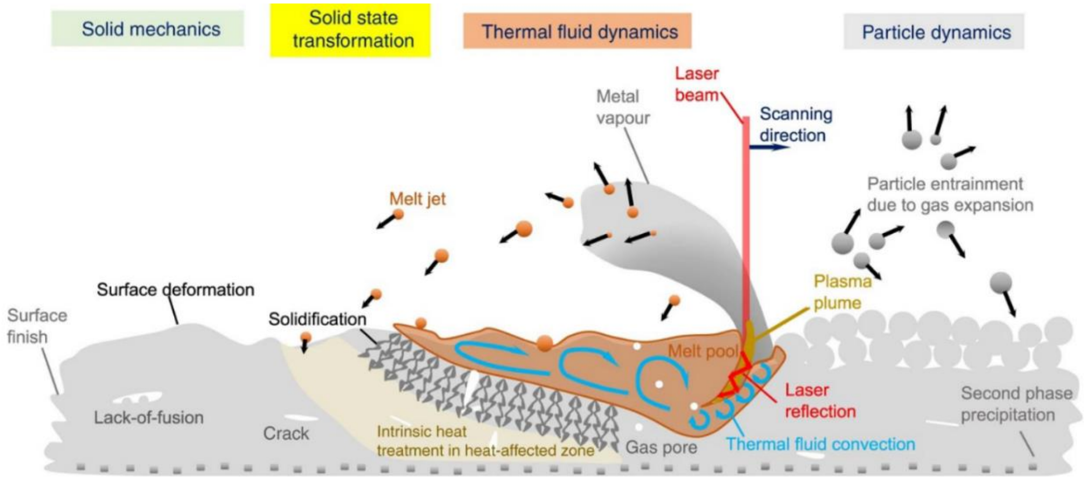
Solid mechanics
Solid state transformation
Thermal fluid dynamics
Particle dynamics
Laser beam
Metal vapour
Scanning direction
Melt jet
Particle entrainment due to gas expansion
Plasma plume
Surface deformation
Surface finish
Solidification
Melt pool
Laser reflection
Second phase precipitation
Lack-of-fusion
Crack
Intrinsic heat treatment in heat-affected zone
Gas pore
Thermal fluid convection

Figure 1.7. Physical effects and processes taking place during AM [48].

Aluminium alloys due to their low density, high specific strength-to-weight ratio and hight resistance against corrosion have a very broad field of application. However, the aluminium powders are not widely used in the L-PBF process due to some difficulties [49]. The high reflectivity of the aluminium increases the laser power required for melting. Besides, higher laser powers are required due the high thermal conductivity of the aluminium in comparison with other materials (steel and titanium), leading to the rapid dissipation of heat away from the scanned track. Nonetheless, the main obstacle to the effective melt processing of aluminium alloys is oxidation, leading to oxide formation inside the part [50]. Despite the oxygen present in the build chamber, the most important characteristics of the powder feedstock for L-PBF are the powder particle size distribution and the morphology [51].

The pore size, distribution, and morphology in AlSi10Mg samples built using L-PBF was studied by computed tomography on small volumes [52]. The measured pores ranged from under 5 µm up to slightly over 100 µm. Besides, they exhibited a range of shapes from spherical to ellipsoidal, as well as irregular morphologies. Substantial variations in the pore size distributions were found as a function of process conditions. The fabrication and characterization of high strength Al-Cu alloys processed using L-PBF was evaluated in [53], aiming to achieve a high relative density for the fabricated 3D structures. They concluded that the volumetric energy density is a rough indicator for high relative density parts, but with limited accuracy. The experimental tests showed that in order to achieve high relative densities a melting depth of approximately 3 layers was required.

1.3. Aims of the study and dissertation outline

The aim of the present work is to perform a numerical and experimental analysis of the L-PBF additive manufacturing process, considering two different aluminium alloys powder material (AlSi10Mg and Al-6.3Cu). The main objective is the proper selection of the process parameters for each aluminium alloy in order to obtain parts without manufacturing defects.

Additionally, the laser emission mode is studied, using continuous and pulsed laser modes. A design of experiments is proposed considering different combinations of laser power and scanning speed for single tracks deposited on the substrate. In addition to the single tracks, multi-layer geometries are also considered, namely hollow thin-wall cubes and cantilevers.

The effect of multi-layer deposition for a single track is evaluated using hollow thin-wall cubes, while the cantilevers are used for evaluated the residual stresses generated both during the manufacturing process and after the heat treatment. The numerical simulation of the L-PBF manufacturing process comprises the meso-scale analysis of each single track (also in the hollow thin-wall cubes) using the in-house developed finite element code DD3IMP and the macro-scale analysis of the cantilevers using the commercial code Simufact Additive. The numerical predictions are compared with the experimental measurements in order to assess the accuracy and reliability of the numerical models.

This section presents the structure of the work, as well as a brief summary of the topics covered in each chapter.

Chapter 1: presents the motivation for this study in the framework of the emerging additive manufacturing. A brief description of the L-PBF technology aluminium alloys is presented, highlighting the main advantages and drawbacks. The approaches currently adopted in the numerical modelling of this AM process are described, as well as the objectives for the present work.

Chapter 2: contains the experimental procedure, namely the characterization of the metallic powders (AlSi10Mg and Al-6.3Cu) and the design of experiments carried out for different build geometries. The manufacturing conditions adopted to build each part geometry (single tracks, thin-walls and cantilevers) are properly defined.

Chapter 3: describes in detail the finite element models used in the numerical simulation of the L-PBF process at different length-scales.

Chapter 4: presents the main results obtained in the present study, comprising both experimental measurements and numerical predictions.

Chapter 5: summarizes the main conclusions obtained from the results presented in the previous chapters.

2. EXPERIMENTAL PROCEDURE

The present study was carried out at the Welding and Quality Institute (ISQ: Instituto da Soldadura e da Qualidade), which is a private, independent and accredited entity. The ISQ offers engineering, consultancy, inspection and testing services and R&D and innovation activities. Present in 14 countries and with 7 offices in Portugal, ISQ is an organisation that provides scientific-technological support by promoting continuous improvement, innovation and the safety of people and property in industry and services. The development of the present research work was performed in the Welding and Additive Manfuacturing lab of ISQ Taguspark (Lisbon), which integrates the Materials and Technologies unity of the Research, Development and Innovation department.

2.1. Materials

Two different aluminium alloys were analysed in the present study, namely the AlSi10Mg and the Al-6.3Cu alloy. Both powders were inert gas atomized in order to obtain a spherical morphology and to minimize oxidation of the powder particles. The aluminium alloy AlSi10Mg comprises aluminium alloyed with silicon of mass fraction up to 10%, small quantities of magnesium and iron, along with other minor elements. The chemical composition of the powder, specified by the material supplier, is listed in Table 2.1.

Table 2.1. Chemical composition of the AlSi10Mg powder supplied by Renishaw (wt.-%).

Al	Si	Mg	Fe	N	O	Ti	Zn	Mn	Ni	Cu	Pb	Sn
Balance	9-11	0.25-0.45	<0.25	<0.20	<0.20	<0.15	<0.10	<0.10	<0.25	<0.25	<0.25	<0.25

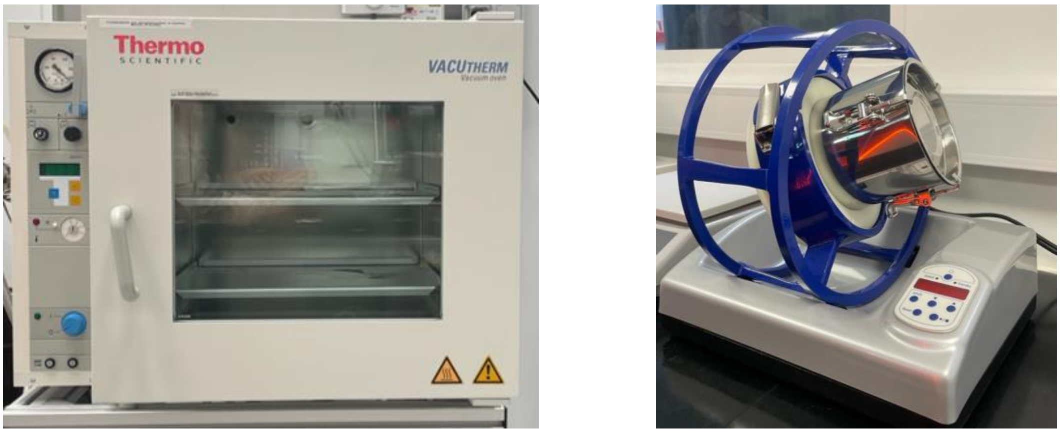

(a) (b)

Figure 2.1. Equipment used to prepare the Al-6.3Cu alloy for use in the L-PBF process: (a) drying oven used to remove the powders humidity; (b) drum hoop mixer device used for blend metal powders.

The Al-6.3Cu alloy was obtained by mixing pure aluminium and copper powders (99.9% of purity, supplied by Sigma Aldrich). Accordingly, the mixture comprises 63g of Cu powder and 937g of Al powder, resulting in 1kg of the Al-6.3Cu alloy for use in the L-PBF process. The powders were dried under vacuum for 1 h at 120ºC in the ThermoFisher Scientific VacuTherm VT 6060 M vacuum oven (see Figure 2.1 (a)). The powder mixture was obtained by mixing the two powders using a drum hoop mixer (JEL RRM Mini-II, J. Engelsmann AG) for 20 minutes at a speed of 35 rpm, as shown in Figure 2.1 (b).

The powder particle size distribution of each alloy (AlSi10Mg and Al-6.3Cu) was measured by dry-sieving. Four different sieves were adopted to segregate the powder particles into five size categories, namely size of 63µm, 45µm, 38µm, and 20µm. The sieving was performed in a CISA Sieve Shaker BA200N (Figure 2.2 (a)) during 15 minutes using an amplitude of 0.5 mm. For analysis of the cross-section of the powder particles, the sample was prepared using the manual grinder and polisher EcoMet30, which is shown in Figure 2.2 (b). The optical microscope used in the evaluation of particle morphology is shown in Figure 2.2 (c).

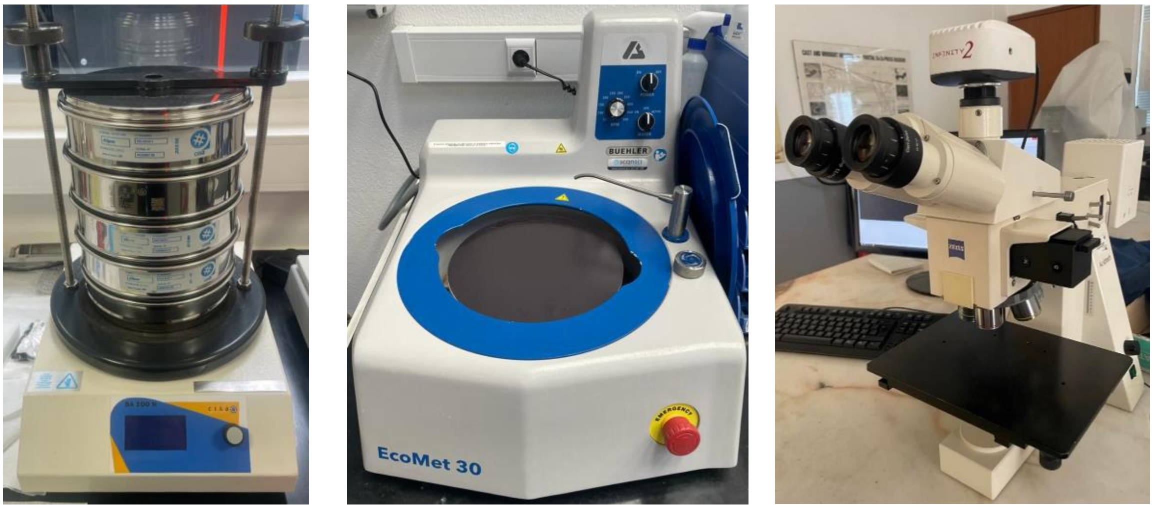
(a) (b) (c)

Figure 2.2. Equipment used in powder granulometry analysis: (a) CISA Sieve Shaker BA200N; (b) manual grinder and polisher EcoMet30; (c) Zeiss optical microscope.

2.2. Sample Preparation

The effect of the main process parameters on the final quality of the components obtained by L-PBF manufacturing process was evaluated using different geometries. Accordingly, a design of experiments was carried out considering different combinations of laser power and scanning speed for three different geometries: (i) single track scanning; (ii) hollow thin-wall cube; (iii) cantilever.

2.2.1. L-PBF equipment

All samples were manufactured using a Renishaw RenAM 500S Flex system, which is shown in Figure 2.3 (a). The RenAM 500S Flex system features a build volume of 250 mm × 250 mm × 350 mm. The system uses a 500 W ytterbium fiber laser (Yb:YAG) with a wavelength of 1070 nm and spot size of 80 μm, which operates under argon protective gas (purity of 99.999%) to prevent oxidation. In this study, samples were manufactured using continuous wave (CW) and modulated wave (MW) laser emission modes, with equivalent input energy densities.

The samples were produced with the reduced build volume (RBV) setup, which allows smaller builds, with a maximum build volume of 78 mm × 78 mm × 50 mm. The RBV is a tool to test new materials and parameters for use on AM systems. The geometry of the adopted substrate has a thickness of 9 mm and width of 77.4 mm. All the experiments were performed on AW5083 aluminium alloy substrates.

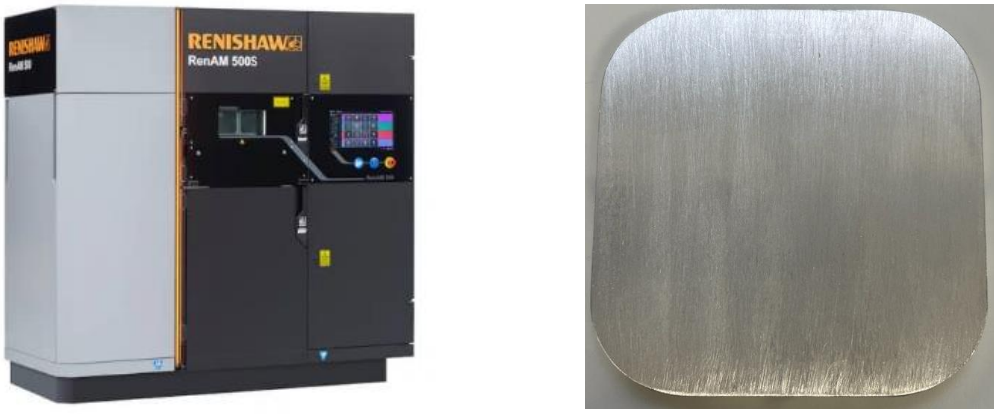

(a) (b)

Figure 2.3. Renishaw system for L-PBF additive manufacturing: (a) RenAM 500S Flex; (b) substrate geometry used in the reduced build volume.

2.2.2. Single track deposition

The effect of laser power and scanning speed on the single-track deposition quality was evaluated using a design of experiments. Hence, eighty different configurations of parameters were evaluated for the AlSi10Mg alloy, varying the laser power, the scanning speed and the laser emission mode. For the Al-6.3Cu alloy, sixty different combination of parameters were studied. In both cases, the thickness of the powder layer was 30 µm, the single-track length was 20 mm and the distance between adjacent tracks was 1.025 mm.

Figure 2.4 (a) presents the single tracks configuration for the AlSi10Mg alloy, as well as the set of process parameters adopted in each one. The laser power was varied between 100 W and 300 W, while the scanning speed was in the range 100 mm/s and 2500 mm/s. The laser emission mode was studied, comparing CW and the MW, as shown in Figure 2.4 (a). In the case of MW, the equivalent scanning speed is defined by the exposure time, which was 40 µs, and the point distance, which was between 4 µm and 100 µm.

Figure 2.4 (b) presents the configuration of the single tracks performed for the Al-6.3Cu alloy and the set of process parameters adopted in each one. In this case, the laser power was varied from 100 W to 300 W, with a scanning speed between 100 mm/s and 1500 mm/s. The reduction of the scanning speed range was a consequence of the results obtained for the larger values of scanning speed in the design of experiments carried out for

AlSi10Mg. Thus, the point distance range used in the MW was between 4 µm and 60 µm, keeping the exposure time in 40 µs.

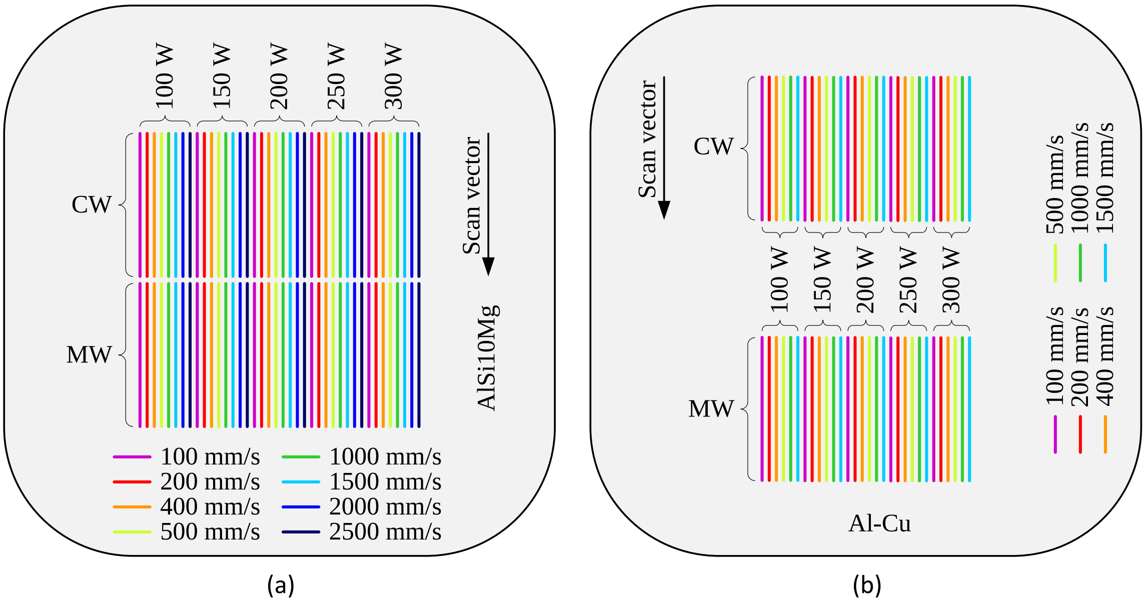
100 W
150 W
200 W
250 W
300 W
CW
MW
Scan vector
AlSi10Mg
100 mm/s
200 mm/s
400 mm/s
500 mm/s
1000 mm/s
1500 mm/s
2000 mm/s
2500 mm/s
(a)
Scan vector
CW
MW
100 W
150 W
200 W
250 W
300 W
500 mm/s
1000 mm/s
1500 mm/s
100 mm/s
200 mm/s
400 mm/s
Al-Cu
(b)

Figure 2.4. Configuration and process parameters used in the single-track scanning: (a) AlSi10Mg; (b) Al-6.3Cu powder mixture.

Figure 2.5 (a) and Figure 2.5 (b) present the experimental observation of the single tracks deposited on the substrate for the alloy AlSi10Mg and for the Al-6.3Cu powder mixture, respectively. The location of each single-track carried out in the design of experiments can be easily identified by comparing Figure 2.4 with Figure 2.5.

The melt-pool size obtained for each set of process parameters was indirectly assessed by measuring the single-track deposited on the substrate. Accordingly, the substrate was sectioned by abrasive cutting (Labotom-5 from Struers) in the transverse direction at mid-length of the track. The samples containing the cross-section of each single-track were embedded in resin and then grinded and polished using the same procedure previously used for the powder. The samples were etched by using Keller’s reagent for 30 seconds. Then, both the height, the depth and the width of each single-track were measured in the optical micrographs.

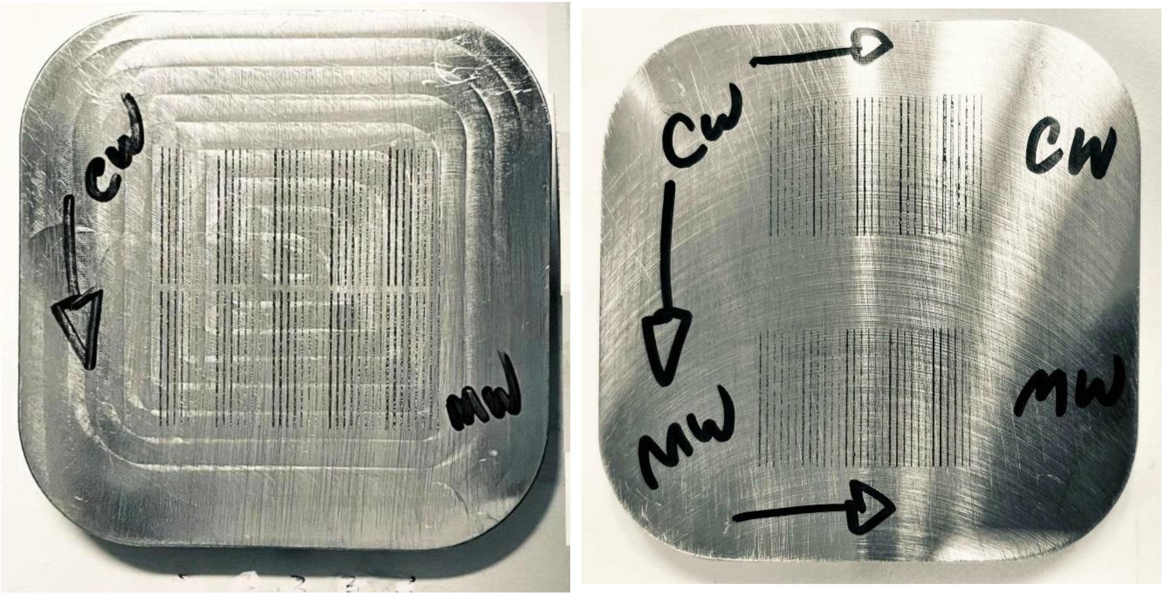

(a) (b)

Figure 2.5. Experimental observation of the single-tracks deposited on the substrate: (a) AlSi10Mg; (b) Al-6.3Cu powder mixture.

2.2.3. Hollow thin-wall cubes

To take into account the multi-layer feature of the L-PBF additive manufacturing process, hollow thin-wall cubes were built. The main dimensions of the geometry are shown in Figure 2.6, namely the top view and the lateral view of the geometry. The width of the rectangular cross-section is 3.4 mm and the length is 4 mm, while the height is 5 mm. The effect of the laser power, scanning speed and laser emission mode on the quality of the hollow thin-wall cube was evaluated using a design of experiments. Consequently, forty different configurations of parameters were evaluated for the AlSi10Mg alloy. The thickness of the powder layer was 60 μm, while each cross-section of the hollow thin-wall cube was built using a single scan strategy (perimeter in the clockwise direction).

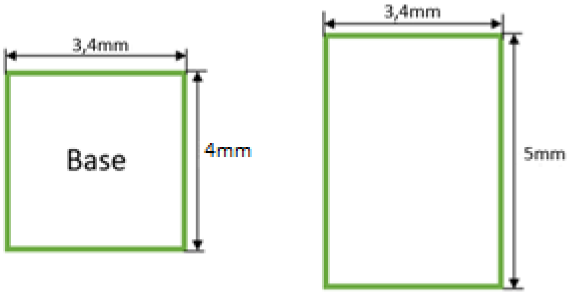

Figure 2.6. Geometry and main dimensions of the hollow thin-wall cube produced by L-PBF.

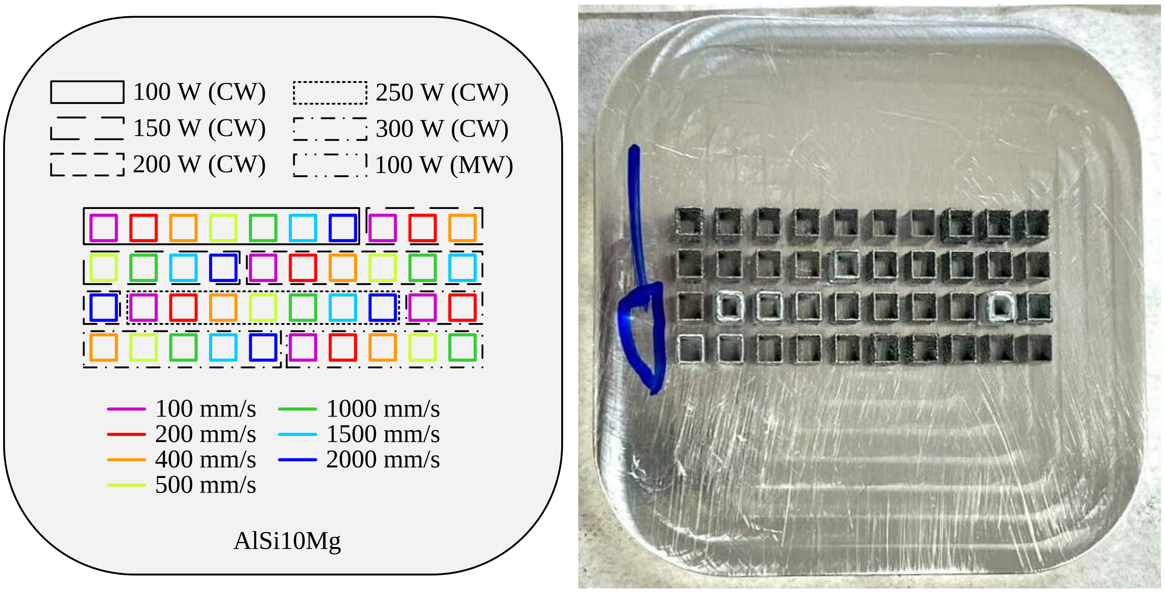

(a) (b)

Figure 2.7. Hollow thin-wall cubes of AlSi10Mg: (a) configuration of the process parameters; (b) experimental observation.

Figure 2.7 (a) presents the distribution of the hollow thin-wall cubes on the substrate for the AlSi10Mg alloy, including the set of process parameters adopted in each case. The laser power was varied between 100 W and 300 W, with a scanning speed from 100 mm/s to 2000 mm/s. The laser emission mode was also studied, but the comparison between CW and MW was carried out only for 100 W of laser power and up to 1000 mm/s of scanning speed, as shown in Figure 2.7 (a). Accordingly, for the MW laser emission the exposure time was 40 μs and the point distance was varied between 4 μm and 40 μm. Figure 2.7 (b) presents the top view of the hollow thin-wall cubes built on the substrate.

2.2.4. Cantilevers

To evaluate the level of residual stresses in the parts produced by L-PBF additive manufacturing process, cantilevers with different set of parameters were built with the AlSi10Mg powder. Figure 2.8 presents the geometry and the main dimensions of the adopted cantilever beam. After the printing process, the cantilever is only partially removed from the substrate. All the thin vertical supports are cut, but the left-most bulky part of the cantilever remains attached to the substrate. Subsequently, the cantilever deformed mainly due to the normal stress along the cantilever length.

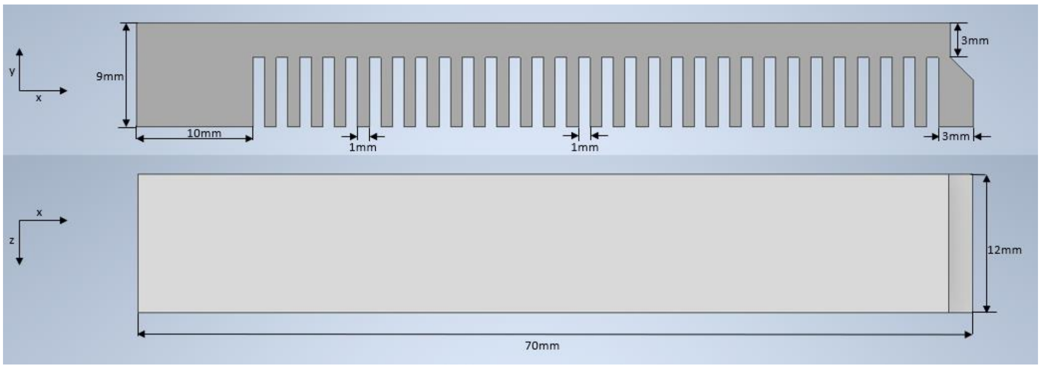

Figure 2.8. Geometry and main dimensions of the cantilever used to evaluate the residual stresses.

The effect of both the laser power, the scanning speed, the hatch distance, the layer thickness and the laser emission mode were evaluated for the cantilever geometry using a design of experiments. Consequently, eight different combinations of process parameters were evaluated for the aluminium alloy AlSi10Mg, which are listed in Table 2.2. The set of parameters was selected according to the results obtained for hollow thin-wall cubes, namely the uniformity of the wall. In all cases, the laser scanning strategy adopted was the meander with an interlayer rotation of 67º. The thickness of each powder layer was 60 µm, except for the cantilever #7, which uses all process parameters recommended by Renishaw company for the aluminium alloy AlSi10Mg (30 µm of powder layer thickness). The design of experiments comprises values of laser power ranging between 100 W and 300 W, while the scanning speed ranges between 100 mm/s and 2250 mm/s. The values of hatch distance selected for the cantilevers are identical to the measured wall thickness for the same values of laser power and scanning speed. Hence, the hatch distance ranges between 0.09 mm and 0.628 mm, as shown in Table 2.2. The volumetric energy density (VED, J/mm^3) used in each cantilever is listed in Table 2.2, which was calculated by:

$$\boldsymbol{VED} = \frac{\boldsymbol{P}}{\boldsymbol{v} \times \boldsymbol{h} \times \boldsymbol{t}} \tag{2.1}$$

where P denotes the laser power, v is the scanning speed, h is the hatch distance and t defines the layer thickness.

Table 2.2. Definition of the process parameters used in each cantilever built with AlSi10Mg powder. VED is the volumetric energy density in J/mm³.

Cantilever ID	Laser power [W]	Scanning speed [mm/s]	Hatch distance [mm]	Layer thickness [μm]	Laser mode	VED (J/mm^3)
1	200	200	0.225	60	CW	74.1
2	200	500	0.135	60	CW	49.4
3	250	500	0.195	60	CW	42.7
4	250	1000	0.123	60	CW	33.9
5	300	100	0.628	60	CW	79.6
6	300	500	0.325	60	CW	30.8
7	350	2250	0.090	30	MW	57.6
8	100	500	0.110	60	MW	30.3

Figure 2.9 presents the obtained cantilevers according to the process parameters listed in Table 2.2. Due to the small size of the substrate used in the RBV, each substrate comprises at maximum 3 cantilevers, requiring the use of 3 substrates to complete the design of experiments. In order to evaluate the geometric distortion induced by the thermal stress, each cantilever was cut from the substrate using wire electrical discharge machining (wire-EDM, outsourced). After cutting from the substrate, the cantilever will bend upwards. The distortion of each cantilever was measured before and after the removal from the substrate using a profilometer Mitutoyo surface test SJ-410, as shown in Figure 2.10. The profile of the upper surface of each cantilever was evaluated along the entire length and at the half-width of the cantilever.

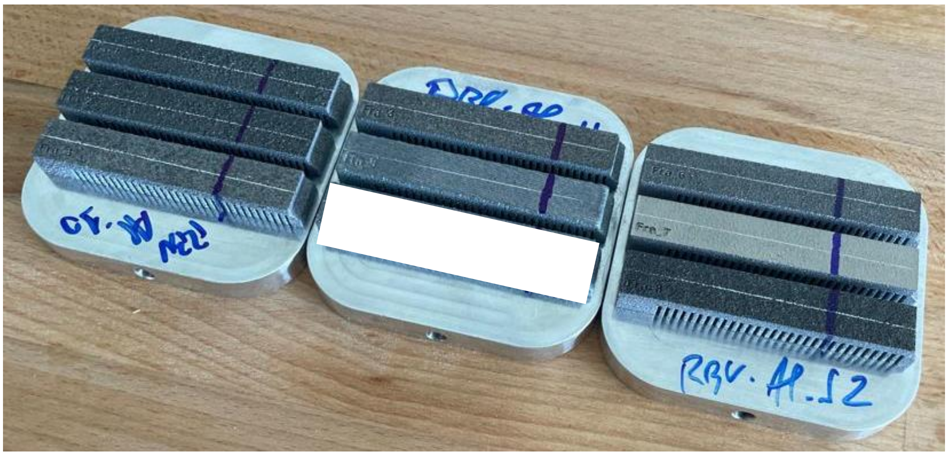

Figure 2.9. Printed cantilevers for AlSi10Mg using different combinations of process parameters (beam power, scanning speed, hatch distance, layer thickness and laser mode).

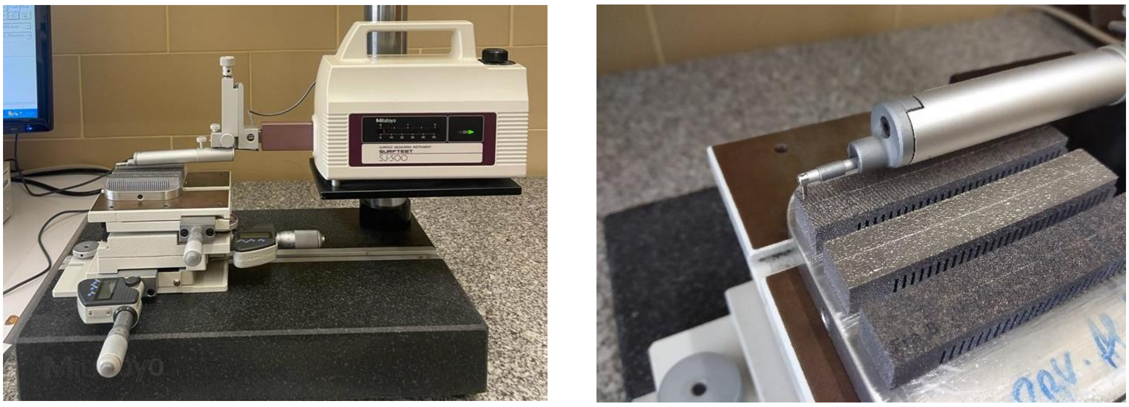
(a) (b)

Figure 2.10. Measuring the cantilever profile with Mitutoyo surface test SJ-500: (a) experimental setup; (b) detail of the probe during the measurement.

2.3. Heat treatment

The successive thermal cycles arising in the L-PBF leads to the generation of severe residual stresses in the built components. The residual stresses are largely spatially non-uniform, which can be detrimental for the mechanical properties. Also, during the building process, they can reduce the dimensional accuracy and lead to geometrical defects, such as distortion and layer delamination [13]. Accordingly, heat treatment for residual stress relief is a common practice in L-PBF. Usually, it is applied before the produced parts are cut from the substrate to avoid distortion. According to [54], the heat treatment conditions must be chosen carefully to avoid undesirable phenomena such as precipitation or phase changes. The proper selection of the heat treatment parameters can lead to a reduction of the residual stresses in about 70-90%.

The effect of the heat treatment on the residual stresses was evaluated in the present study for the cantilever geometry obtained with the printing process parameters suggested by Renishaw (cantilever #7 in Table 2.2). Hence, two cantilevers produced under identical conditions, one of which was submitted to a heat treatment and the other without post-processing heat treatment. The procedure adopted in the heat treatment was according to Renishaw. The parts were incorporated into protective gas boxes containing argon (three purges were performed) and then placed inside the furnace (Nabertherm NW200 in Figure

2.11). This thermal treatment consisted of heating to 300ºC and keeping the cantilever at for 2 hours and then slowly cooling down inside the furnace.

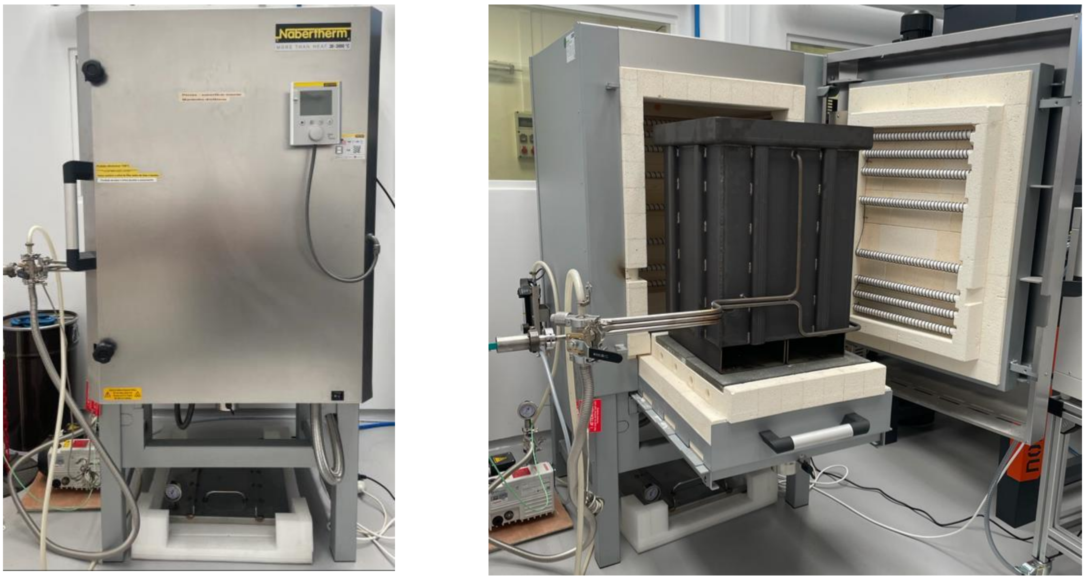

Figure 2.11. Oven Nabertherm NW200 used in the heat treatment of the cantilevers.

3. FINITE ELEMENT MODELLING

3.1. Meso-scale modelling

The numerical analysis of the L-PBF additive manufacturing process can be carried out at meso-scale, allowing the study of the interaction of the laser beam with the powder layer. In the present work, the meso-scale thermal analysis was carried out using the in-house finite element code DD3IMP. The evolution of the temperature field during the deposition of single tracks can be predicted, by replicating the design of experiments described in Section 2.2.2 and 2.2.3.

3.1.1. Transient thermal analysis

The differential equation governing the transient heat conduction, within a continuous medium with arbitrary volume, can be derived from the first law of thermodynamic. The solution of the heat equation provides the temperature *T* with respect to time *t*, expressed as follows:

$$k\left(\frac{\partial^2 T}{\partial x^2}+\frac{\partial^2 T}{\partial y^2}+\frac{\partial^2 T}{\partial z^2}\right)+\dot{q}=\rho c_p\frac{\partial T}{\partial t}\,, \tag{3.1}$$

Where k is the thermal conductivity coefficient, ρ denotes the mass density, c_p is the specific heat and $\dot{q}$ is the power generated per volume in the workpiece. In order to take into account the effects of Marangoni convection on the melt pool, the thermal conductivity of the liquid is artificially increased [55]. The proposed model considers the heat loss by convection and radiation between the exposed powder bed surface and the environment. The heat exchange by convection to the environment on the top surface of the powder bed is determined by:

$$q_c = h_c(T - T_0) \tag{3.2}$$

where h_c is the convective heat transfer coefficient and T_0 is the environment temperature. A value of 5 W/(m^{2}K) was chosen for h_c to account for free convection. The remaining surfaces (side walls and bottom surface) are assumed thermally isolated. The radiative heat losses were accounted for the top surface of the powder bed, given by:

$$q_r = \varepsilon\sigma(T^4 - T_0^4)$$

where ε is the surface emissivity, which was taken as 0.8 and σ is the Stefan Boltzmann constant and T_0 is the environment temperature T_0=290 K.

3.1.2. Heat source

Due to the powder bed packing density, the incident laser radiation is reflected between the particles, increasing the absorption depth in comparison to bulk solid. Thus, the laser heat input is modelled by the volumetric Gaussian heat source proposed by Goldak et al. [56]. The power density distribution for a hemispherical shape heat source model can be expressed as:

$$\dot{q} = \frac{2\beta P}{\pi r_0^3} exp\left\{-2\frac{x^2+y^2+z^2}{r_0^2}\right\} \quad (3.3)$$

where P is the power of the laser source, β is the absorptivity and r_0 denotes the radius of the laser beam. The absorptivity of 18% for AlSi10Mg powder material is used according to [57]. The radius of the laser beam adopted in the numerical simulations was 40 µm. The schematic diagram of laser beam irradiating on the powder bed surface is presented in Figure 3.1, highlighting the Gaussian distribution of the power density.

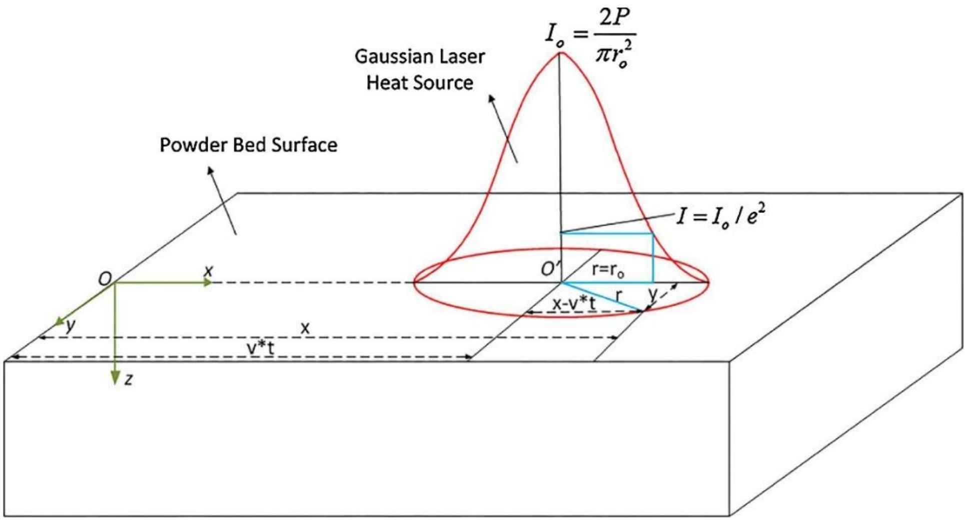

Figure 3.1. Schematic diagram of laser beam irradiating on the powder bed surface [58].

The numerical modelling of the laser emission modes is presented in Figure 3.2 for P=200 W, comparing the CW and the MW for equivalent values of scanning speed (400 mm/s). While in the CW the laser is always switch on, in the case of the MW the laser is on (30 µs) and off (10 µs), which corresponds to 40 µs of exposure time. Besides, the point distance is 16 µm in CW laser mode, as shown in Figure 3.2.

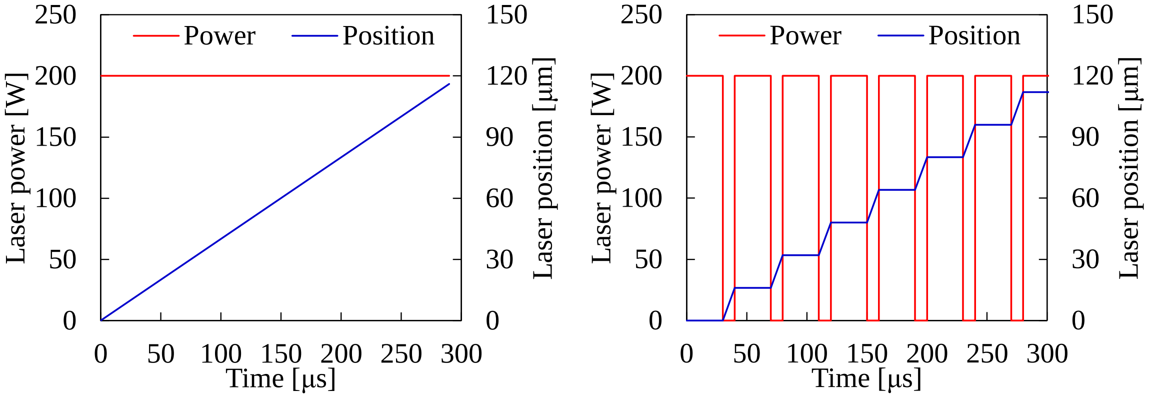

(a)

(b)

Figure 3.2. Modelling the laser emission modes for P=200 W: (a) CW and v=400 mm/s; (b) MW with 40 µs of exposure time and 16 µm of point distance.

3.1.3. Numerical model

Since the L-PBF process comprises the material phase transformation from powder to liquid, which then cools down to solidification, three material phases were considered in the simulation: powder, solid and liquid. The powder material switches to liquid when the temperature rises to the melting point (840 K) and the liquid material solidifies when the temperature cools down to the melting point (bidirectional transformation). All thermal and physical properties were assumed constant in the numerical simulation (see Table 3.1). In order to account for the convective heat transfer within the melt pool, the thermal conductivity coefficient of the liquid phase was artificially increased up to 800 W/mK. On the other hand, mass density of the powder phase was 60% of the solid AlSi10Mg, due to the assumption of 0.6 for the packing factor of the powder bed. Besides, the adopted thermal conductivity coefficient of the powder was 10 times smaller than that of the same bulk material due to the porosity in the powder bed [59].

Table 3.1. Thermo-physical properties of AlSi10Mg (solid material) [source: Addimen].

ρ [kg/m^3]	c_p [J/kg·K]	k [W/m·K]	T_m [K]
2680	900	160	840

The geometry of the initial domain used in the thermal modelling of the single-track deposition is presented in Figure 3.3 (a). The substrate is a parallelepiped with 3.5 mm length, 1 mm half-width and 1 mm of thickness. Due to symmetry conditions, only half width is modelled, as shown in Figure 3.3. The thickness of the powder layer is 30 μm in the region above the substrate. The adopted non-conforming finite element mesh (3 levels of mesh refinement) is composed by 158,340 hexahedral linear finite elements, as shown in Figure 3.3 (b). In order to reduce the computational cost, the mesh is refined only in the vicinity of the laser scan vector, which has 1.5 mm of length. Accordingly, the minimum element size is 4 μm in both longitudinal and transversal directions, while in the vertical direction is 3.75 μm.

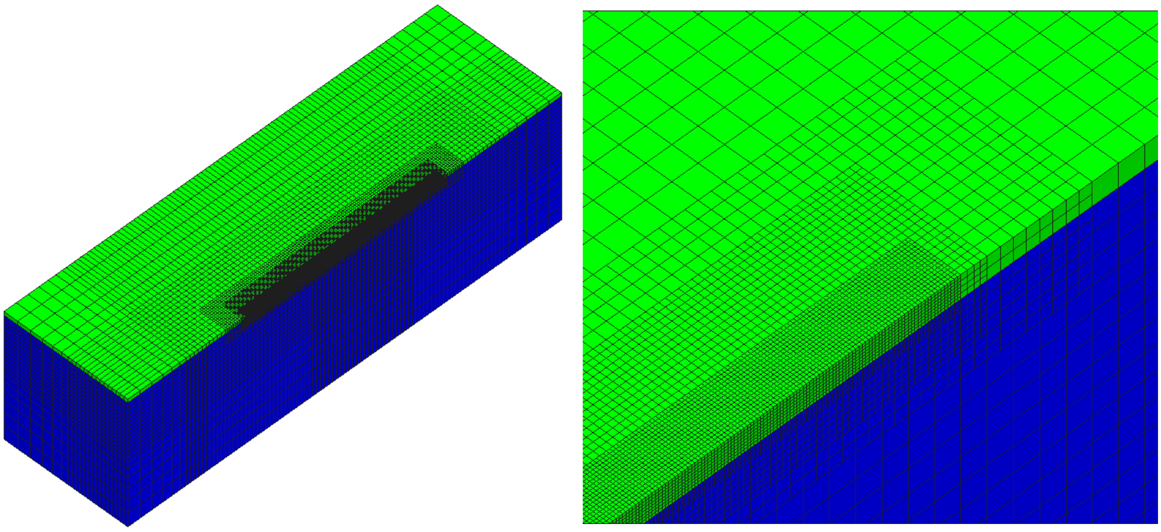

(a) (b)

Figure 3.3. Geometry and finite element mesh used in the numerical modelling of the single-track scanning: (a) solution domain composed by the substrate and powder layer; (b) detail of the mesh around the symmetry plane.

Figure 3.4 presents the geometry of the domain used in the thermal modelling of the hollow thin-wall cubes. In order to avoid the numerical issues related with the multi-layer deposition modelling, a single layer deposition was studied considering a multi-track deposition (four edges). Nevertheless, the 40th layer deposition was selected to avoid the deposition of the first couple of layers, which can be significantly influenced by the closer presence of the substrate. Therefore, this layer was scanned over solidified layers of the hollow thin-wall cube, i.e. the initial wall has 2.34 mm of height, as shown in Figure 3.4 (b). Since the thickness of the additively manufactured hollow cube is strongly dependent of the selected process parameters, namely laser power and scanning speed, two different values of wall thickness were considered in the model (t_0=0.2 mm and t_0=0.4 mm). The thickness of each powder layer is 60 μm but the total powder bed height after the current layer deposition is 2.4 mm, as shown in Figure 3.4 (a). The substrate is a parallelepiped with 6 mm × 6 mm × 4.80 mm, while the cross section of the hollow cube presents 4 mm of length and 3.4 mm of width. The adopted non-conforming finite element mesh (4 levels of mesh refinement) is composed by 99,534 hexahedral linear finite elements, as shown in Figure 3.4 (c). In order to reduce the computational cost, the mesh is refined only in the vicinity of each laser scan vector. Accordingly, the minimum element size is 25 μm in both longitudinal and transversal directions, while in the vertical direction is 30 μm.

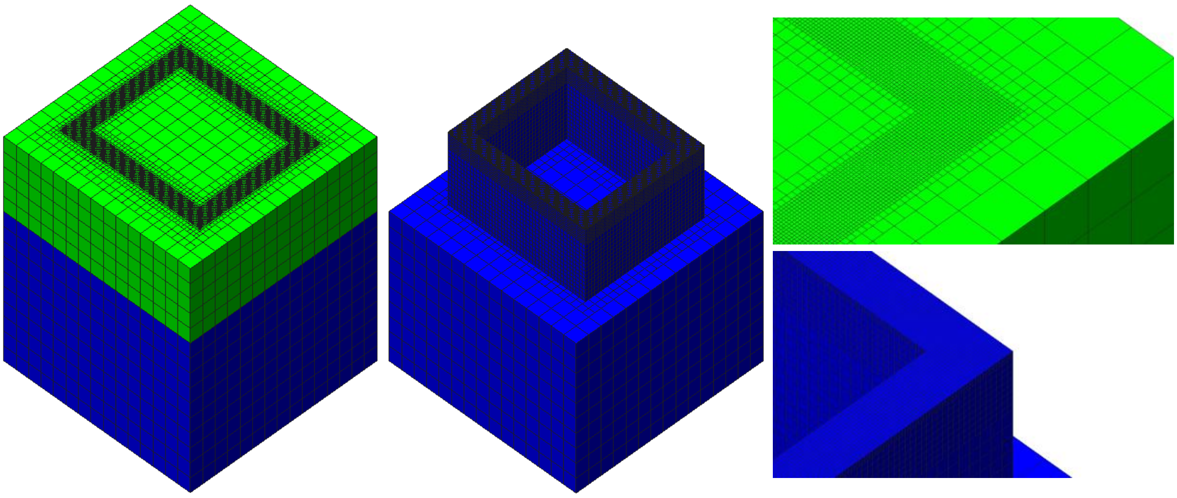
(a) (b) (c)

Figure 3.4. Geometry and finite element mesh used in the numerical modelling of the hollow thin-wall cube: (a) entire solution domain; (b) solution domain without powder; (c) detail of the mesh in the corner.

3.2. Macro-scale modelling

In the present study, the numerical analysis of the L-PBF additive manufacturing process at macro-scale is carried out resorting to the commercial software package Simufact

Additive. This mechanical analysis allows to predict residual stresses and distortions in real (macro) build geometries. The printing process of the cantilever geometry can be evaluated in detail, including the effect of the heat treatment on the resulting sample deflection after cutting operation.

3.2.1. Simufact Additive

Simufact Additive is a commercial software solution for the simulation of metal-based additive manufacturing processes. This software package cover two different process: (i) Powder Bed Fusion Processes; (ii) Metal Binder Jetting. The module regarding the metal powder bed fusion process, which will be adopted in the present study, contains three options: mechanical, thermal and thermo-mechanical. Nevertheless, only the mechanical module was used for this study. This software uses the following numerical methods for modelling the L-PBF process and to predict part distortion: (a) Finite Element Method (FEM); (b) Inherent Strain Method.

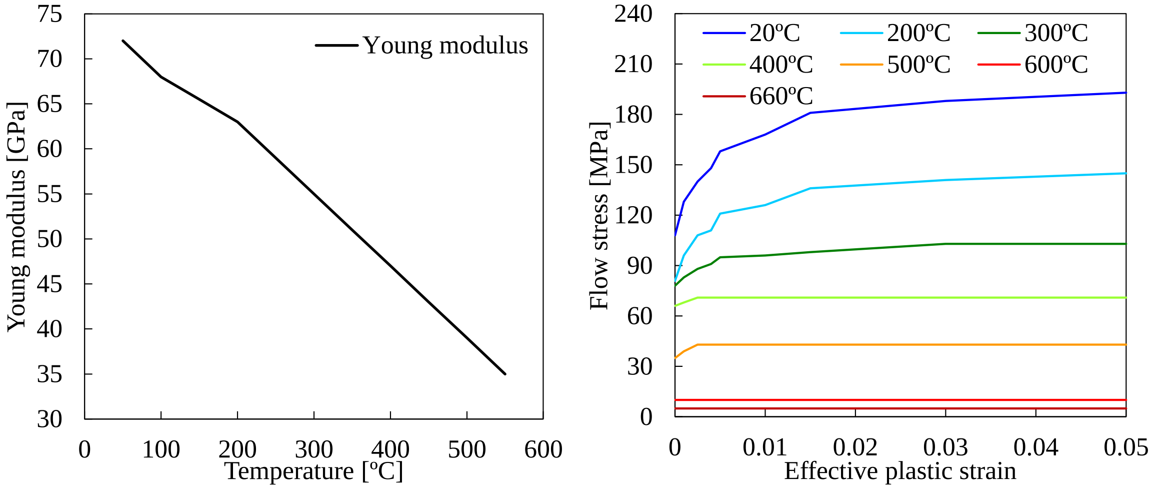

(a) (b)

Figure 3.5. Effect of temperature on the mechanical properties of AlSi10Mg: (a) Young modulus; (b) flow stress evolution [source: Simufact material database].

Since the purpose of the macro-scale simulation is the printing process of the cantilever (see Figure 2.8), the geometry was imported to the Simufact Additive using the STEP file. Since this geometry does not requires support structures, the cantilever is placed directly over the substrate (assumed rigid in the simulation). The powder material properties of the AlSi10Mg used in the numerical analysis were obtained from the software library. Figure 3.5 (a) presents the evolution of the Young modulus with the temperature required to define the elastic behaviour, together with the Poisson ration of 0.34. The effect of the temperature on the flow stress curves is presented in Figure 3.5 (b), highlighting the reduction of the material strength with the temperature increase. The thermal expansion coefficient adopted for AlSi10Mg was 2.06×10^{-5} 1/K.

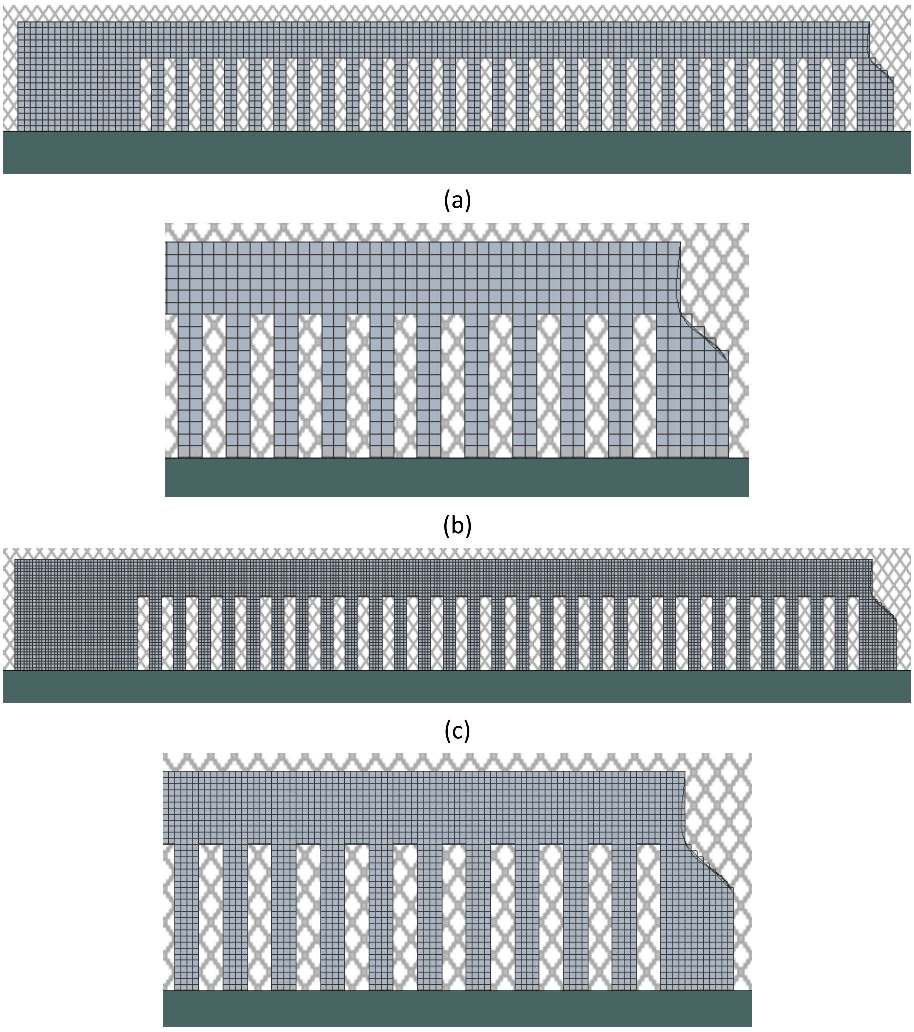

(a)

(b)

(c)

(d)

Figure 3.6. Finite element mesh used in the simulation of the cantilever geometry: (a) global lateral view of the coarse mesh (element size: 0.5 mm); (b) detail of the coarse mesh; (c) global lateral view of the fine mesh (element size: 0.25 mm); (d) detail of the fine mesh

Hexahedral finite elements (voxel elements) are used in the numerical simulation. The discretization of the cantilever geometry was carried out using two different meshes, which are presented in Figure 3.6. The element size of the coarse mesh is 0.5 mm, while the fine mesh contains elements with 0.25 mm of size. The total number of elements defining the fine mesh is about 8 times larger than in the coarse mesh. The cutting stage simulates a cut through the defined horizontal plane to partially detach the cantilever from the base plate in multiple time steps. This cutting operation was carried out after the build operation, using eight time steps to gradually release the cantilevers from the substrate (cutting from the right-side to the left-side).

3.2.2. Inherent strain method

The Simufact Additive software predicts residual stress and part distortion through the inherent strain method, which has been successfully adapted to L-PBF processes in a multi-scale [60]. The inherent strain method employs strains that are inherited from the thermo-mechanical process and allows for calculation of the deformed shape. The strategy reduces the complex thermo-mechanical simulation to a mechanical analysis, which makes the simulation much faster while having a limited trade off in accuracy. The trade-off commonly affects stresses that may be predicted less accurately in some cases than they would be with an in-depth thermo-mechanical analysis.

The inherent strain is the sum of the strains due to plastic deformation, thermal expansion and phase changes. If the total strain developed during a laser scan is e^{tot} and the elastic strain is denoted by e^{e}, then:

$$e^{tot} = e^{e} + e^{p} + e^{t} + e^{phase} \tag{3.4}$$

where e^{p} is the plastic deformation, e^{t} is the strain due to the thermal expansion and e^{phase}, denotes the strain due to phase changes. Then, the inherent strain is defined by:

$$e^{*} = e^{tot} - e^{e}. \tag{3.5}$$

This strain is used as the initial strain to calculate the residual stress and the distortion developed during the building process. The system of equations used in FEM for static mechanical analysis of elastic materials is:

$$[K]\{u\} = \{f^{*}\} \tag{3.6}$$

where $[K]$, $\{u\}$ and $\{f^*\}$ represent the elastic stiffness matrix, nodal displacement vector and nodal force vector induced by the inherent strain, respectively.

The numerical prediction of residual stresses and part distortion using the macro-scale part model requires the calibration of the inherent strain. The calibration procedure for the inherent strain takes into account a combination of machine, process parameters and material. The idea behind the algorithm is the comparison of simulation data with experimental measurements. Simufact Additive recommends the building of a cantilever, which is then partially cut off from the build platform to measure bending. The bending value of the cantilever, along with the process conditions, is used to calculate inherent strain in the calibration procedure. Note that for every combination of material and process parameters, a new calibration is required [61].

The calibration procedure can be divided into two categories: isotropic and orthotropic inherent strains. In the isotropic calibration, the inherent strains in x-direction are set equal to the strains in y-direction $\varepsilon_{xx}=\varepsilon_{yy}$, while the orthotropic calibration considers $\varepsilon_{xx}\neq\varepsilon_{yy}$. Therefore, isotropic calibration requires the manufacturing of a single cantilever, while the orthotropic calibration requires the manufacturing of at least two cantilevers, one in x and one in y direction. Figure 3.7 presents the menu of the Simufact Additive used to define the starting values for the inherent strains used in the calibration procedure. The default values for AlSi10Mg are listed in Table 3.2, which were adopted in the numerical simulations of the cantilever.

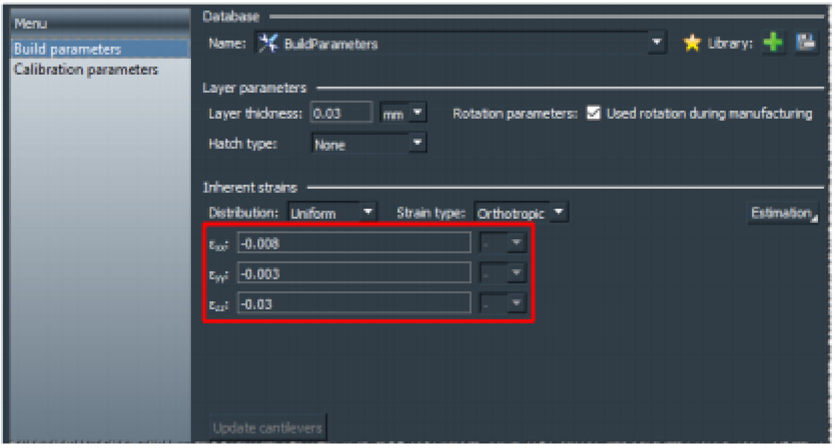

Name: BuildParameters
Layer thickness: 0.03 mm
Rotation parameters: ☑ Used rotation during manufacturing
Hatch type: None
Distribution: Uniform
Strain type: Orthotropic
ε_{xx}: -0.008
ε_{yy}: -0.003
ε_{zz}: -0.03

Figure 3.7. Menu of Simufact Additive containing the starting values for the inherent strains used in the calibration procedure.

Table 3.2. Default values of each component of the inherent strain for AlSi10Mg.

ε_{xx}	ε_{yy}	ε_{zz}
-0.0058	-0.0022	-0.03

4. RESULTS AND DISCUSSION

4.1. Powder granulometry

Figure 4.1 (a) presents the obtained powder particle size distribution of the AlSi10Mg alloy. The mean particle size calculated from cumulative weight is between 45 µm and 63 µm. In addition to particle size, particle morphology was also measured for AlSi10Mg. Thus, Figure 4.1 (b) presents the cross-section of powder particles obtained under a microscope after to determine the particles shape, which is approximately spherical.

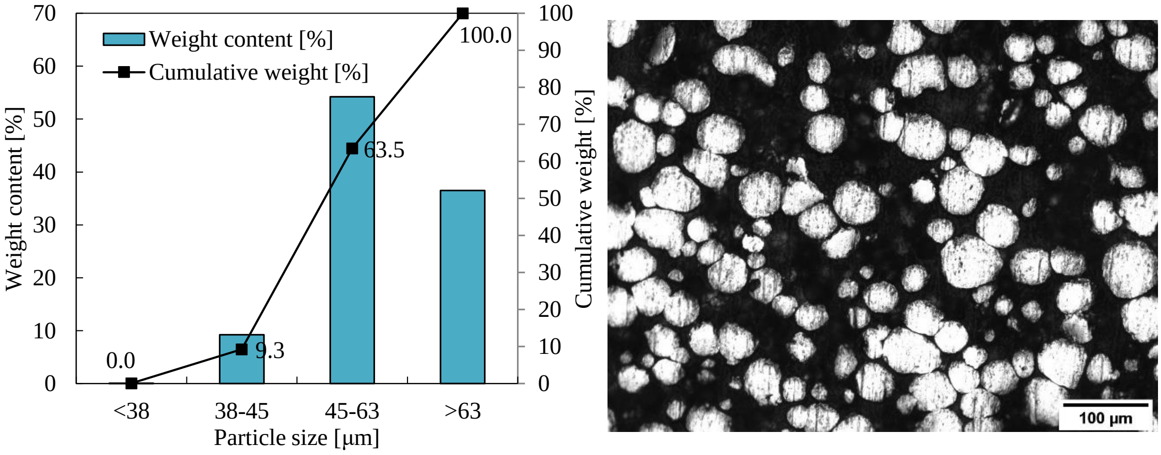

(a) (b)

Figure 4.1. Characterization of the AlSi10Mg powder: (a) particle size distribution; (b) cross-section of the powder particles.

Figure 4.2 (a) and Figure 4.2 (c) presents the powder particle size distribution of pure Al and pure Cu, respectively. The Al powder particles has a $d_{50} \approx 55$ µm, which is the same range as the AlSi10Mg powder. On the other hand, the Cu powder particles shows a $d_{50} \approx 45$ µm, which is slightly smaller than pure Al powder. The particle morphology for Al and Cu is shown in Figure 4.2 (b) and Figure 4.2 (d), respectively. The powder particles shape is approximately spherical, particularly in the case of the Cu powder.

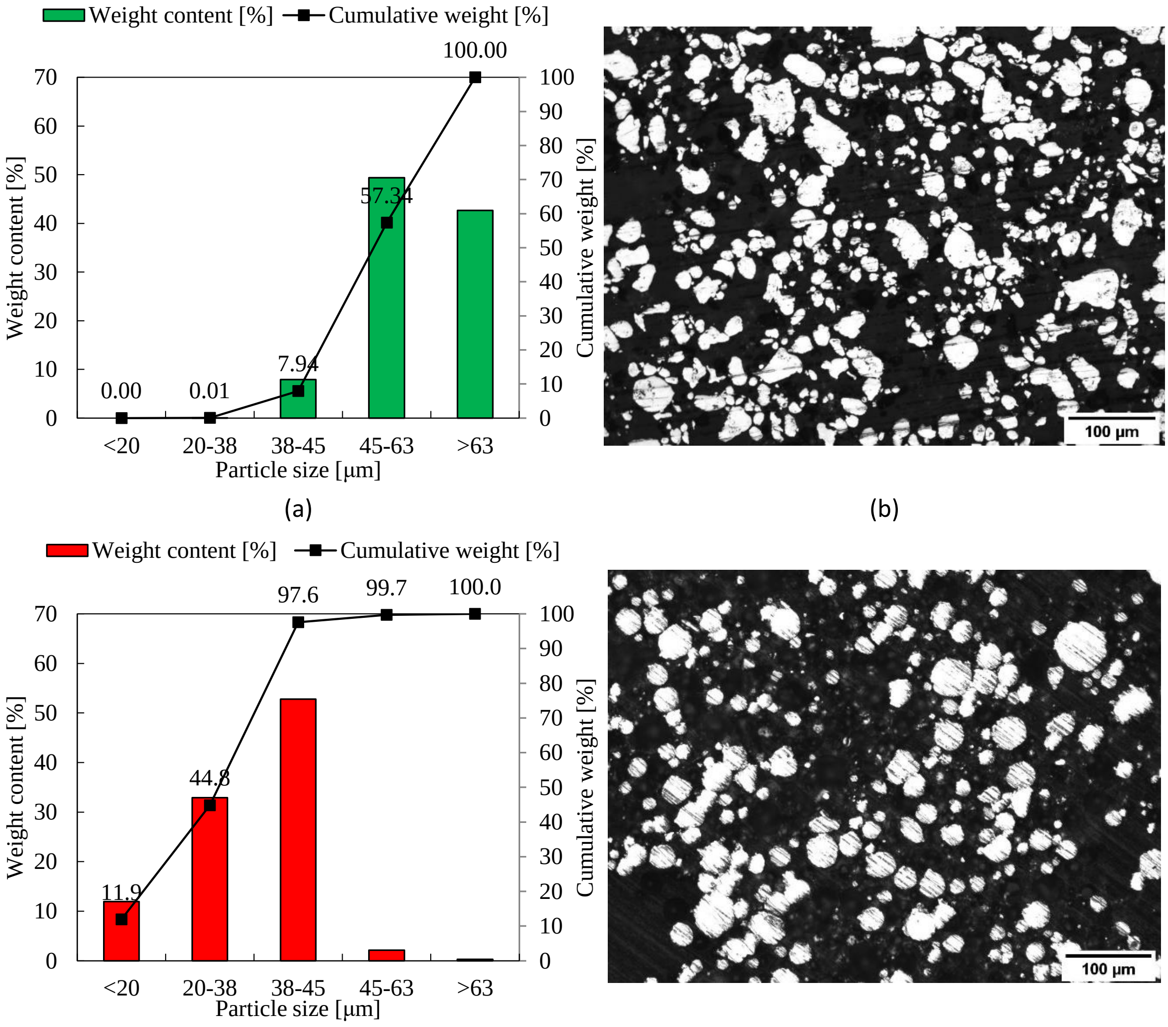

(a) (b)

(c) (d)

Figure 4.2. Characterization of pure powder: (a) particle size distribution of Al powder; (b) cross-section of Al powder particles; (c) particle size distribution of Cu powder; (d) cross-section of Cu powder particles.

4.2. Single track scanning

The design of experiences applied to the single tracks comprises eighty different set parameters for AlSi10Mg and sixty different set parameters for Al-6.3Cu alloy. Both experimental and numerical analysis was performed to identify the proper combination of process parameters to obtain uniform tracks.

4.2.1. Single track quality

Figure 4.3 presents the top view of the single tracks of the AlSi10Mg alloy built with different values of laser power and scanning speed. Globally, the track width increases either increasing the laser power or decreasing the scanning speed. Nevertheless, with a lower laser power and higher scanning speed the track is missing or discontinuous. Considering the laser power of 100 W, the track is missing for scanning speed values larger than 500 mm/s. On the other hand, for large values of power and small values of scanning speed overmelting is observed, namely for the lowest scanning speed (100 mm/s) and values of power larger than 200 W. The influence of the laser emission mode (CW or MW) on the deposition quality is not evident by visual inspection.

The top view of the single tracks of Al-6.3Cu built with different values of laser power and scanning speed is shown in Figure 4.4, comparing the two laser emission modes evaluated. The same trend is observed for the Al-6.3Cu alloy regarding the effect of the process parameters. However, for the same set of process parameters, the scanned track is more uniform using Al-6.3Cu in comparison with AlSi10Mg, as shown by comparing Figure 4.3 and Figure 4.4. Besides, the width of the scan track seems more uniform using the MW laser mode, particularly for the highest laser power and lower scanning speed (see Figure 4.4). This is a consequence pulsed mode of the laser, which avoids long stretching of the melt pool as in the continuous laser mode.

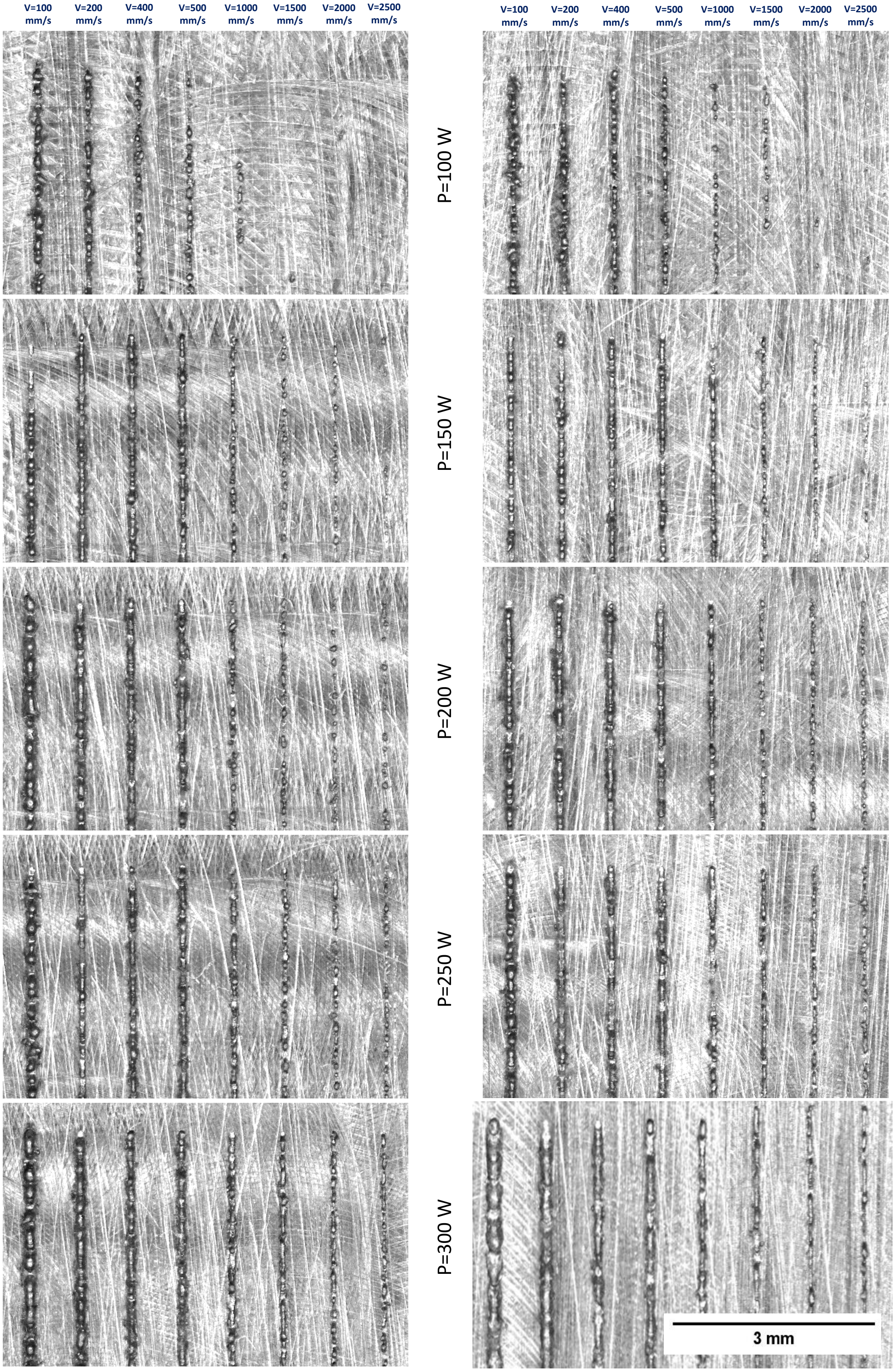
V=100 mm/s
V=200 mm/s
V=400 mm/s
V=500 mm/s
V=1000 mm/s
V=1500 mm/s
V=2000 mm/s
V=2500 mm/s
P=100 W
P=150 W
P=200 W
P=250 W
P=300 W
3 mm

(a) (b)

Figure 4.3. Design of experiments for single-track scanning of AlSi10Mg for laser mode: (a) CW; (b) MW.

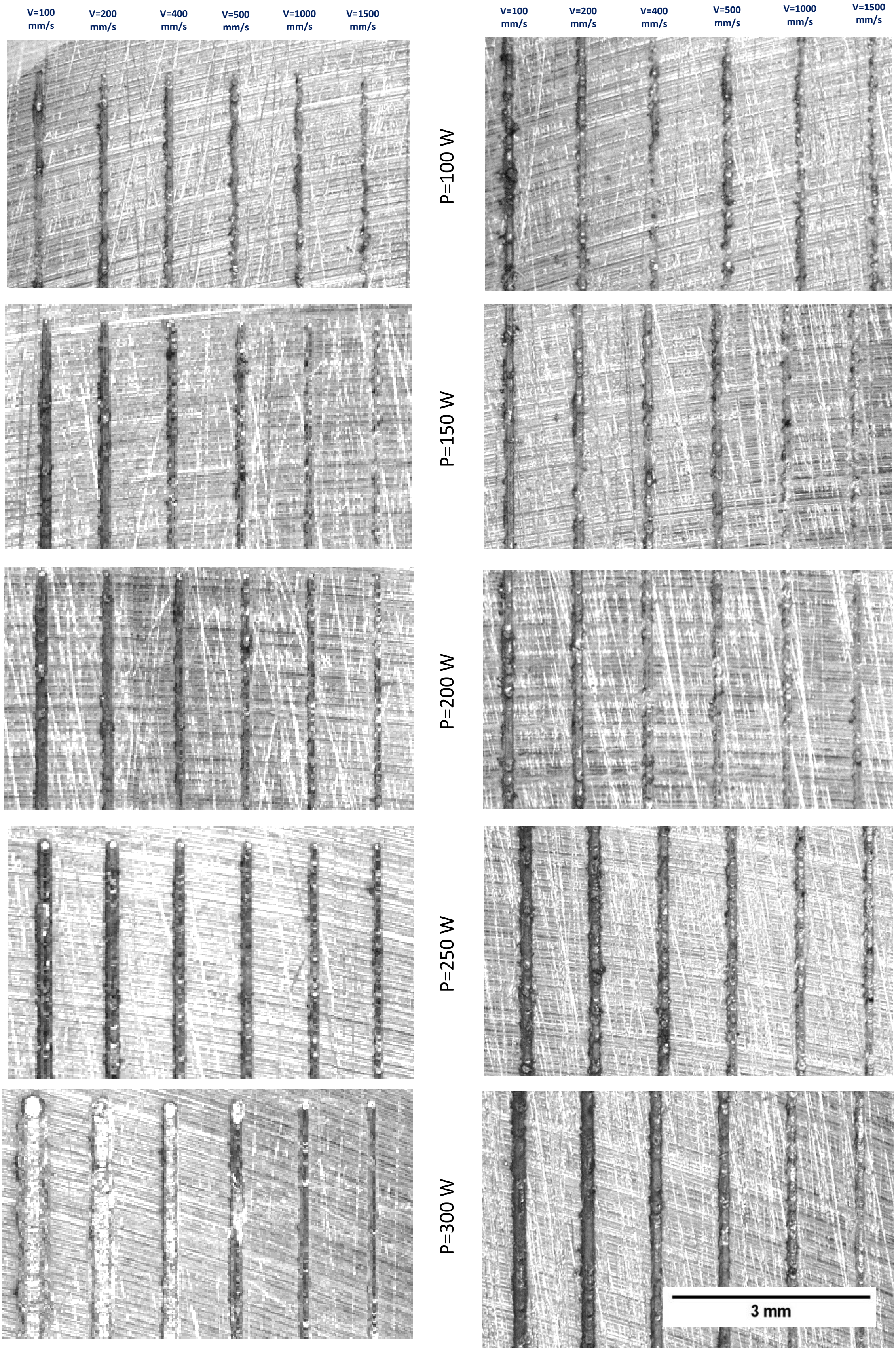
V=100 mm/s
V=200 mm/s
V=400 mm/s
V=500 mm/s
V=1000 mm/s
V=1500 mm/s
P=100 W
P=150 W
P=200 W
P=250 W
P=300 W
3 mm

(a) (b)

Figure 4.4. Design of experiments for single-track scanning of Al-6.3Cu for laser mode: (a) CW; (b) MW.

The visual inspection of each single-track scanning (Figure 4.3 and Figure 4.4) allows to divide the tracks into three categories: (i) uniform; (ii) non-uniform and (iii) discontinuous. Figure 4.5 presents this classification for the single tracks obtained experimentally for the AlSi10Mg alloy. The uniformity (good quality) of the tracks is obtained for small values of scanning speed (≤ 1000 mm/s) and at least intermediate values of laser power. Globally, values of scanning speed larger than 1000 mm/s yields discontinuous tracks (poor quality), even for large values of laser power. This corresponds to low values of energy density. The influence of the laser emission mode (CW or MW) on the deposition quality is also shown in Figure 4.5, comparing the quality of the deposited tracks. It is seen that with the MW a wider processing window is obtained for uniform tracks.

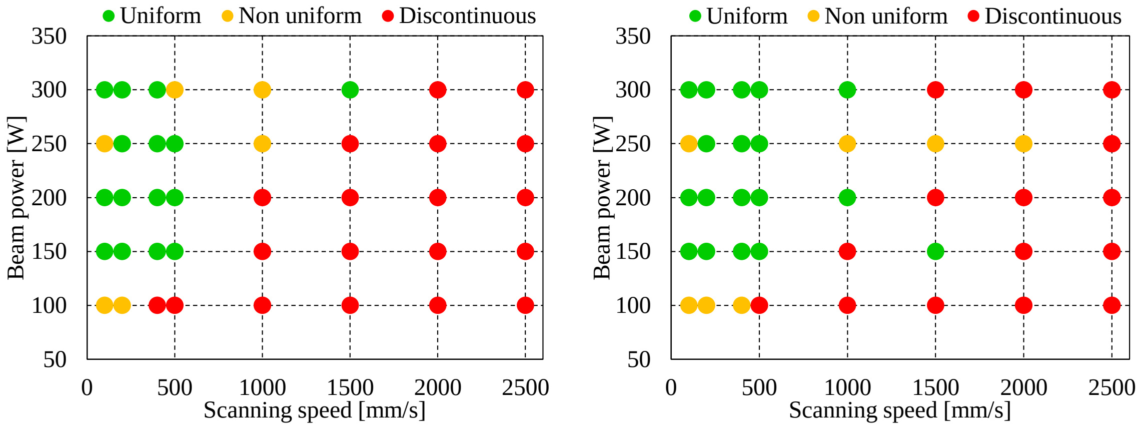

(a) (b)

Figure 4.5. Morphology of the single tracks obtained experimentally for AlSi10Mg using the laser mode: (a) CW; (b) MW.

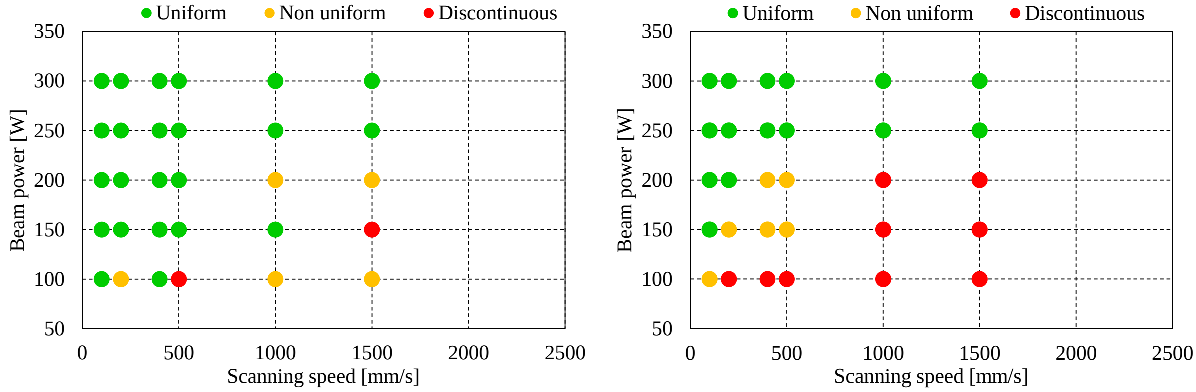

(a) (b)

Figure 4.6. Morphology of the single tracks obtained experimentally for Al-6.3Cu using the laser mode: (a) CW; (b) MW.

The classification for the single tracks obtained experimentally for the Al-6.3Cu alloy is shown in Figure 4.6. The main difference between the AlSi10Mg and Al-6.3Cu appears for higher values of laser power and scanning speed, where a wider processing window is obtained for uniform single tracks in the case of the Al-6.3Cu alloy.

The shape and dimensions of the melt pool were observed in the transverse cross-section of the substrate with the single-tracks. The cross-section view of each single track of AlSi10Mg using the laser emission mode CW and MW is presented in Figure 4.7 and Figure 4.8, respectively. The melt pool height is very high in some cases, particularly for v = 100 mm/s and CW laser mode, but also for large values of scanning speed and laser power in case of MW laser mode.

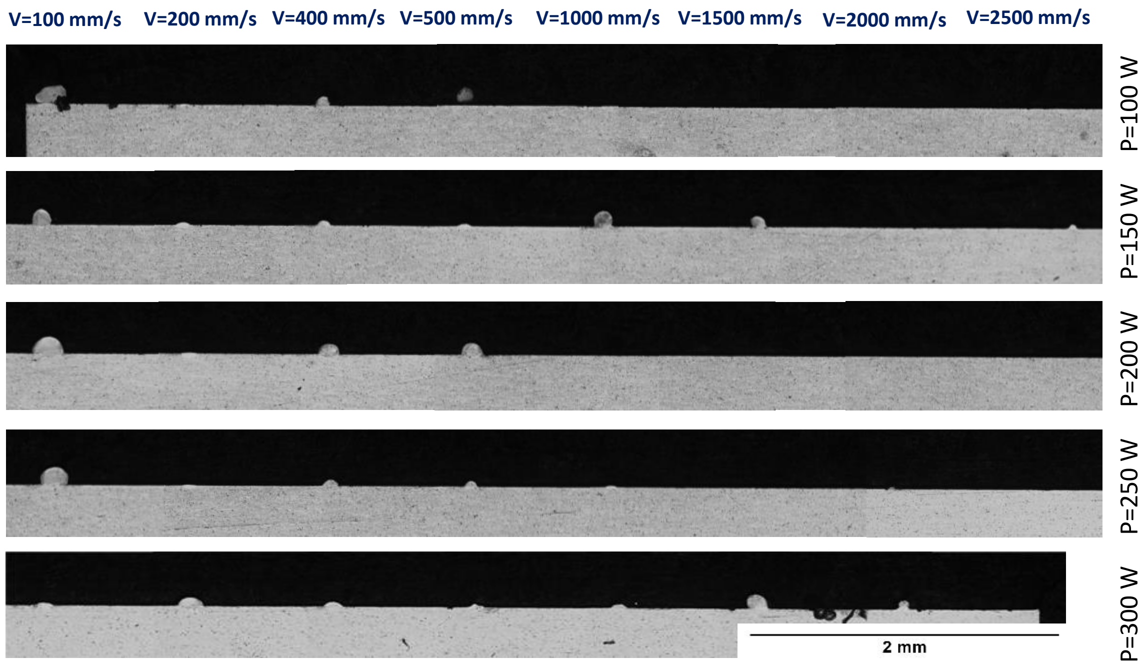
V=100 mm/s
V=200 mm/s
V=400 mm/s
V=500 mm/s
V=1000 mm/s
V=1500 mm/s
V=2000 mm/s
V=2500 mm/s
P=100 W
P=150 W
P=200 W
P=250 W
P=300 W
2 mm

Figure 4.7. Cross section view of each single track of AlSi10Mg for CW laser mode.

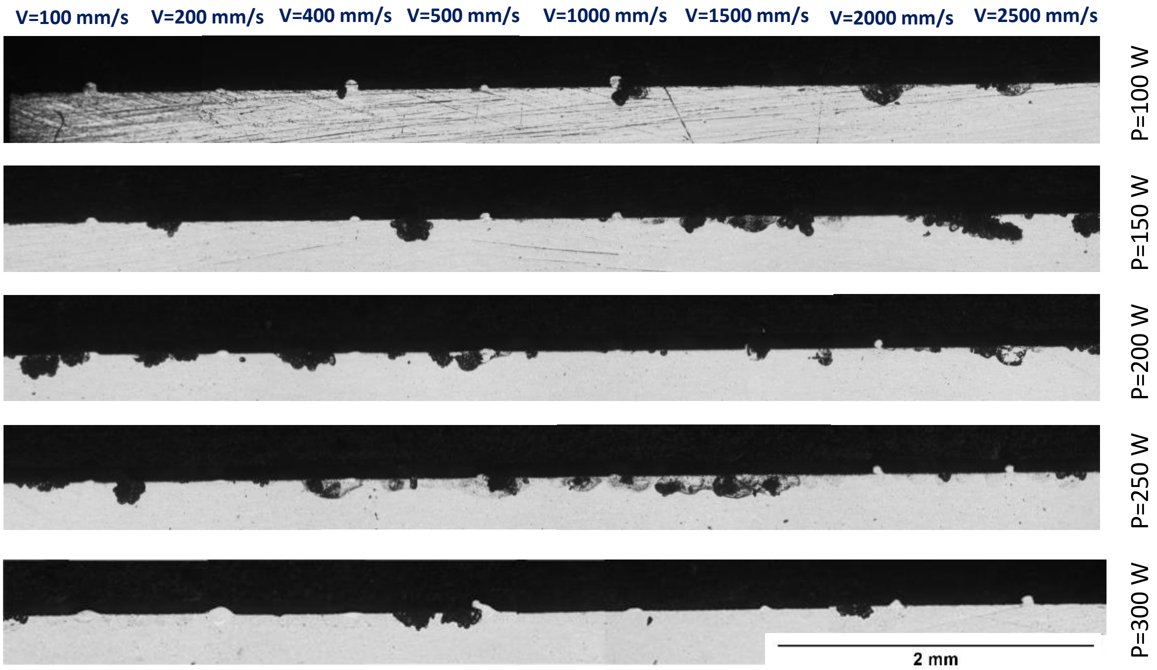
V=100 mm/s
V=200 mm/s
V=400 mm/s
V=500 mm/s
V=1000 mm/s
V=1500 mm/s
V=2000 mm/s
V=2500 mm/s
P=100 W
P=150 W
P=200 W
P=250 W
P=300 W
2 mm

Figure 4.8. Cross section view of each single track of AlSi10Mg for MW laser mode.

The cross-section view of each single track of Al-6.3Cu using the laser emission mode CW and MW is presented in Figure 4.9 and Figure 4.10, respectively. In opposite to the AlSi10Mg powder, the melt pool height is very low in all set of process parameters for Al-6.3Cu. However, the melt pool depth is very large using CW laser mode for P=300 W. Despite the easy identification of each single track in the top view of Figure 4.4, the cross section presents some voids in the location of the tracks, which indicating material remotion from the substrate instead of material addition, probably resulted from the chemical etching.

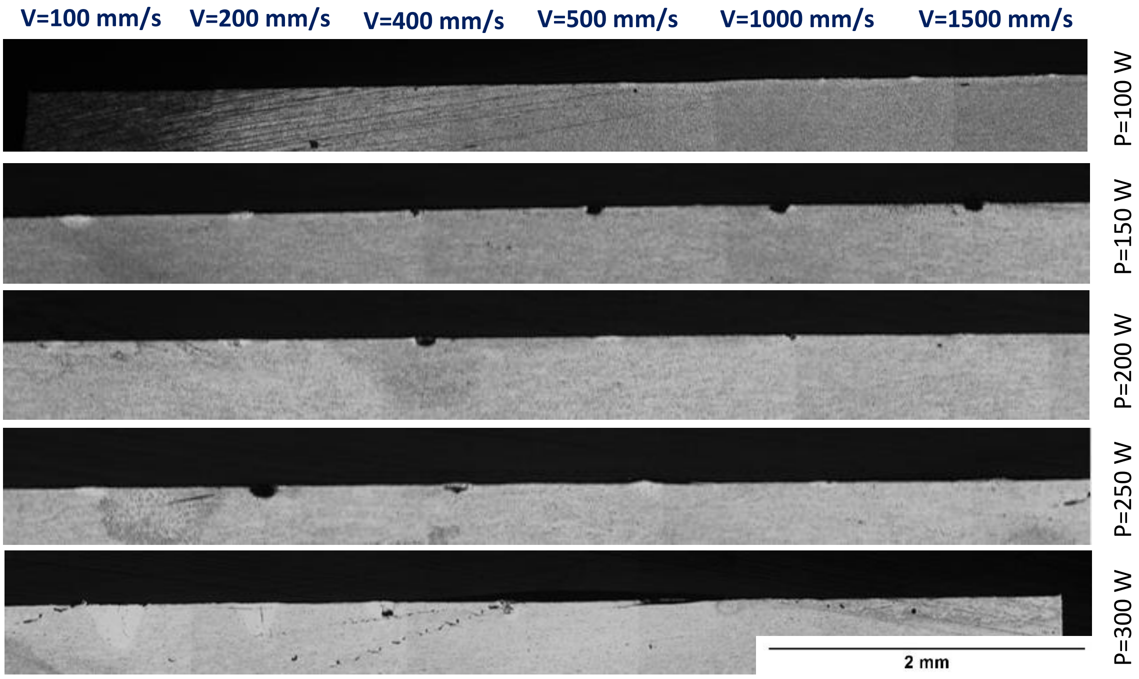
V=100 mm/s
V=200 mm/s
V=400 mm/s
V=500 mm/s
V=1000 mm/s
V=1500 mm/s
P=100 W
P=150 W
P=200 W
P=250 W
P=300 W
2 mm

Figure 4.9. Cross section view of each single track of Al-6.3Cu for CW laser mode.

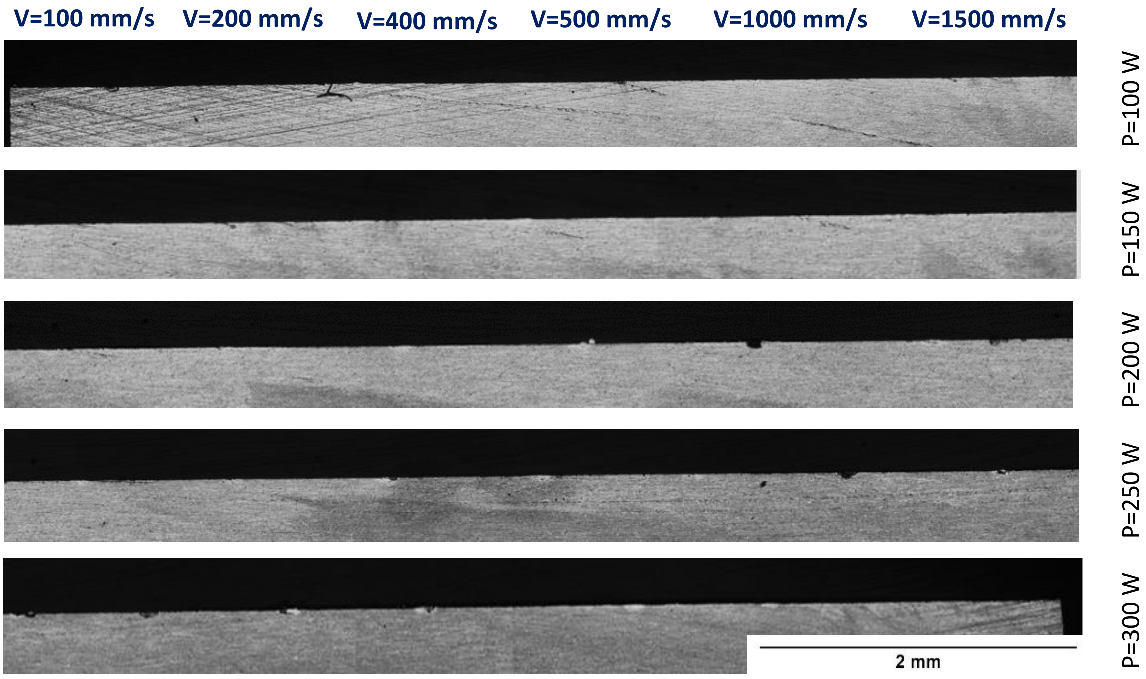
V=100 mm/s
V=200 mm/s
V=400 mm/s
V=500 mm/s
V=1000 mm/s
V=1500 mm/s
P=100 W
P=150 W
P=200 W
P=250 W
P=300 W
2 mm

Figure 4.10. Cross section view of each single track of Al-6.3Cu for MW laser mode.

The predicted melt pool shape is presented in Figure 4.11 for AlSi10Mg, comparing CW and MW laser modes for P=200 W and different scanning speed values. In case of CW laser emission mode, the predicted track is always continuous due to the assumptions adopted in the numerical model, which differs from the experimental observation (Figure

4.5). Besides, the melt pool is larger for small values of scanning speed. For all values of scanning speed presented, there are melting of the substrate, which guarantee the connection of the track to the substrate. Nevertheless, adopting the MW laser emission mode, the track width can be non-uniform for large values of scanning speed (see Figure 4.11 (c)). Besides, the geometry of the melt pool seems more spherical using the MW laser mode.

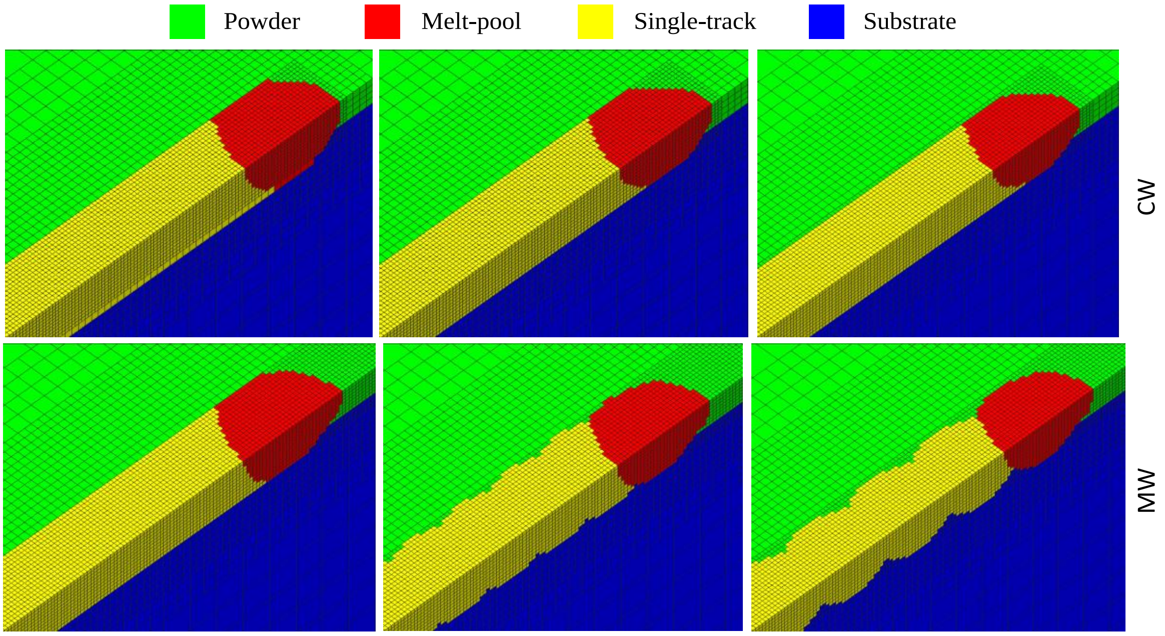

(a) (b) (c)

Figure 4.11. Predicted material phase in single tracks for AlSi10Mg comparing CW and MW laser modes for P=200 W using: (a) v=1000 mm/s; (b) v=1500 mm/s; (c) v=2000 mm/s.

The top view of the interface between powder layer and substrate for AlSi10Mg using the MW laser mode is presented in Figure 4.12 (a), allowing to quantify the connection of each single track with the substrate. Indeed, the single track is discontinuous for P=200 W and v=2000 mm/s due to the large value of point distance (80 μm) for 40 μs of exposure time. Note that this is the cross-section at the interface with the substrate, i.e. 30 μm under the top surface of the powder bed. Considering the entire design of experiments, the influence of both beam power and scanning speed on the track interface morphology is shown Figure 4.12 (b). The uniformity of the track interface is obtained for large values of laser power and small values of scanning speed. On the other hand, discontinuous tracks are obtained particularly for large values of scanning speed and lower values of laser power. This data allows a proper definition of the process parameters to be used in L-PBF process to avoid either non-uniform or discontinuous tracks. These numerical predictions are in agreement with the measurements (Figure 4.5 (b)), i.e. the uniform track is obtained for scanning speed values up to 1000 mm/s when P = 300 W and for scanning speed values up to 500 mm/s when P = 150-250 W.

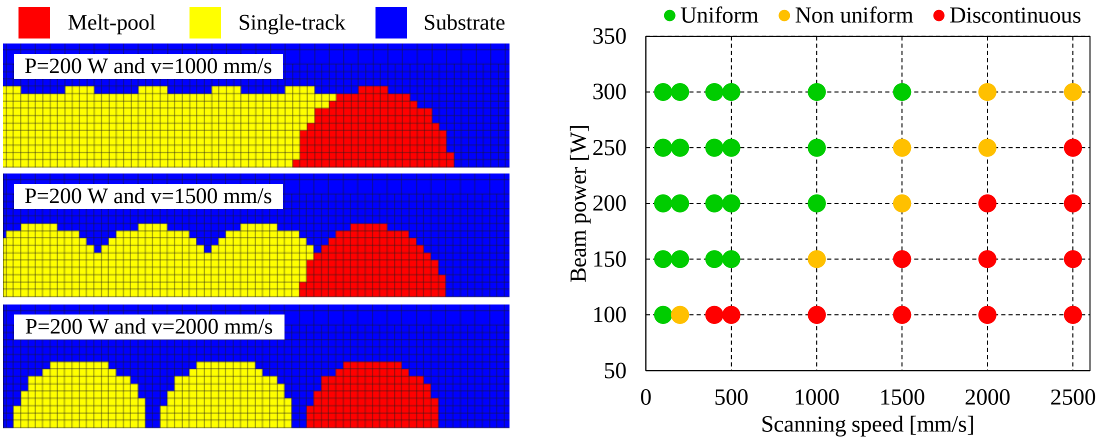

(a) (b)

Figure 4.12. Predicted single tracks for AlSi10Mg using the MW laser mode: (a) top view of the interface between powder layer and substrate; (b) influence of the beam power and scanning speed on the track interface morphology.

4.2.2. Melt pool dimensions

The melt pool dimensions (width, height and depth) of each single track were evaluated from the optical micrographs. Figure 4.13 (a) shows the cross-section of the track of AlSi10Mg obtained with CW laser mode using P=150 W and v=200 mm/s, while Figure 4.13 (b) presents the track produced with P=200 W and 100 mm/s. The reduction of the scanning speed to the minimum value (100 mm/s) and slight increase of the laser power leads to a significant increase of the melt pool height, as shown in Figure 4.13 (b). Nevertheless, the melt pool depth is approximately the same for both set of process parameters.

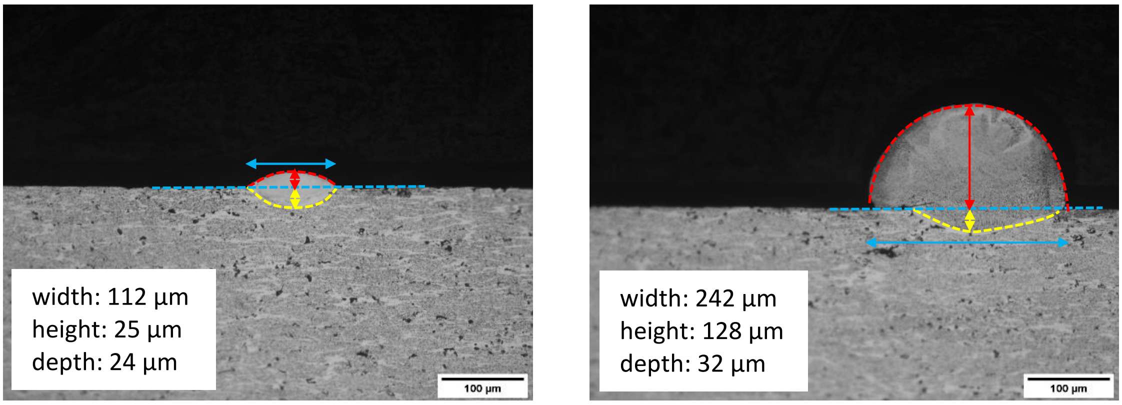
width: 112 µm
height: 25 µm
depth: 24 µm
100 µm
width: 242 µm
height: 128 µm
depth: 32 µm
100 µm

(a) (b)

Figure 4.13. Shape of the track cross-section for AlSi10Mg using the CW laser mode: (a) P=150 W and v=200 mm/s; (b) P=200 W and 100 mm/s.

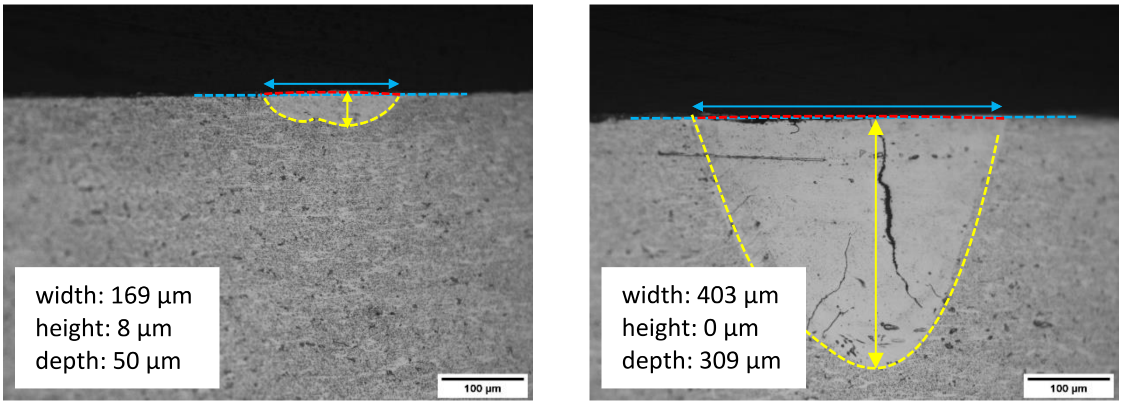
width: 169 µm
height: 8 µm
depth: 50 µm
100 µm
width: 403 µm
height: 0 µm
depth: 309 µm
100 µm

(a) (b)

Figure 4.14. Shape of the track cross-section for Al-6.3Cu using the CW laser mode: (a) P=200 W and v=500 mm/s; (b) P=300 W and 200 mm/s.

Regarding the Al-6.3Cu alloys, the track cross-section is presented in Figure 4.14 for two different set of process parameters and using CW laser mode. The increase of the laser power from 200 W to 300 W and the slight decrease of the scanning speed from 500 mm/s to 200 mm/s leads to substantial increase of the melt pool depth. Besides, the melt pool height is very small or inexistent for Al-6.3Cu powder mixture. Therefore, the very clear identification of each track in the top view (Figure 4.4) for Al-6.3Cu can be just a modification of the substrate surface without significative material deposition. The vertical crack within the zone of the melt pool (Figure 4.14 (b)) results from the thermal material contraction occurring during the cooling, leading to significative residual tensile stresses due to the constraints imposed by the large stiffness of the substrate.

The influence of the laser power and scanning speed on the measured melt pool width, height and depth for the AlSi10Mg alloy is presented in Figure 4.15, Figure 4.16 and Figure 4.17, respectively. The measurements were carried out only for the tracks assumed uniform according to Figure 4.5. Globally, the melt pool width increases with the increase of the laser power, particularly for MW laser mode. The maximum values obtained for the melt pool width are around 230 µm (see Figure 4.15). The effect of the process parameters on the melt pool height is clearer for MW laser mode (Figure 4.16 (b)), where the increase of the laser power together with the decrease of the scanning speed leads to an increase of the melt pool height. For some combinations of process parameters, the melt pool height is larger than the powder layer thickness, which was 30 µm. On the other hand, the expected effect of the process parameters on the melt pool depth is stronger for CW laser mode (see Figure 4.17 (a)). The melt pool depth can achieve 50 µm for the largest value of laser power, as shown in Figure 4.17 (a).

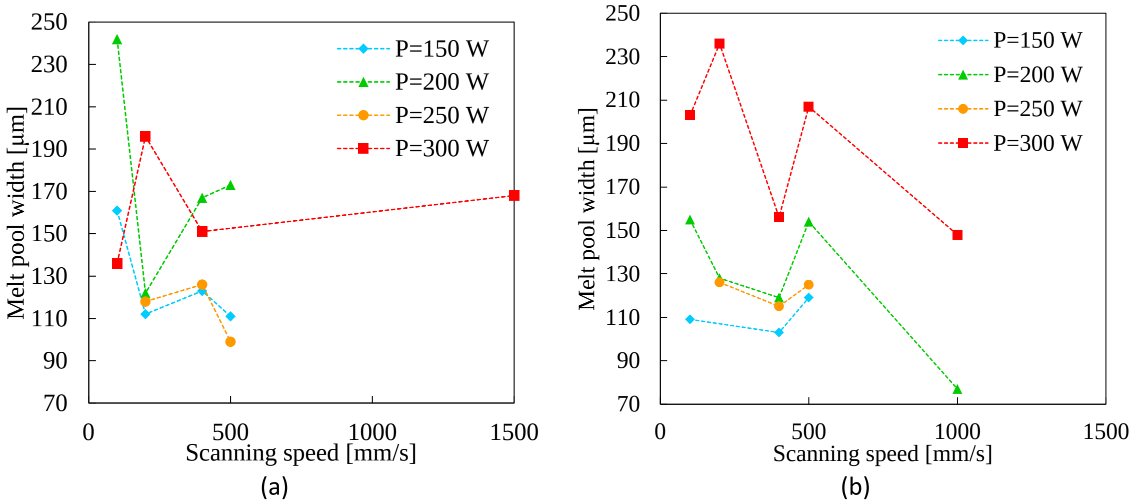

(a) (b)

Figure 4.15. Effect of laser power and scanning speed on the measured melt pool width for AlSi10Mg using the laser mode: (a) CW; (b) MW.

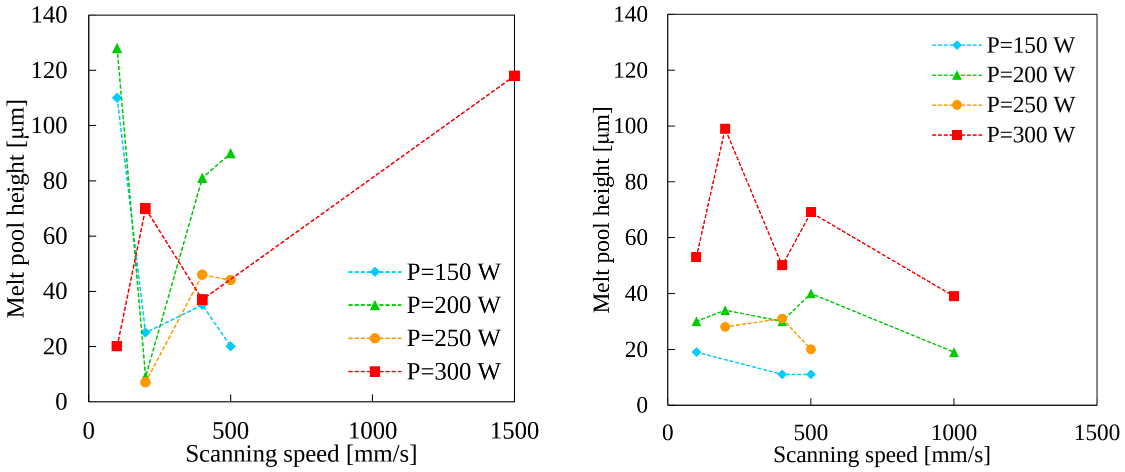

(a) (b)

Figure 4.16. Effect of laser power and scanning speed on the measured melt pool height for AlSi10Mg using the laser mode: (a) CW; (b) MW.

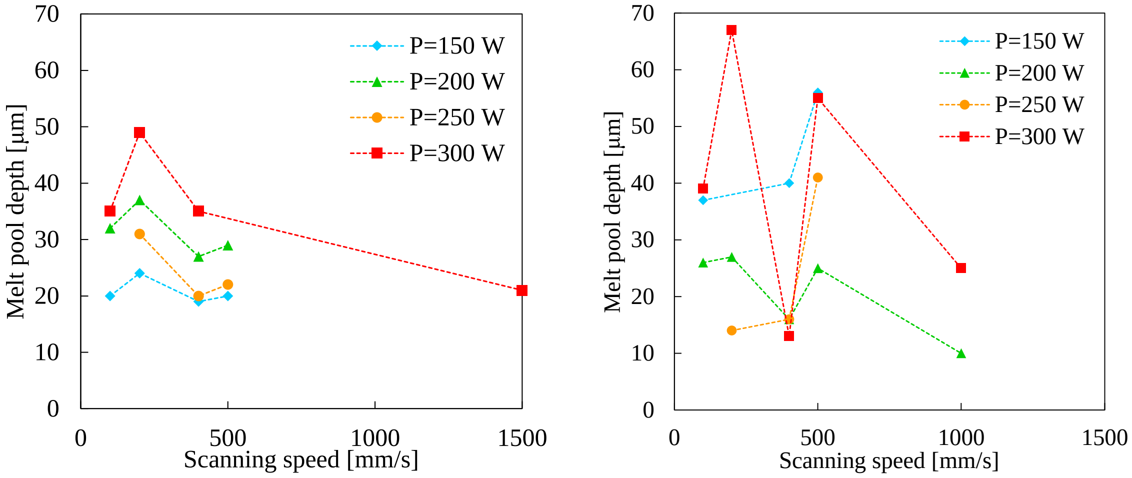

(a) (b)

Figure 4.17. Effect of laser power and scanning speed on the measured melt pool depth for AlSi10Mg using the laser mode: (a) CW; (b) MW.

The numerical prediction of the melt pool width, depth and length for AlSi10Mg is presented in Figure 4.18, Figure 4.19 and Figure 4.20, respectively. Generally, the predicted melt pool size (width, depth and length) is lower using the MW laser mode because during 25% of the time the laser is switched off (see Figure 3.2 (b)) and therefore less energy is introduced into the melt pool. The sharp variation of the melt pool size with the scanning speed is related with the mesh size used in the numerical simulations, which is unable to define accurately the melt pool size/dimension, particularly the width and depth. Nevertheless, the melt pool size increases with the increase of the laser power and with reduction of the scanning speed. The predicted melt pool width ranges between 90 μm and

240 µm (Figure 4.18). Regarding the melt pool depth, the maximum value predicted was 65 µm. However, for the small laser power (P=100 W) the energy was not enough for melting the substrate (null depth), particularly for MW laser mode (Figure 4.19 (b)). Comparing the melt pool width (Figure 4.18) with the melt pool length (Figure 4.20), the predicted melt pool shape is approximately circular (top view). The increase of the predicted melt pool length for P=100 W and scanning speed values larger than 1000 mm/s using the CW laser mode (Figure 4.20 (a)) is a consequence of the lack of connection between the scanned track and the substrate (Figure 4.19 (a)).

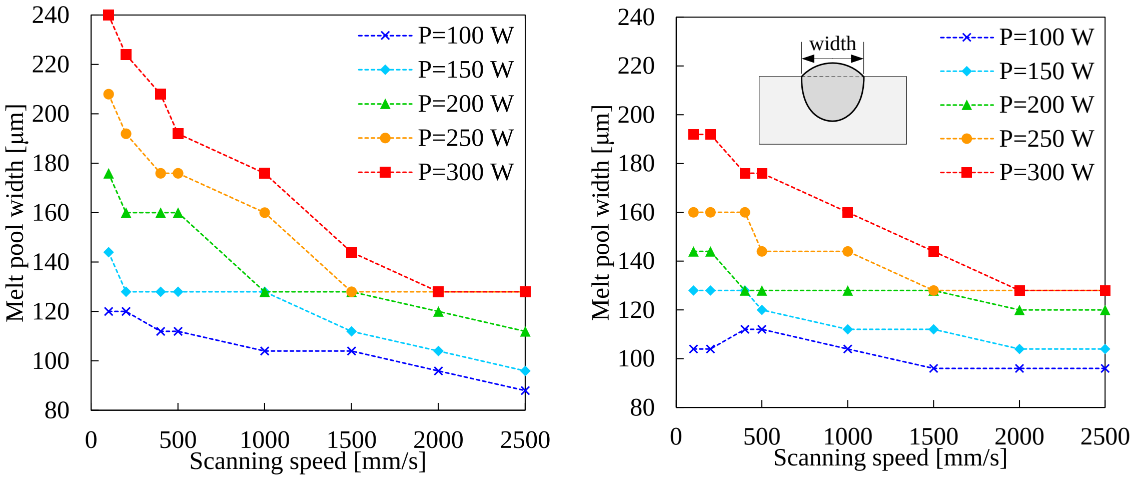

(a)

(b)

Figure 4.18. Effect of laser power and scanning speed on the predicted melt pool width for AlSi10Mg using the laser mode: (a) CW; (b) MW.

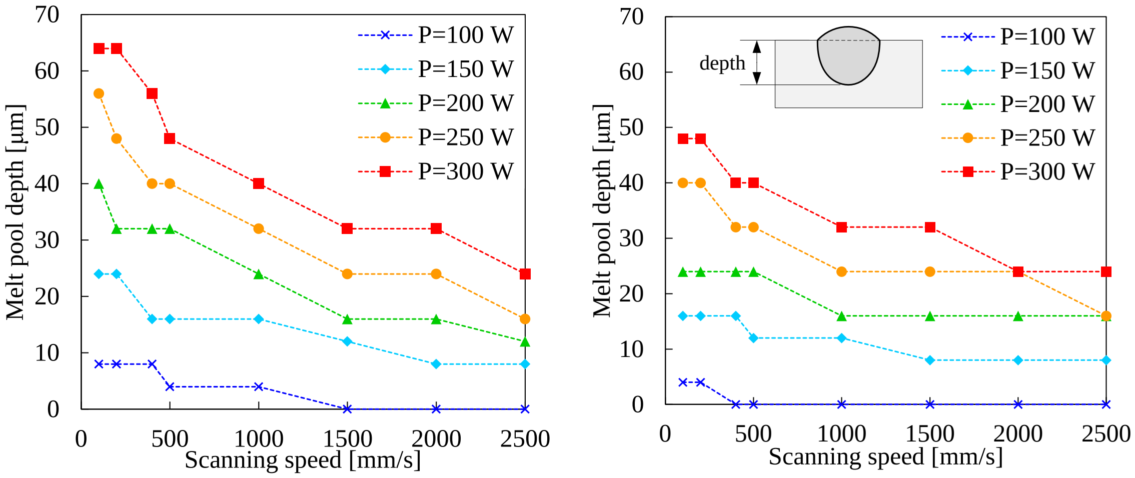

(a)

(b)

Figure 4.19. Effect of laser power and scanning speed on the predicted melt pool depth for AlSi10Mg using the laser mode: (a) CW; (b) MW.

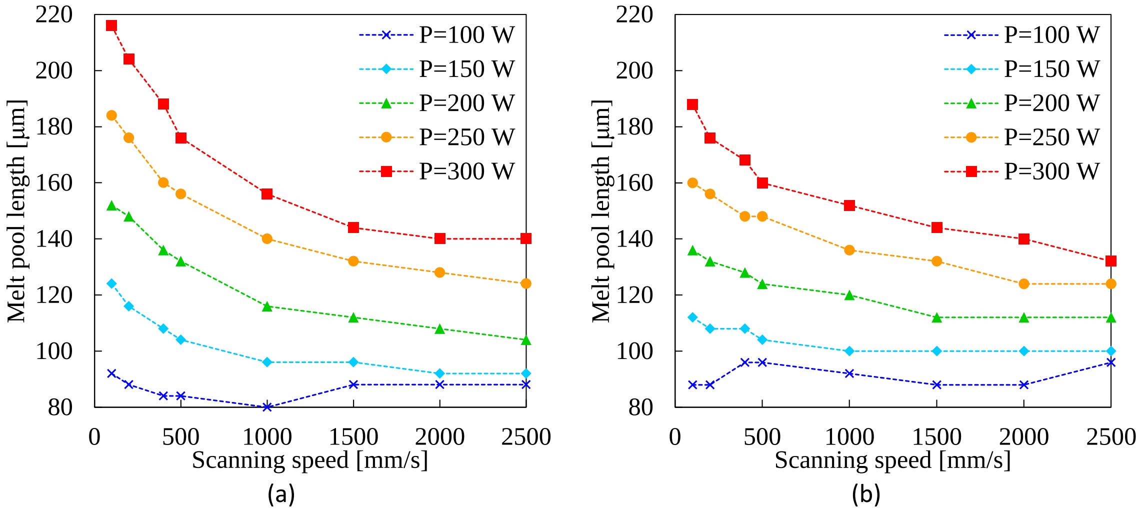

Figure 4.20. Effect of laser power and scanning speed on the predicted melt pool length for AlSi10Mg using the laser mode: (a) CW; (b) MW.

The influence of the laser power and scanning speed on the measured melt pool width, height and depth for the Al-6.3Cu alloy is presented in Figure 4.21, Figure 4.22 and Figure 4.23, respectively, considering only the uniform tracks according to Figure 4.6.

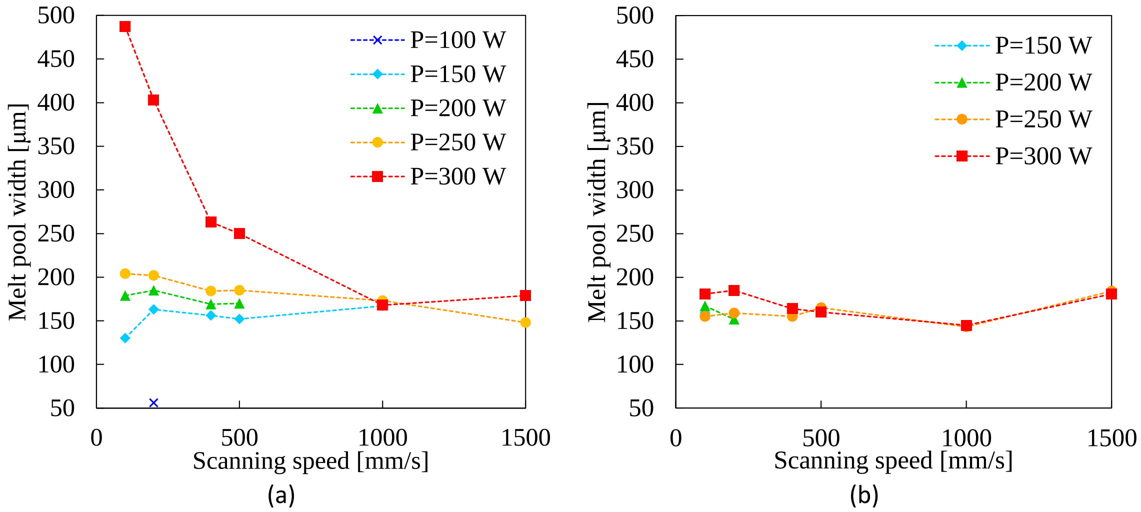

Figure 4.21. Effect of laser power and scanning speed on the measured melt pool width for Al-6.3Cu using the laser mode: (a) CW; (b) MW.

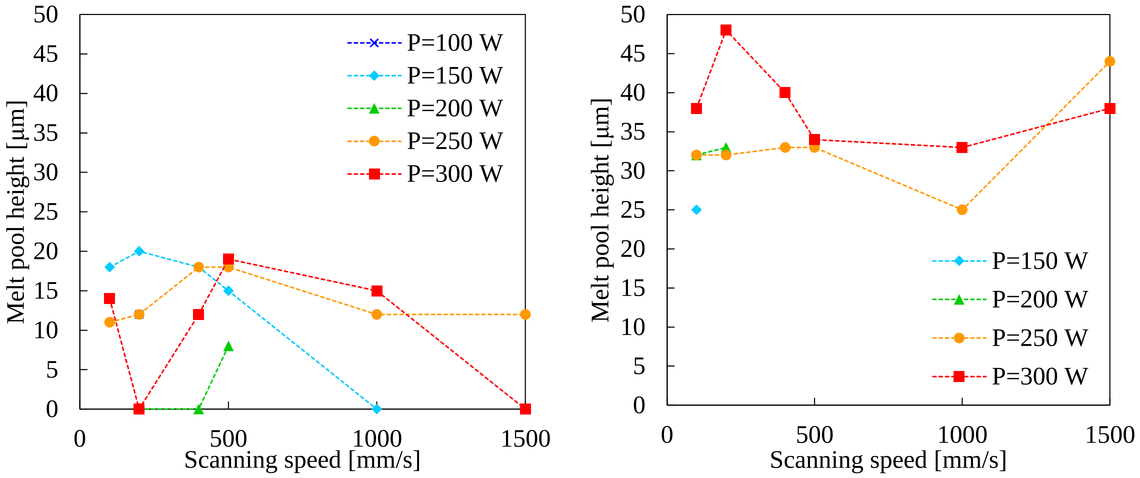

(a) (b)

Figure 4.22. Effect of laser power and scanning speed on the measured melt pool height for Al-6.3Cu using the laser mode: (a) CW; (b) MW.

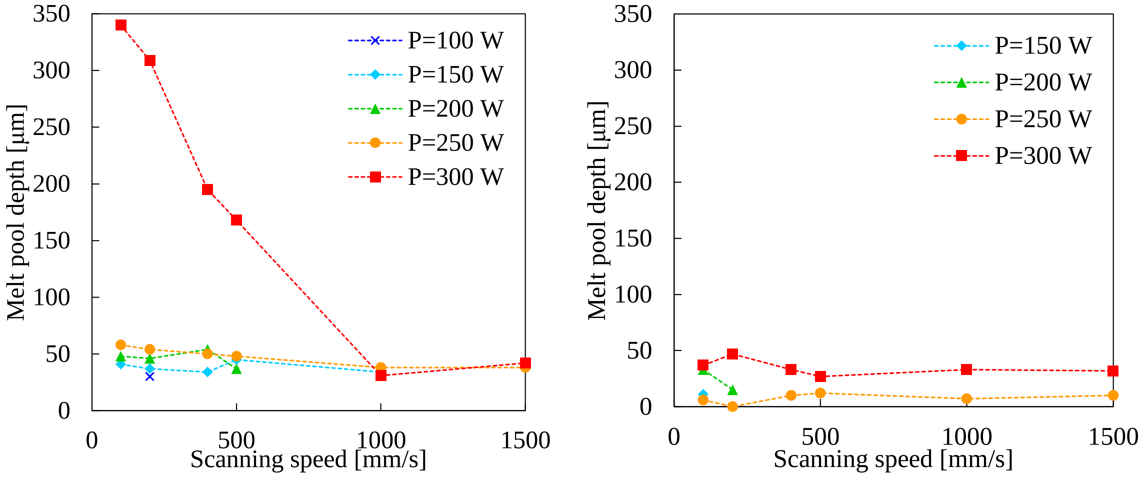

(a) (b)

Figure 4.23. Effect of laser power and scanning speed on the measured melt pool depth for Al-6.3Cu using the laser mode: (a) CW; (b) MW.

Globally, the melt pool width is ranging between 150 µm and 200 µm, except for the CW laser mode and P=300 W, where the measured melt pool width achieves up to 500 µm, as shown in Figure 4.21 (a). The melt pool height is significantly larger adopting the MW laser mode in comparison with the CW laser mode. In fact, using the CW laser mode the melt pool height is at most 20 µm, as shown in Figure 4.22 (a). This value is significatively lower than the measurements carried for AlSi10Mg under identical process parameters (Figure 4.16 (b)). Adopting the MW laser mode, the measured melt pool height is slightly larger than the powder layer thickness (30 µm). The measured melt pool depth is very high for P=300 W and using the CW laser mode (see Figure 4.23 (a)). Except for this set of parameters, the melt pool depth is about 50 μm when the CW laser mode is adopted. Thus, globally the melt pool depth obtained for Al-6.3Cu powder mixture is larger than the one obtained for AlSi10Mg.

4.3. Hollow thin-wall cubes

Figure 4.24 presents the top view of each hollow thin-wall cube built using AlSi10Mg and the CW laser mode.

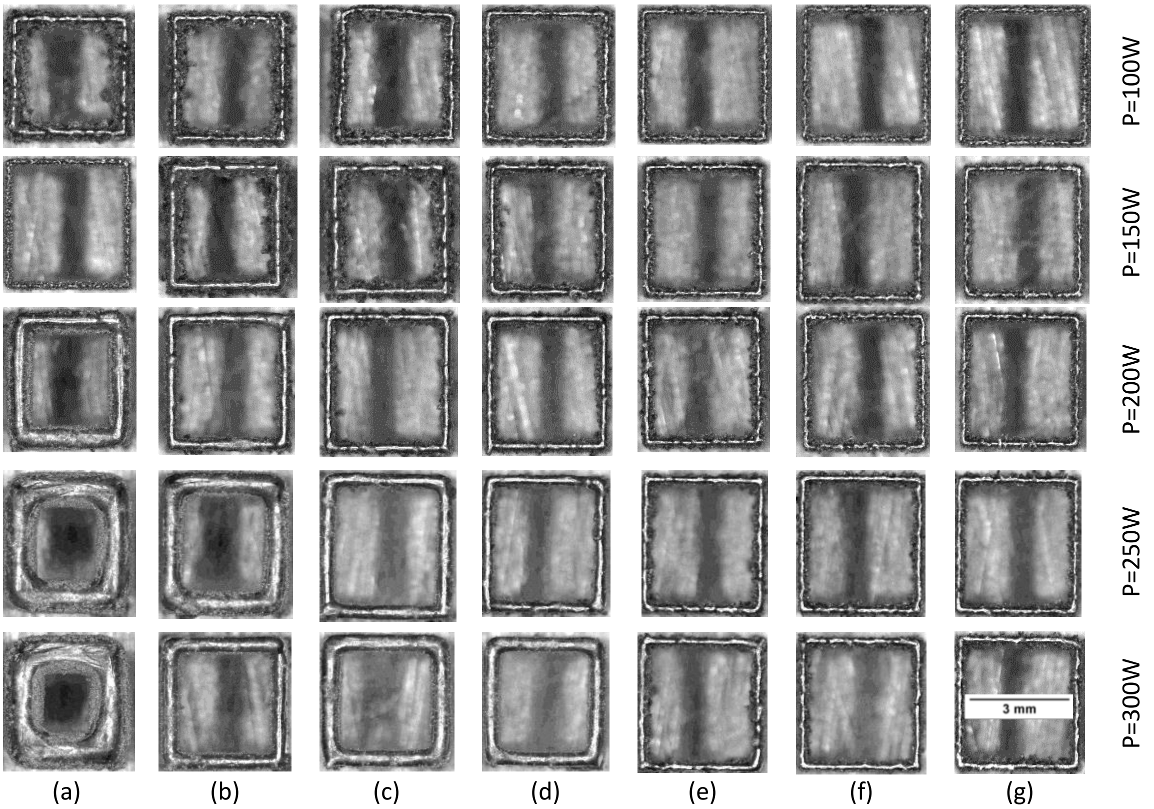

Figure 4.24. Design of experiments for the hollow thin-wall cube using AlSi10Mg and CW laser mode for scanning speed: (a) 100 mm/s; (b) 200 mm/s; (c) 400 mm/s; (d) 500 mm/s; (e) 1000 mm/s; (f) 1500 mm/s; (g) 2000 mm/s.

The design of experiments covers different values of laser power and scanning speed. Globally, the wall thickness increases either increasing the laser power or decreasing the scanning speed. Therefore, the thick wall was obtained for P=300 W and v=100 mm/s, as may be seen in Figure 4.24. On the other hand, for small values of laser power and large values of scanning speed, the wall can be discontinuous, i.e. some voids are visible in the walls. These results are in agreement with the observations carried out for the single tracks deposited on the substrate (Figure 4.3). The top view of each hollow thin-wall cube built using AlSi10Mg for P=100 W and the MW laser mode is shown in Figure 4.25. Since the values selected for the laser power are very low, the obtained thin-wall is discontinuous for all values of scanning speed adopted in the design of experiments. Despite the discontinuity of the built walls, the increase of the scanning speed leads to a global decrease of the thickness (see Figure 4.25).

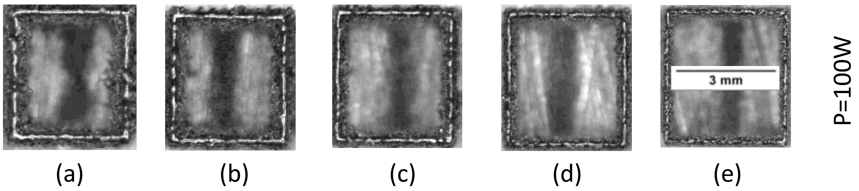

Figure 4.25. Design of experiments for the hollow thin-wall cube using AlSi10Mg and MW laser mode for scanning speed: (a) 100 mm/s; (b) 200 mm/s; (c) 400 mm/s; (d) 500 mm/s; (e) 1000 mm/s.

The influence of both the laser power and the scanning speed on the measured wall thickness of the built hollow cube for AlSi10Mg is presented in Figure 4.26 for both CW and MW laser emission modes. In order to take into account the variability in the experimental measurements from microscopic pictures, the thickness was evaluated in each edge of the cross-section of the hollow cube. Besides, in case of discontinuous walls, the evaluation was performed in the continuous portions of the edge. The maximum average thickness obtained was 0.77 mm. Nevertheless, using the same values of process parameters (P=300W, v=100mm/s, CW) and powder material, the melt pool width measured in the single track was lower than 0.15 mm (Figure 4.15). Therefore, the thickness of the wall is significatively larger than the melt pool width obtained in the single track under identical conditions. This is a consequence of the heat flux, which is directly affected by the geometry of heat conduction. Although the substantial variability in the measurements (error bars), the global increase of the wall thickness with the increase of the laser power and reduction of the scanning speed is visible. Besides, the difference between CW and MW is not noticeable.

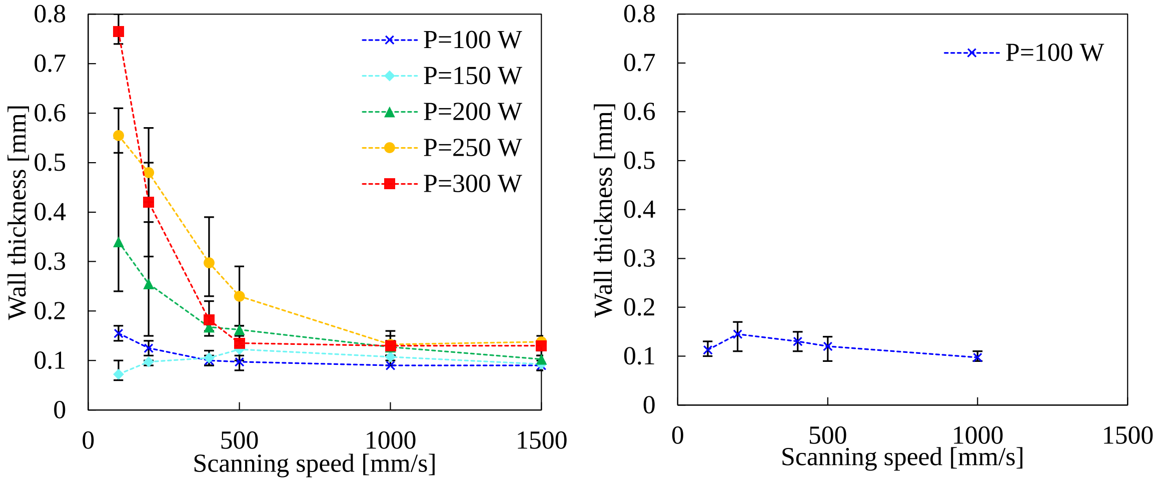

(a) (b)

Figure 4.26. Effect of laser power and scanning speed on the measured wall thickness of each hollow cube for AlSi10Mg using the laser mode: (a) CW; (b) MW.

Figure 4.27 presents the predicted material phase at the end of the 40th layer deposition in the hollow thin-wall cube for P=300 W and v=200 mm/s using the CW laser mode, highlighting the influence of the initial wall thickness (0.2 mm or 0.4 mm) used in the numerical model. The lower value for the initial wall thickness (0.2 mm) was selected from the predicted melt pool width in the single track (Figure 4.18) for the same process parameters. The width of the track corresponding to this deposited layer is approximately constant along the entire laser path, but it is larger when the initial wall thickness is lower (0.2 mm). In fact, for 0.2 mm of initial wall thickness the predicted track width was 0.4 mm, while using 0.4 mm of initial wall thickness the predicted track width was 0.3 mm. Note that the remelted wall is not visible in Figure 4.27 because it is under the deposited material.

The temperature field (below the melting point) predicted immediately after the 40th layer deposition (before cooling stage) in the hollow thin-wall cube is presented in Figure 4.28 for P=300 W and v=200 mm/s using the CW laser mode. The hot region of the hollow thin-wall cube is larger when the initial wall thickness is lower. In fact, the temperature of half of the deposited layer is higher than 345 K for t_0=0.2 mm, while this region is reduced to about 1/3 for t_0=0.4 mm. Since the thermal conductivity of the powder bed was assumed 10x lower in comparison with the solid material [62], the heat flux occurs mainly in the walls (solid material). Thus, the heat transfer from the volumetric heat source to the surrounding is stronger when the wall is thicker, leading to a faster heat dissipation (Figure 4.28 (b)).

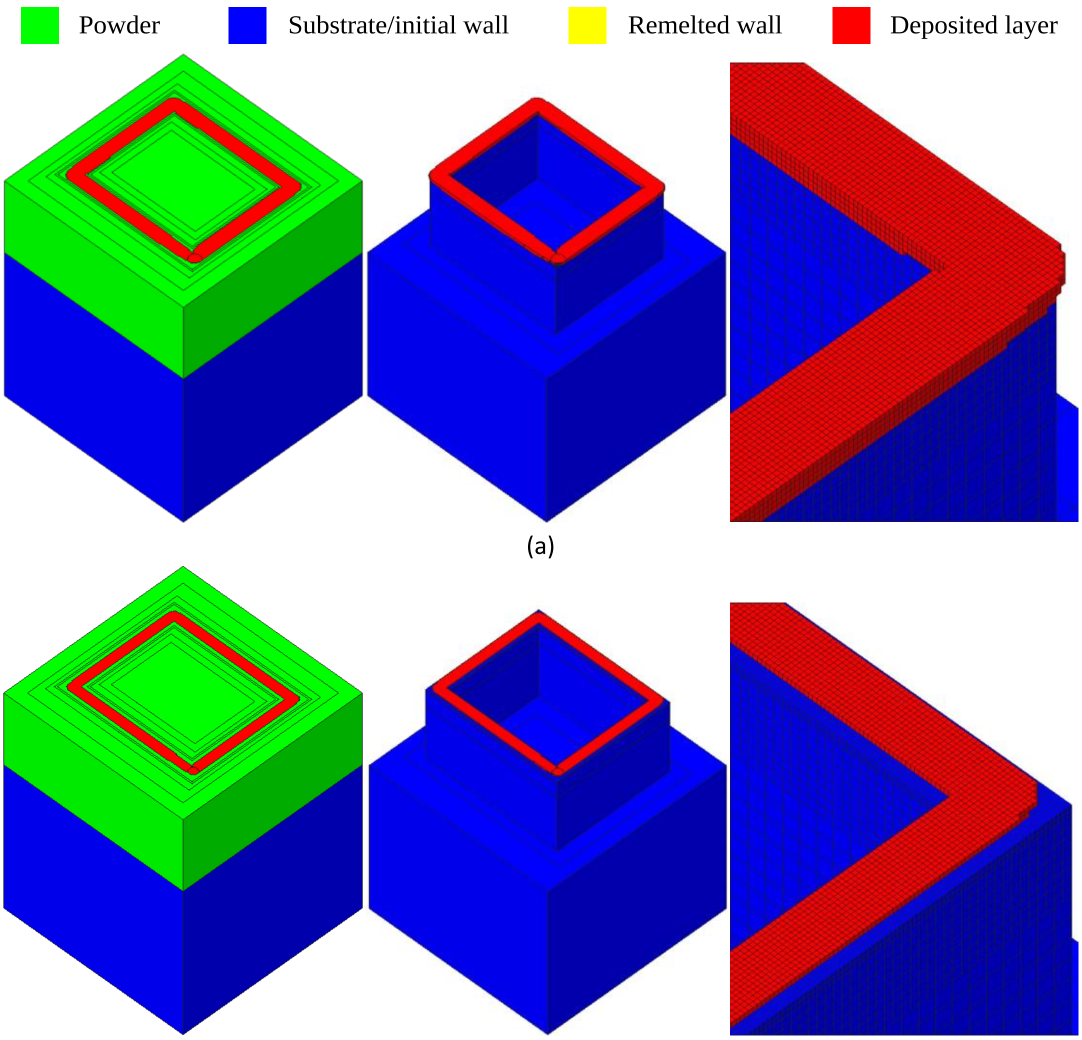
Powder
Substrate/initial wall
Remelted wall
Deposited layer

(a)

(b)

Figure 4.27. Predicted material phase at the end of the 40th layer deposition in the hollow thin-wall cube for P=300 W and v=200 mm/s using the CW laser mode for AlSi10Mg: (a) 0.2 mm of initial wall thickness; (b) 0.4 mm of initial wall thickness.

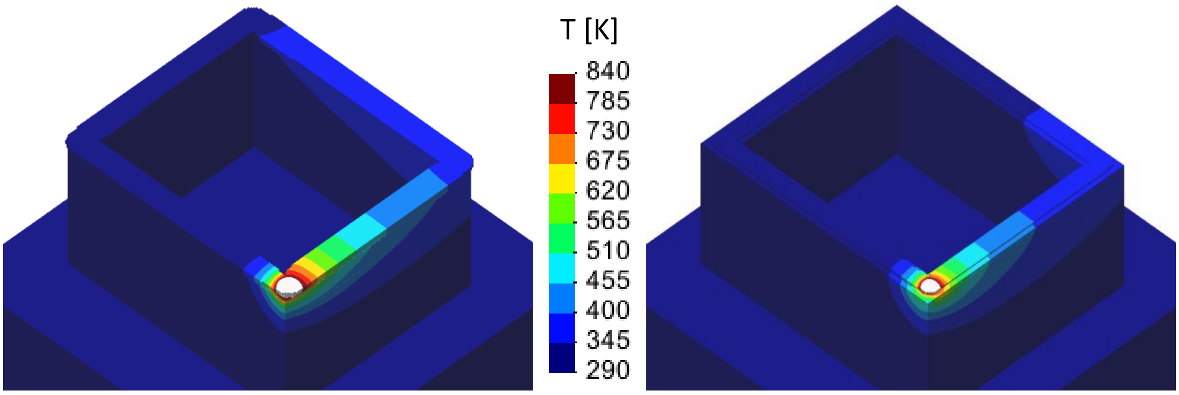
T [K]
840
785
730
675
620
565
510
455
400
345
290

(a)

(b)

Figure 4.28. Predicted temperature field immediately after the 40th layer deposition (before cooling) in the hollow thin-wall cube for P=300 W and v=200 mm/s using the CW laser mode for AlSi10Mg: (a) 0.2 mm of initial wall thickness; (b) 0.4 mm of initial wall thickness.

The predicted material phase in the cross-section at the middle of a laser scan of the hollow thin-wall cube for P=300 W and v=200 mm/s is shown in Figure 4.29, comparing the influence of the initial wall thickness used in the simulation. The cross-section area of the melt pool is smaller (including the remelted zone) when the initial wall thickness is thicker since the heat flux in the vertical direction is easier (more solid material). Although the heat source is always located in the top surface of the powder bed (higher temperature), the heat is dissipated through the initial wall. However, thinner walls hinder the heat transfer since the thermal conductivity of the powder bed is significantly lower. This highlights the importance of multi-layer deposition modelling for accurate prediction of the wall thickness.

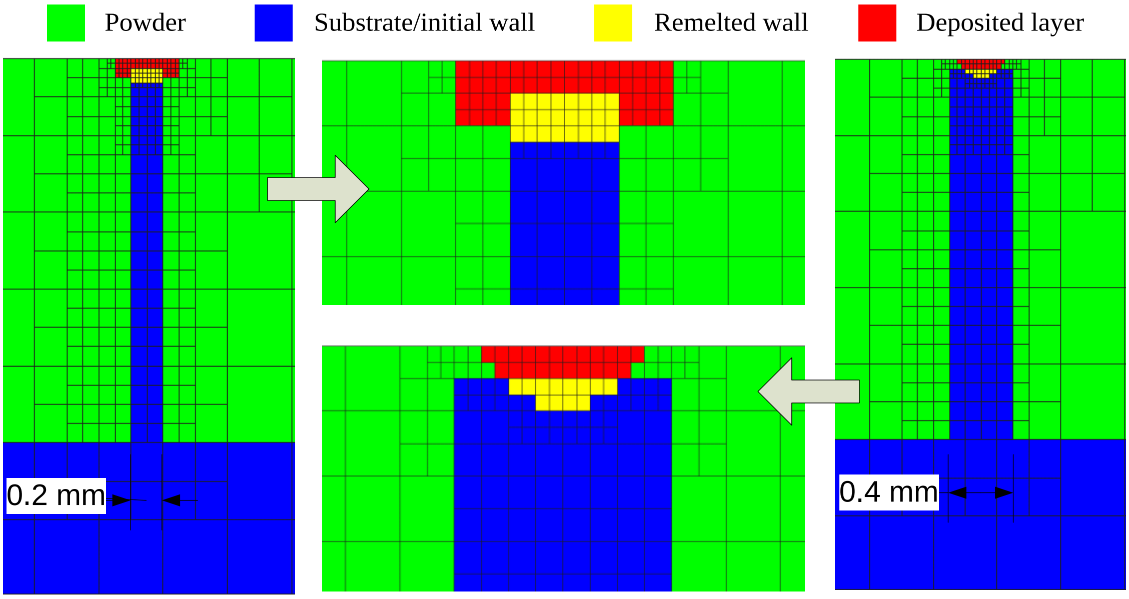

Figure 4.29. Predicted material phase in the cross-section (middle of edge) at the 40th layer deposition in the hollow thin-wall cube for P=300 W and v=200 mm/s and using the CW laser mode for AlSi10Mg.

4.4. Cantilevers

The effect the process parameters selected to build the cantilevers of AlSi10Mg alloy was evaluated. Accordingly, eight different combinations of process parameters were selected according to Table 2.2. Besides, cantilever #7 was built in duplicate to evaluate the effect of the heat treatment on the residual stresses and sample deflection.

4.4.1. Residual stresses and sample deflection

Figure 4.30 presents the lateral view of the cantilever geometry before and after the partially cutting operation. The wire electrical discharge machining (EDM) was carried in two different horizontal planes, i.e. cutting at the lower face of the thin vertical supports (see Figure 4.30 (a)) or cutting at the upper face of the thin vertical supports (see Figure 4.30 (b)). Only cantilevers #4 and #5 were cut at the upper face of supports.

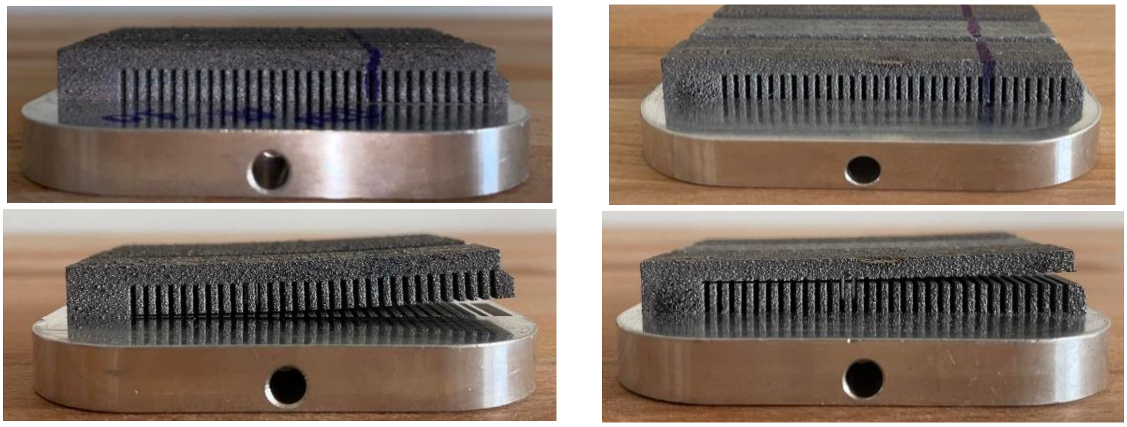
(a) (b)

Figure 4.30. Location of the cutting plane used in the cantilevers: (a) lower face of the support structure; (b) upper face of the support structure.

Figure 4.31 presents the measured cantilever deflection profile before and after the cutting operation using the contact profilometer. The upper surface of each cantilever is approximately horizontal before the cutting operation. Nevertheless, the surface roughness of all sampled is very high, as highlighted in Figure 4.31, which is a characteristic of the L-PBF process. After the cutting operation, the cantilever bends upwards and the maximum vertical deflection occurs in the right side of the cantilever. Considering the cutting at the lower face of the thin vertical supports (Figure 4.30 (a)), the effect of process parameters on the cantilever profile after cut is presented in Figure 4.31 (a)-(c). On the other hand, when the cut is performed at the upper face of the thin vertical supports (Figure 4.30 (b)), the effect of process parameters on the cantilever profile after cut is presented in Figure 4.31 (d). Globally, the cantilever deflection is larger when the cut plane is located at the interface between the sample and the substrate. Besides, the cantilever profile after cut is only slightly influenced by the process parameters studied (laser power, scanning speed, hatch distance, layer thickness and laser emission mode). The maximum vertical deflection measured in the cantilevers ranges between 2.2 mm and 2.5 mm when the cut plane is located at the interface between the sample and the substrate.

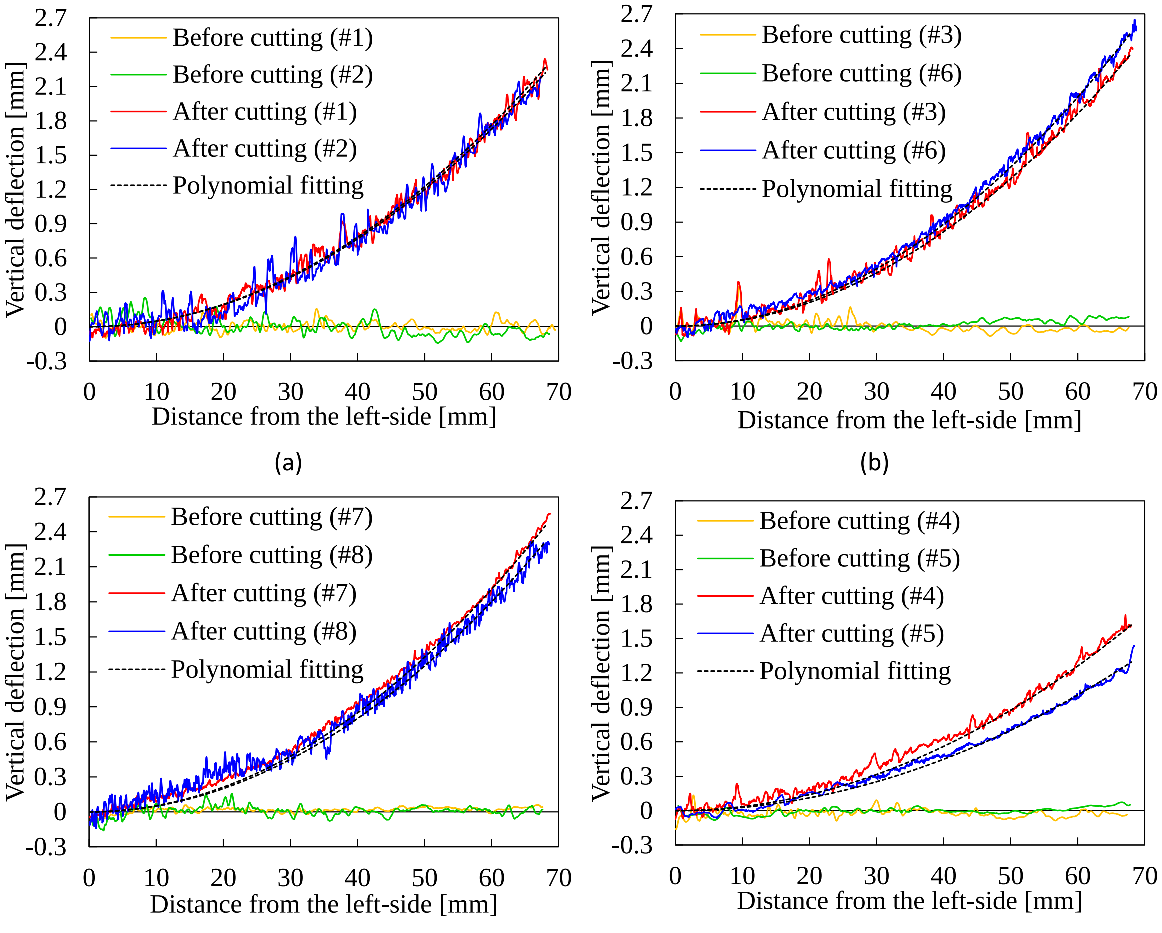

(a) (b)

(c) (d)

Figure 4.31. Effect of process parameters on the measured cantilever deflection profile before and after cutting: (a) cantilevers #1 and #2; (b) cantilevers #3 and #6; (c) cantilevers #7 and #8; (d) cantilevers #4 and #5 with cutting operation performed at the upper face of the thin vertical supports.

Using the finite element simulation at macro-scale, the predicted σ_{xx} stress component field before and after cutting is presented in Figure 4.32. The influence of the process parameters (laser power, scanning speed, and hatch distance and layer thickness) was neglected in the numerical model since the default values of the inherent strain method (see Table 3.2) were adopted in all simulations. In order to assess the influence of the mesh size on the numerical results, two different meshes are adopted (Figure 3.6) in the numerical simulation.

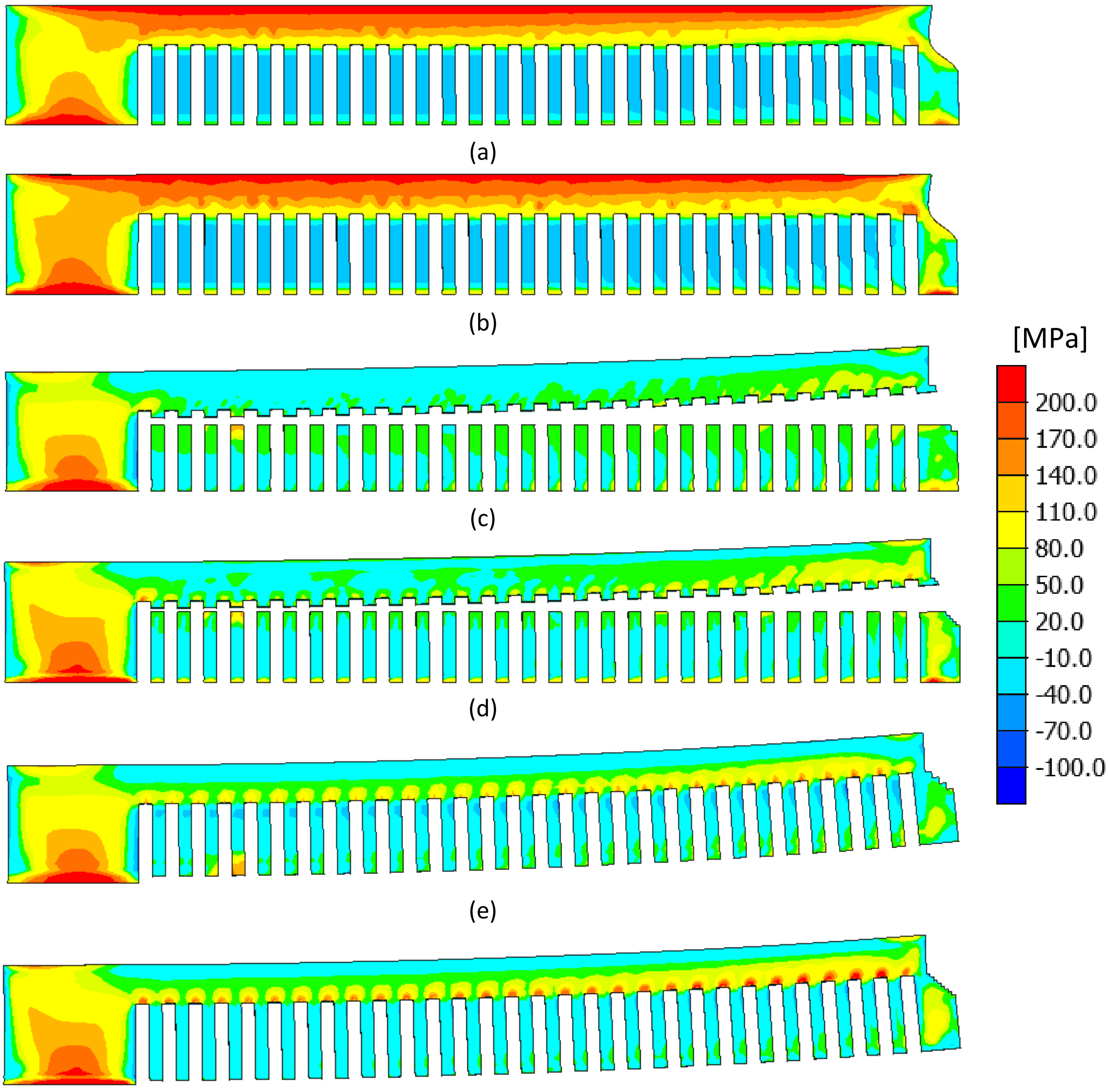

(a)

(b)

(c)

(d)

(e)

(f)

Figure 4.32. Predicted σ_{xx} stress component field in the cantilever: (a) before cutting stage using the coarse mesh; (b) before cutting stage using the fine mesh; (c) after upper cut using the coarse mesh; (d) after upper cut using the fine mesh; (e) after lower cut using the fine mesh

The impact of the mesh on the numerical solution for the residual stress field is small, as highlighted in Figure 4.32. Nevertheless, the computational cost increases from 8 minutes up to 110 minutes when the mesh is refined. Besides, effect of the cut plane location (upper or lower) is evaluated numerically. After the material deposition and before cutting stage, the solid region of the cantilever contains tensile residual stresses along the length direction. However, the stress field presents a gradient in the vertical direction, increasing from the bottom to the upper face, as shown in Figure 4.32. After partial cutting stage, occurs the residual stress relief, which is more significant when the cut plane is located at the upper face of the thin vertical supports since the presence of the vertical supports (ribs) induces a stress concentration.

The predicted vertical displacement field in the cantilever after cut is presented in Figure 4.33, comparing the situations upper and lower cut in the numerical simulation. The cantilever deflection is larger when the cut plane is located at the interface between the sample and the substrate, which is in agreement with the experimental measurements (see Figure 4.31). Figure 4.34 (a) shows the predicted cantilever profile after cutting operation, evaluated in the upper face of the cantilever, which is close to a parabola. The mesh refinement leads to a slight reduction of the deflection values.

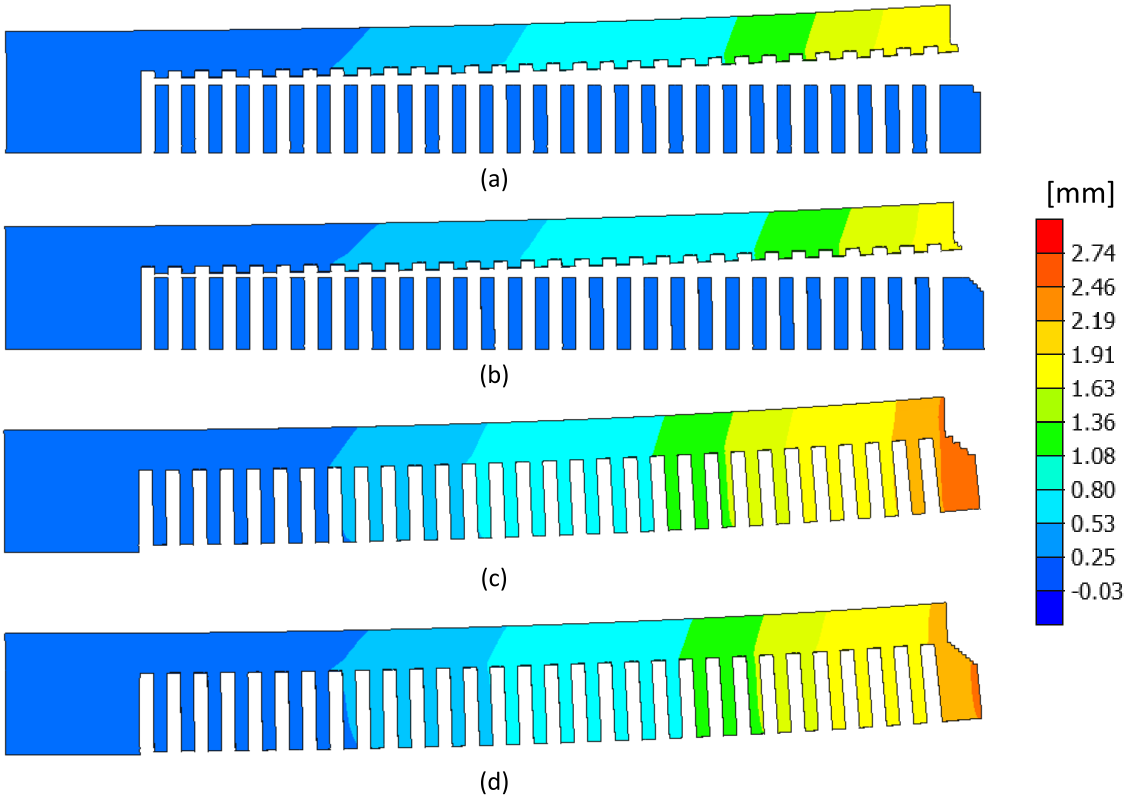

Figure 4.33. Predicted vertical displacement field in the cantilever after cutting stage: (a) upper cut using the coarse mesh; (b) upper cut using the fine mesh; (c) lower cut using the coarse mesh; (d) lower cut using the fine mesh.

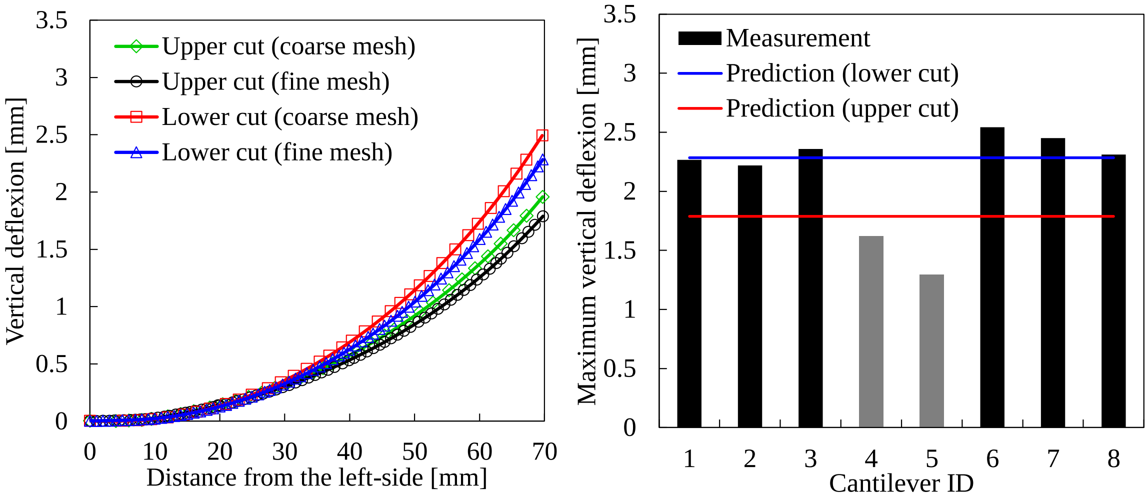

(a) (b)

Figure 4.34. Effect of the cutting position on the predicted cantilever distortion: (a) numerical prediction; (b) experimental measurements.

Figure 4.34 (b) presents the comparison between the experimental measurements of the maximum vertical deflection and the numerical predictions. Although the use of default values for the inherent strains (see Section 3.2.2), the numerical predictions are in good agreement with the experimental measurements. Indeed, considering the cut plane located at the lower face of the thin vertical supports, the difference between numerical and experimental values of maximum vertical deflection is lower than 10%. Nevertheless, this difference increases up to 40% when the cut plane is located at the upper face of the thin vertical supports.

Using the experimental measurements of the maximum vertical displacement in each cantilever (Figure 4.34 (b)), the isotropic calibration of the inherent strains was carried out in the Simufact Additive. This allows to obtain the inherent strains associated to each set of process parameters used in the experimental campaign (Table 2.2), which can be further used in the numerical analysis of more complex geometries. Table 4.1 presents the obtained values for each cantilever, i.e. for different combinations of process parameters, namely laser power, the scanning speed, the hatch distance, the layer thickness and the laser emission mode.

Table 4.1. Inherent strain values obtained with the isotropic calibration procedure (Simufact Additive) for cantilever built with AlSi10Mg powder.

Cantilever ID	Target vertical deflexion [mm]	Achieved vertical deflexion [mm]	Inherent strain ε_{xx}=ε_{yy}	Inherent strain ε_{zz}
1	2.21	2.23	-0.0034	-0.03
2	2.22	2.24	-0.0034	-0.03
3	2.37	2.37	-0.0037	-0.03
4	1.62	1.61	-0.0031	-0.03
5	1.29	1.29	-0.0024	-0.03
6	2.53	2.54	-0.0043	-0.03
7	2.46	2.46	-0.0040	-0.03
8	2.29	2.29	-0.0035	-0.03

4.4.2. Heat treatment

The lateral view of the cantilever subjected to heat treatment is presented in Figure 4.35, comparing the geometry before and after the cutting operation. Applying the heat treatment, the cantilever deflection after the cut is negligible when compared with the deflexion for the same process parameters and cut but without heat treatment (cantilever #7), which was presented in Figure 4.31 (c). Therefore, the heat treatment is effective in significantly reducing the deflexion of the components after cutting the support structures.

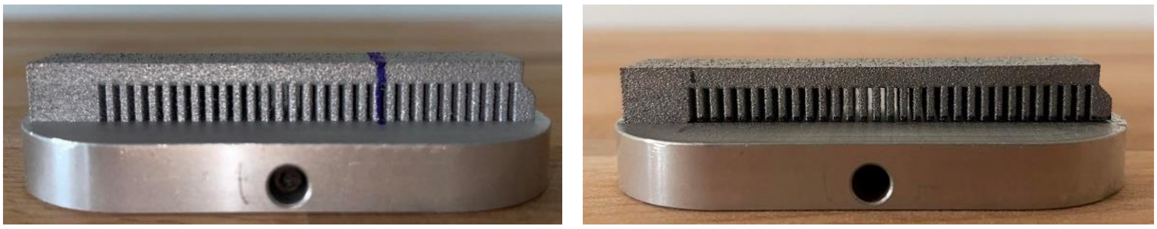
(a) (b)

Figure 4.35. Lateral view of the cantilever after the heat treatment: (a) before cut; (b) after cut.

The predicted σ_{xx} stress component field before the heat treatment (after build), after the heat treatment and after cutting is presented in Figure 4.36. The stress gradient in the vertical direction of the cantilever is strongly reduced applying the heat treatment. However, the global level of tensile residual stress increased, particularly in the region near the left-most bulky part of the cantilever. On the other hand, a significant residual stress relief occurs after the cutting stage, as shown in Figure 4.36 (e)-(f).

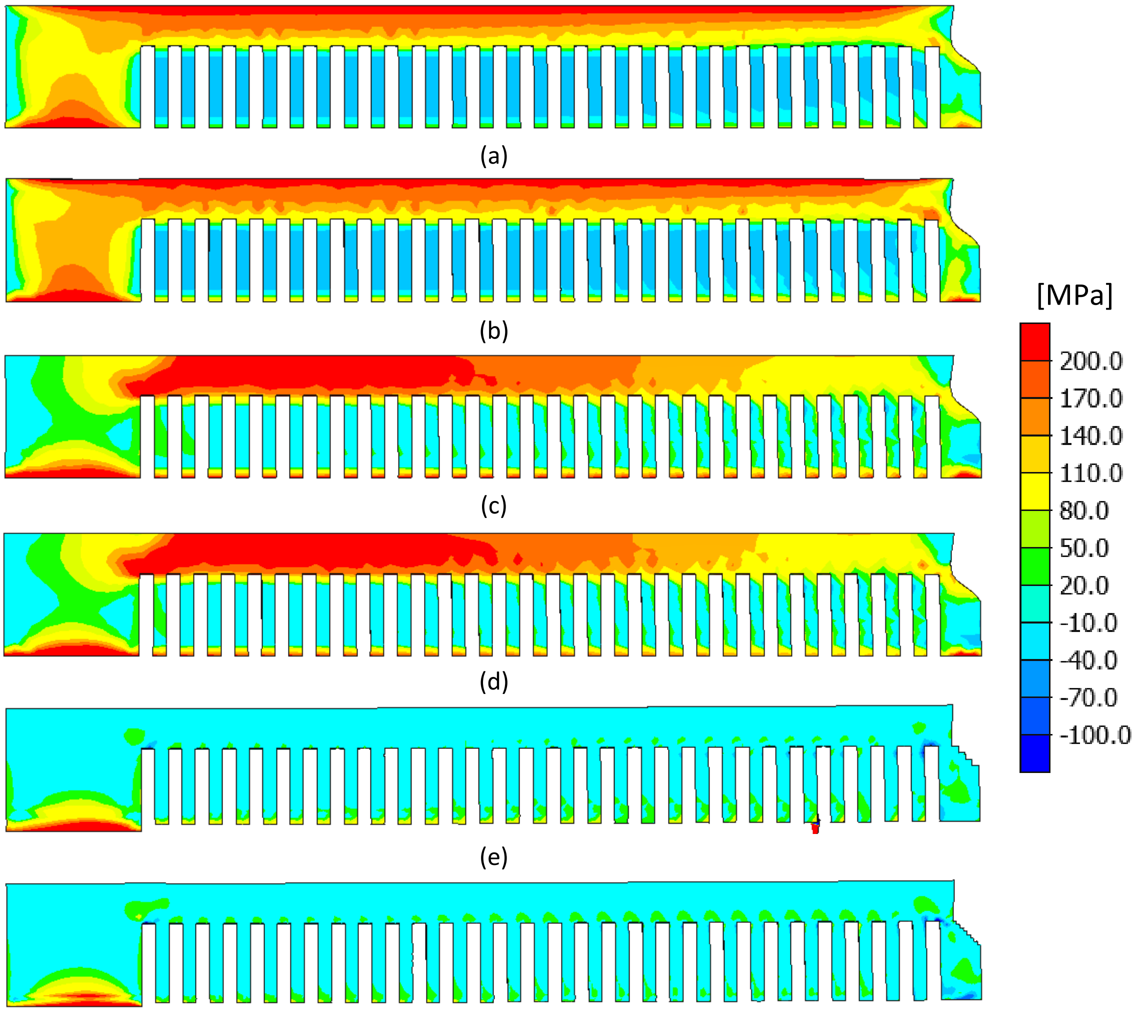

(a)

(b)

(c)

(d)

(e)

(f)

Figure 4.36. Predicted σ_{xx} stress component field in the cantilever: (a) before heat treatment using the coarse mesh; (b) before heat treatment using the fine mesh; (c) after heat treatment using the coarse mesh; (d) after heat treatment using the fine mesh; (e) after cut using the fine mesh; (f) after cut using the fine mesh

Figure 4.37 (a) presents the predicted cantilever profile after the cutting operation, comparing the samples with and without heat treatment. Indeed, the maximum vertical deflection is reduced from 2.3 mm without heat treatment down to 0.25 mm with the application of the heat treatment. After the heat treatment, the cantilever deflection resulting from the cutting operation is very small due to the nearly uniform residual stress distribution through the thickness (vertical direction of the cantilever). Figure 4.37 (b) presents the measured cantilever deflection profile before and after the cutting operation, considering the process parameters listed in Table 2.2 corresponding to the cantilever #7 and posterior heat treatment. The difference between the profile obtained before and after the cut is negligible. In fact, the cantilever after the heat treatment and before the cutting operation already shows a slight deflection. The numerical prediction is in agreement with the experimental observation of the cantilever deflection.

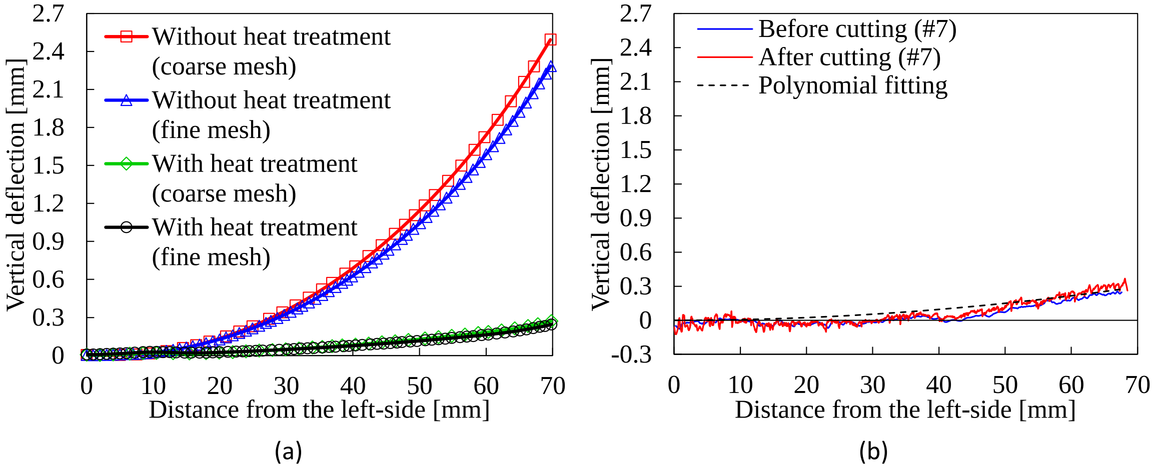

Figure 4.37. Effect of the heat treatment on the cantilever distortion after lower cut: (a) numerical prediction using two different meshes; (b) experimental measurements.

5. CONCLUSIONS

The metal powder-based additive manufacturing processes have attracted the attention of several industries by allowing to produce parts with complex geometry, avoiding the design constraints of traditional manufacturing processes Nevertheless, the complex heat transport and physical mechanisms occurring during the cyclic melting and solidification process leads to the occurrence of different manufacturing defects. Therefore, the main objective of the present study is the proper selection of the process parameters to be used in the Laser-Powder Bed Fusion (L-PBF) process. Two different powder materials (AlSi10Mg and Al-6.3Cu) were studied, using both numerical and experimental analysis. Hence, different combinations of process parameters were used to build three different geometries: (i) single track scanning; (ii) hollow thin-wall cube and (iii) cantilever. The finite element modelling of the L-PBF manufacturing process was carried at two different scales: (i) meso-scale analysis using the in-house finite element code DD3IMP and (ii) macro-scale analysis of the cantilevers using the Simufact Additive. The numerical predictions were compared with the experimental measurements.

Concerning the single tracks of AlSi10Mg and Al-6.3Cu built on the substrate, the track width increases by increasing the laser power and decreasing the scanning speed. Despite the variability in the experimental data, the numerical predictions of the melt pool size are in agreement with the experimental measurements performed in the cross-section of each scanned track. The measured melt pool height is significatively larger for AlSi10Mg in comparison with the one obtained for Al-6.3Cu powder mixture. On the other and, for large values of laser power the melt pool depth is significatively larger for Al-6.3Cu powder mixture in comparison with the one obtained for AlSi10Mg. The numerical model highlights that the interface between powder layer and substrate for AlSi10Mg using the modulated wave laser emission mode can be uniform, non-uniform or discontinuous depending on the adopted point distance (scanning speed).

The effect of the multi-layer deposition was evaluated using hollow thin-wall cubes. Using the same process parameters to build the hollow thin-wall cubes using AlSi10Mg, the obtained wall thickness is significatively larger than the melt pool width obtained in the single track. This is a consequence of the low thermal conductivity of the powder bed, i.e.

the heat generated by the laser beam is dissipated mainly through the walls, which present a small cross-section for the heat flux. The numerical results value highlighting the influence of the preceding wall thickness (0.2 mm or 0.4 mm). For 0.2 mm of initial wall thickness the predicted track width was 0.4 mm, while using 0.4 mm of initial wall thickness the predicted track width was 0.3 mm. This shows the importance of multi-layer deposition modelling for accurate prediction of the wall thickness.

The cantilevers were used evaluate the residual stresses generated both during the manufacturing process and after the heat treatment. The residual stresses were indirectly measured using the cantilever deflection after cut operation. Nevertheless, the results show that cantilever profile after cut is only slightly influenced by the process parameters studied (laser power, scanning speed, hatch distance, layer thickness and laser emission mode). Despite the use of default values for the inherent strains, the numerical predictions are in very good agreement with the experimental measurements, i.e. the difference between numerical and experimental values of maximum vertical deflection is lower than 10%. Applying the heat treatment to the cantilever geometry, the deflection resulting from the cutting operation is very small. Therefore, the adopted heat treatment (300ºC for 2 hours) is effective in significantly reducing the deflexion of the components after cutting the support structures.

5.1. Future work

Since the time to develop this study was very limited while the scientific research on AM processes is growing exponentially, some suggestions for future works are proposed:

- Produce hollow thin-wall cubes and cantilevers using the Al-6.3Cu powder mixture in order to assess the importance of the powder characteristics on the built quality. Use different portions of Cu in the Al-6.3Cu mixture since the thermo-physical properties of the Cu are significatively different from the ones of the Al.
- Study the thickness gradient along the hollow cube height for different combination of process parameters. Comparison between numerical and experimental data.
- Measure residual stresses in the cantilever by hole-drilling method and by x-ray diffraction method and compare both measurement techniques. Evaluate the impact of the different heat treatments (holding temperature and time) on the residual stresses.

REFERENCES

[1] I. Gibson, D. Rosen, B. Stucker, Additive manufacturing technologies: 3D printing, rapid prototyping, and direct digital manufacturing, second edition, 2015. https://doi.org/10.1007/978-1-4939-2113-3.

[2] Could 3D printing change the world? - Atlantic Council, (n.d.). https://www.atlanticcouncil.org/in-depth-research-reports/report/could-3d-printing-change-the-world/ (accessed July 5, 2022).

[3] W. Gao, Y. Zhang, D. Ramanujan, K. Ramani, Y. Chen, C.B. Williams, C.C.L. Wang, Y.C. Shin, S. Zhang, P.D. Zavattieri, The status, challenges, and future of additive manufacturing in engineering, Comput. Des. 69 (2015) 65–89. https://doi.org/10.1016/j.cad.2015.04.001.

[4] R. Liu, Z. Wang, T. Sparks, F. Liou, J. Newkirk, Aerospace applications of laser additive manufacturing, Laser Addit. Manuf. (2017) 351–371. https://doi.org/10.1016/B978-0-08-100433-3.00013-0.

[5] R. Leal, F.M. Barreiros, L. Alves, F. Romeiro, J.C. Vasco, M. Santos, C. Marto, Additive manufacturing tooling for the automotive industry, Int. J. Adv. Manuf. Technol. 92 (2017) 1671–1676. https://doi.org/10.1007/s00170-017-0239-8.

[6] M. Javaid, A. Haleem, Additive manufacturing applications in medical cases: A literature based review, Alexandria J. Med. 54 (2018) 411–422. https://doi.org/10.1016/j.ajme.2017.09.003.

[7] N. Guo, M.C. Leu, Additive manufacturing: technology, applications and research needs, Front. Mech. Eng. 8 (2013) 215–243. https://doi.org/10.1007/s11465-013-0248-8.

[8] J.C. Ruiz-Morales, A. Tarancón, J. Canales-Vázquez, J. Méndez-Ramos, L. Hernández-Afonso, P. Acosta-Mora, J.R. Marín Rueda, R. Fernández-González, J.A. Rogers, J.A. Lewis, D. Su, E.A. Stach, R.S. Ruoff, Three dimensional printing of components and functional devices for energy and environmental applications, Energy Environ. Sci. 10 (2017) 846–859. https://doi.org/10.1039/C6EE03526D.

[9] M.K. Thompson, G. Moroni, T. Vaneker, G. Fadel, R.I. Campbell, I. Gibson, A. Bernard, J. Schulz, P. Graf, B. Ahuja, F. Martina, Design for Additive Manufacturing:

Trends, opportunities, considerations, and constraints, CIRP Ann. - Manuf. Technol. 65 (2016) 737–760. https://doi.org/10.1016/j.cirp.2016.05.004.

[10] ASTM F2792-12a, Standard Terminology for Additive Manufacturing Technologies, (Withdrawn 2015), ASTM International, West Conshohocken, PA, 2012, n.d. https://www.astm.org/Standards/F2792.htm (accessed May 10, 2017).

[11] Covering additive and 3D printing technologies for the production of functional, end use parts | Additive Manufacturing, (n.d.). https://www.additivemanufacturing.media/ (accessed July 5, 2022).

[12] D. Herzog, V. Seyda, E. Wycisk, C. Emmelmann, Additive manufacturing of metals, Acta Mater. 117 (2016) 371–392. https://doi.org/10.1016/j.actamat.2016.07.019.

[13] T. DebRoy, H.L. Wei, J.S. Zuback, T. Mukherjee, J.W. Elmer, J.O. Milewski, A.M. Beese, A. Wilson-Heid, A. De, W. Zhang, Additive manufacturing of metallic components – Process, structure and properties, Prog. Mater. Sci. 92 (2018) 112–224. https://doi.org/10.1016/j.pmatsci.2017.10.001.

[14] M. Simonelli, Y.Y. Tse, C. Tuck, On the texture formation of selective laser melted Ti-6Al-4V, Metall. Mater. Trans. A Phys. Metall. Mater. Sci. 45 (2014) 2863–2872. https://doi.org/10.1007/s11661-014-2218-0.

[15] C. Tan, K. Zhou, W. Ma, B. Attard, P. Zhang, T. Kuang, Selective laser melting of high-performance pure tungsten: parameter design, densification behavior and mechanical properties, Sci. Technol. Adv. Mater. 19 (2018) 370–380. https://doi.org/10.1080/14686996.2018.1455154.

[16] R. Wojtuszewski, A. Banas, M. Oliwa, Additive manufacturing of titanium alloys, Annu. Forum Proc. - AHS Int. 2018-May (2018) 263–270. https://doi.org/10.1201/9781315119106-16/ADDITIVE-MANUFACTURING-TITANIUM-ALLOYS-DUTTA-FRANCIS-FROES.

[17] M. Abdelwahed, S. Bengsston, R. Casati, A. Larsson, M. Vedani, L-PBF Processing of Steel Powders Produced by Gas and Water Atomization, BHM Berg- Und Hüttenmännische Monatshefte 2020 1661. 166 (2021) 40–45. https://doi.org/10.1007/S00501-020-01071-1.

[18] H. Taheri, M. Shoaib, L. Koester, T. Bigelow, P. Collins, L. Bond, Powder-based additive manufacturing - a review of types of defects, generation mechanisms, detection, property evaluation and metrology, Int. J. Addit. Subtractive Mater. Manuf.

1 (2017) 172. https://doi.org/10.1504/IJASMM.2017.088204.

[19] C. Galy, E. Le Guen, E. Lacoste, C. Arvieu, Main defects observed in aluminum alloy parts produced by SLM: From causes to consequences, Addit. Manuf. 22 (2018) 165–175. https://doi.org/10.1016/J.ADDMA.2018.05.005.

[20] B. Zhang, L. Dembinski, C. Coddet, The study of the laser parameters and environment variables effect on mechanical properties of high compact parts elaborated by selective laser melting 316L powder, Mater. Sci. Eng. A. 584 (2013) 21–31. https://doi.org/10.1016/j.msea.2013.06.055.

[21] W.J. Sames, F.A. List, S. Pannala, R.R. Dehoff, S.S. Babu, The metallurgy and processing science of metal additive manufacturing, Int. Mater. Rev. 61 (2016) 315–360. https://doi.org/10.1080/09506608.2015.1116649.

[22] T. Mukherjee, W. Zhang, T. DebRoy, An improved prediction of residual stresses and distortion in additive manufacturing, Comput. Mater. Sci. 126 (2017) 360–372. https://doi.org/10.1016/J.COMMATSCI.2016.10.003.

[23] Z. Li, R. Xu, Z. Zhang, I. Kucukkoc, The influence of scan length on fabricating thin-walled components in selective laser melting, Int. J. Mach. Tools Manuf. 126 (2018) 1–12. https://doi.org/10.1016/j.ijmachtools.2017.11.012.

[24] S. Das, Physical Aspects of Process Control in Selective Laser Sintering of Metals, Adv. Eng. Mater. 5 (2003) 701–711. https://doi.org/10.1002/adem.200310099.

[25] H. Masuo, Y. Tanaka, S. Morokoshi, H. Yagura, T. Uchida, Y. Yamamoto, Y. Murakami, Influence of defects, surface roughness and HIP on the fatigue strength of Ti-6Al-4V manufactured by additive manufacturing, Int. J. Fatigue. 117 (2018) 163–179. https://doi.org/10.1016/j.ijfatigue.2018.07.020.

[26] Y. Kok, X.P. Tan, P. Wang, M.L.S. Nai, N.H. Loh, E. Liu, S.B. Tor, Anisotropy and heterogeneity of microstructure and mechanical properties in metal additive manufacturing: A critical review, Mater. Des. 139 (2018) 565–586. https://doi.org/10.1016/j.matdes.2017.11.021.

[27] E. Liverani, A.H.A. Lutey, A. Ascari, A. Fortunato, The effects of hot isostatic pressing (HIP) and solubilization heat treatment on the density, mechanical properties, and microstructure of austenitic stainless steel parts produced by selective laser melting (SLM), Int. J. Adv. Manuf. Technol. 107 (2020) 109–122. https://doi.org/10.1007/s00170-020-05072-9.

[28] D. Baere, V. Cauwenbergh, V. Hooreweder, H. Jesper, D. De Baere, P. Van Cauwenbergh, M. Bayat, S. Mohanty, Thermo-mechanical modelling of stress relief heat treatments after laser-based powder bed fusion Publication date : Publisher ' s PDF , also known as Version of record Thermo-mechanical modelling of stress relief heat treatments after laser-based powder bed fusion, Addit. Manuf. 38 (2021) 101818. https://doi.org/10.1016/j.addma.2020.101818.

[29] E. Liverani, S. Toschi, L. Ceschini, A. Fortunato, Effect of selective laser melting (SLM) process parameters on microstructure and mechanical properties of 316L austenitic stainless steel, J. Mater. Process. Technol. 249 (2017) 255–263. https://doi.org/10.1016/j.jmatprotec.2017.05.042.

[30] X. Zhou, N. Dai, M. Chu, L. Wang, D. Li, L. Zhou, X. Cheng, X-ray CT analysis of the influence of process on defect in Ti-6Al-4V parts produced with Selective Laser Melting technology, Int. J. Adv. Manuf. Technol. 106 (2020) 3–14. https://doi.org/10.1007/s00170-019-04347-0.

[31] R. Acevedo, P. Sedlak, R. Kolman, M. Fredel, Residual stress analysis of additive manufacturing of metallic parts using ultrasonic waves: State of the art review, J. Mater. Res. Technol. 9 (2020) 9457–9477. https://doi.org/10.1016/j.jmrt.2020.05.092.

[32] W. King, A.T. Anderson, R.M. Ferencz, N.E. Hodge, C. Kamath, S.A. Khairallah, Overview of modelling and simulation of metal powder bed fusion process at Lawrence Livermore National Laboratory, Mater. Sci. Technol. 31 (2015) 957–968. https://doi.org/10.1179/1743284714Y.0000000728.

[33] B. Schoinochoritis, D. Chantzis, K. Salonitis, Simulation of metallic powder bed additive manufacturing processes with the finite element method: A critical review, Proc. Inst. Mech. Eng. Part B J. Eng. Manuf. 231 (2017) 96–117. https://doi.org/10.1177/0954405414567522.

[34] W.E. King, A.T. Anderson, R.M. Ferencz, N.E. Hodge, C. Kamath, S.A. Khairallah, A.M. Rubenchik, Laser powder bed fusion additive manufacturing of metals; physics, computational, and materials challenges, Appl. Phys. Rev. 2 (2015) 041304. https://doi.org/10.1063/1.4937809.

[35] M. Markl, C. Körner, Multiscale Modeling of Powder Bed–Based Additive Manufacturing, Annu. Rev. Mater. Res. 46 (2016) 93–123.

https://doi.org/10.1146/annurev-matsci-070115-032158.

[36] Y. Zhang, G. Guillemot, M. Bernacki, M. Bellet, Macroscopic thermal finite element modeling of additive metal manufacturing by selective laser melting process, Comput. Methods Appl. Mech. Eng. 331 (2018) 514–535. https://doi.org/10.1016/J.CMA.2017.12.003.

[37] A. Bandyopadhyay, K.D. Traxel, Invited review article: Metal-additive manufacturing—Modeling strategies for application-optimized designs, Addit. Manuf. 22 (2018) 758–774. https://doi.org/10.1016/j.addma.2018.06.024.

[38] M.M. Francois, A. Sun, W.E. King, N.J. Henson, D. Tourret, C.A. Bronkhorst, N.N. Carlson, C.K. Newman, T. Haut, J. Bakosi, J.W. Gibbs, V. Livescu, S.A. Vander Wiel, A.J. Clarke, M.W. Schraad, T. Blacker, H. Lim, T. Rodgers, S. Owen, F. Abdeljawad, J. Madison, A.T. Anderson, J.-L. Fattebert, R.M. Ferencz, N.E. Hodge, S.A. Khairallah, O. Walton, Modeling of additive manufacturing processes for metals: Challenges and opportunities, Curr. Opin. Solid State Mater. Sci. (2017). https://doi.org/10.1016/j.cossms.2016.12.001.

[39] D. Riedlbauer, P. Steinmann, J. Mergheim, Thermomechanical finite element simulations of selective electron beam melting processes: performance considerations, Comput. Mech. 54 (2014) 109–122. https://doi.org/10.1007/s00466-014-1026-0.

[40] I. Gibson, D.W. Rosen, B. Stucker, Additive Manufacturing Technologies, Springer US, Boston, MA, 2010. https://doi.org/10.1007/978-1-4419-1120-9.

[41] B. Cheng, S. Shrestha, K. Chou, Stress and deformation evaluations of scanning strategy effect in selective laser melting, Addit. Manuf. 12 (2016) 240–251. https://doi.org/10.1016/j.addma.2016.05.007.

[42] F. Dugast, P. Apostolou, A. Fernandez, W. Dong, Q. Chen, S. Strayer, R. Wicker, A.C. To, Part-scale thermal process modeling for laser powder bed fusion with matrix-free method and GPU computing, Addit. Manuf. 37 (2021) 101732. https://doi.org/10.1016/j.addma.2020.101732.

[43] C. Li, C.H. Fu, Y.B. Guo, F.Z. Fang, A multiscale modeling approach for fast prediction of part distortion in selective laser melting, J. Mater. Process. Technol. 229 (2016) 703–712. https://doi.org/10.1016/J.JMATPROTEC.2015.10.022.

[44] J. Smith, W. Xiong, W. Yan, S. Lin, P. Cheng, O.L. Kafka, G.J. Wagner, J. Cao, W.K.

Liu, Linking process, structure, property, and performance for metal-based additive manufacturing: computational approaches with experimental support, Comput. Mech. 57 (2016) 583–610. https://doi.org/10.1007/s00466-015-1240-4.

[45] S.M. Hashemi, S. Parvizi, H. Baghbanijavid, A.T.L. Tan, M. Nematollahi, A. Ramazani, N.X. Fang, M. Elahinia, Computational modelling of process–structure–property–performance relationships in metal additive manufacturing: a review, Int. Mater. Rev. 67 (2022) 1–46. https://doi.org/10.1080/09506608.2020.1868889.

[46] T. Mukherjee, T. Debroy, A digital twin for rapid qualification of 3D printed metallic components, Appl. Mater. Today. 14 (2019) 59–65. https://doi.org/10.1016/j.apmt.2018.11.003.

[47] P. Foteinopoulos, A. Papacharalampopoulos, K. Angelopoulos, P. Stavropoulos, Development of a simulation approach for laser powder bed fusion based on scanning strategy selection, (2020) 3085–3100.

[48] D.R. Gunasegaram, A.B. Murphy, M.J. Matthews, T. DebRoy, The case for digital twins in metal additive manufacturing, J. Phys. Mater. 4 (2021) 040401. https://doi.org/10.1088/2515-7639/AC09FB.

[49] R.S. Mishra, S. Thapliyal, Design approaches for printability-performance synergy in Al alloys for laser-powder bed additive manufacturing, Mater. Des. 204 (2021) 109640. https://doi.org/10.1016/j.matdes.2021.109640.

[50] K. Riener, S. Oswald, M. Winkler, G.J. Leichtfried, Influence of storage conditions and reconditioning of AlSi10Mg powder on the quality of parts produced by laser powder bed fusion (LPBF), Addit. Manuf. 39 (2021) 101896. https://doi.org/10.1016/J.ADDMA.2021.101896.

[51] K. Riener, N. Albrecht, S. Ziegelmeier, R. Ramakrishnan, L. Haferkamp, A.B. Spierings, G.J. Leichtfried, Influence of particle size distribution and morphology on the properties of the powder feedstock as well as of AlSi10Mg parts produced by laser powder bed fusion (LPBF), Addit. Manuf. 34 (2020) 101286. https://doi.org/10.1016/J.ADDMA.2020.101286.

[52] S. Rao, R. Cunningham, T. Ozturk, A.D. Rollett, Measurement and Analysis of Porosity in Al-10Si-1Mg Components Additively Manufactured by Selective Laser Melting, Mater. Perform. Charact. 5 (2016) 701–716. https://doi.org/10.1520/MPC20160037.

[53] B. Ahuja, M. Karg, K. Yu, M. Schmidt, Fabrication and Characterization of High Strength Al-Cu alloys Processed Using Laser Beam Melting in Metal Powder Bed, Phys. Procedia. 56 (2014) 135–146. https://doi.org/10.1016/j.phpro.2014.08.156.

[54] A. Kreitcberg, V. Brailovski, S. Turenne, Effect of heat treatment and hot isostatic pressing on the microstructure and mechanical properties of Inconel 625 alloy processed by laser powder bed fusion, Mater. Sci. Eng. A. 689 (2017) 1–10. https://doi.org/10.1016/J.MSEA.2017.02.038.

[55] S. Nikam, H. Wu, R. Harkin, J. Quinn, R. Lupoi, S. Yin, S. McFadden, On the application of the anisotropic enhanced thermal conductivity approach to thermal modelling of laser-based powder bed fusion processes, Addit. Manuf. 55 (2022) 102870. https://doi.org/10.1016/J.ADDMA.2022.102870.

[56] J. Goldak, A. Chakravarti, M. Bibby, A new finite element model for welding heat sources, Metall. Trans. B. 15 (1984) 299–305. https://doi.org/10.1007/BF02667333.

[57] B. Liu, B.Q. Li, Z. Li, P. Bai, Y. Wang, Z. Kuai, Numerical investigation on heat transfer of multi-laser processing during selective laser melting of AlSi10Mg, Results Phys. 12 (2019) 454–459. https://doi.org/10.1016/J.RINP.2018.11.075.

[58] H.C. Tran, Y.L. Lo, Heat transfer simulations of selective laser melting process based on volumetric heat source with powder size consideration, J. Mater. Process. Technol. 255 (2018) 411–425. https://doi.org/10.1016/J.JMATPROTEC.2017.12.024.

[59] B.M. Marques, C.M. Andrade, D.M. Neto, M.C. Oliveira, J.L. Alves, L.F. Menezes, Numerical Analysis of Residual Stresses in Parts Produced by Selective Laser Melting Process, Procedia Manuf. 47 (2020) 1170–1177. https://doi.org/10.1016/J.PROMFG.2020.04.167.

[60] M. Bugatti, Q. Semeraro, Limitations of the inherent strain method in simulating powder bed fusion processes, Addit. Manuf. 23 (2018) 329–346. https://doi.org/10.1016/j.addma.2018.05.041.

[61] N. Peter, Z. Pitts, S. Thompson, A. Saharan, Benchmarking build simulation software for laser powder bed fusion of metals, Addit. Manuf. 36 (2020) 101531. https://doi.org/10.1016/j.addma.2020.101531.

[62] Y. Du, X. You, F. Qiao, L. Guo, Z. Liu, Results in Physics A model for predicting the temperature field during selective laser melting, Results Phys. 12 (2019) 52–60. https://doi.org/10.1016/j.rinp.2018.11.031.

ANNEX A

Step Method for Soft Aluminium Alloys

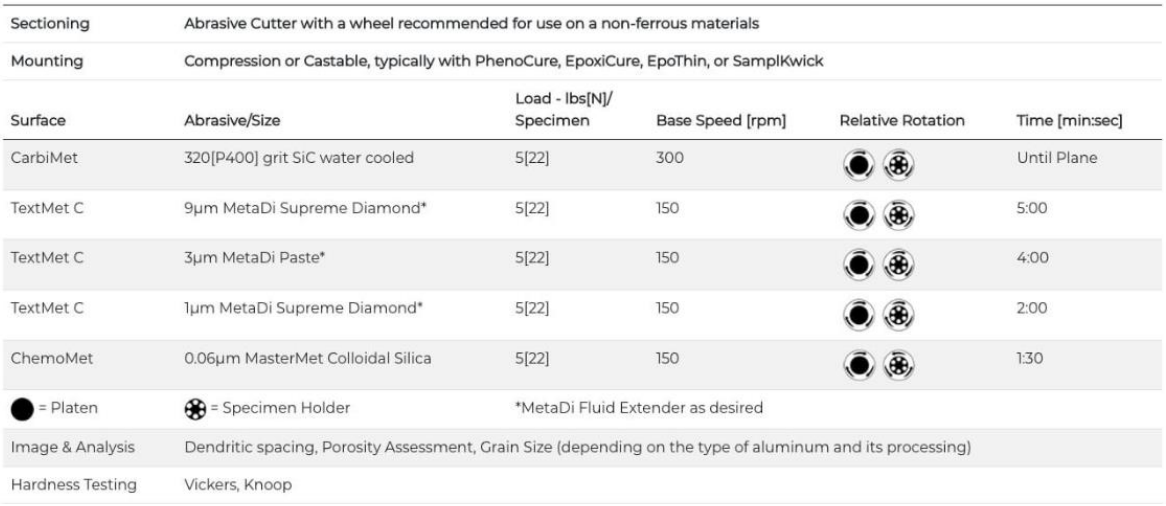

Sectioning	**Abrasive Cutter with a wheel recommended for use on a non-ferrous materials**				
Mounting	**Compression or Castable, typically with PhenoCure, EpoxiCure, EpoThin, or SamplKwick**				
Surface	**Abrasive/Size**	**Load - lbs[N]/ Specimen**	**Base Speed [rpm]**	**Relative Rotation**	**Time [min:sec]**
CarbiMet	320[P400] grit SiC water cooled	5[22]	300	● ⊛	Until Plane
TextMet C	9µm MetaDi Supreme Diamond*	5[22]	150	● ⊛	5:00
TextMet C	3µm MetaDi Paste*	5[22]	150	● ⊛	4:00
TextMet C	1µm MetaDi Supreme Diamond*	5[22]	150	● ⊛	2:00
ChemoMet	0.06µm MasterMet Colloidal Silica	5[22]	150	● ⊛	1:30
● = Platen	⊛ = Specimen Holder	*MetaDi Fluid Extender as desired			
Image & Analysis	Dendritic spacing, Porosity Assessment, Grain Size (depending on the type of aluminum and its processing)				
Hardness Testing	Vickers, Knoop				